NMR AND TRANSPORT STUDIES ON GROUP IV CLATHRATES AND RELATED INTERMETALLIC MATERIALS

A Dissertation

by

XIANG ZHENG

Submitted to the Office of Graduate Studies of
Texas A&M University
in partial fulfillment of the requirements for the degree of

DOCTOR OF PHILOSOPHY

August 2012

Major Subject: Materials Science and Engineering

NMR AND TRANSPORT STUDIES ON GROUP IV CLATHRATES AND RELATED INTERMETALLIC MATERIALS

A Dissertation

by

XIANG ZHENG

Submitted to the Office of Graduate Studies of
Texas A&M University
in partial fulfillment of the requirements for the degree of

DOCTOR OF PHILOSOPHY

Approved by:

Chair of Committee,	Joseph H. Ross, Jr.
Committee Members,	Donald G. Naugle
	Steven M. Wright
	Glenn Agnolet
Chair of Intercollegiate Faculty,	Ibrahim Karaman

August 2012

Major Subject: Materials Science and Engineering

ABSTRACT

NMR and Transport Studies on Group IV Clathrates and
Related Intermetallic Materials. (August 2012)
Xiang Zheng, B.S., University of Science and Technology of China;
M.S., Texas A&M University
Chair of Advisory Committee: Dr. Joseph H. Ross, Jr.

Increasing efforts have been put into research about thermoelectric materials for the last few decades, especially recently, faced with the crucial demand for new energy and energy savings. Among the potential candidates for new generation thermoelectric materials are the intermetallic clathrates. Clathrates are cage-structured materials with guest atoms enclosed. Previous studies have shown lower thermal conductivities compared with many other bulk compounds, and it is believed that guest atom vibration modes are the reason for such thermal behaviors. Several models, including the Einstein oscillator and soft potential models, have been used to explain the guest motion. However the characterization of the anharmonic oscillating motion can be a challenge.

In this work, Nuclear Magnetic Resonance (NMR), heat capacity and transport measurements have been used to study several clathrate systems, especially the well-known type-I $Ba_8Ga_{16}Sn_{30}$, which has been reported to have one of the lowest thermal conductivities for bulk compounds. In this material the strong anharmonic rattling behavior was investigated and analyzed according to a double well potential model, yielding good agreement with the experimental results. Furthermore, the resistivity and heat capacity results were studied and analyzed according to the influence of the anharmonic contribution. This offered a way to connect the NMR, transport and heat capacity properties, providing an advantageous way to study strongly anharmonic

systems.

In further work, several related intermetallic materials were examined for their structure, motion and NMR properties. Dynamical and electrical behaviors were investigated by studying the magnetic and quadrupole NMR spin-lattice relaxation. Type-VIII $Ba_8Ga_{16}Sn_{30}$ exhibits an enhanced dynamics-related term at low temperature, but no rattling response as observed for the type-I structure. Type-I $Ba_8In_{16}Ge_{30}$ was compared with the type-I $Ba_8Ga_{16}Sn_{30}$ because their cage structures are similar. No strong anharmonic contribution was found in the NMR T_1 behavior of $Ba_8In_{16}Ge_{30}$, however the T_2 showed behavior characteristic of atomic motion. In all cases, the magnetic relaxation was used to characterize the electron structures, and n-type $Ba_8Ga_{16}Ge_{30}$ exhibited a spin-lattice relaxation behavior which is characteristic of impurity band structures near the Fermi surface. Also, a series of $Ba_8Cu_xGe_{46-x}$ clathrates were investigated and showed much more insulating like behavior. In related work, the layered $BaGa_4$ and $BaGa_3Sn$ have shown interesting NMR spin-spin relaxation behavior that indicates atomic fluctuations. This is similar to the situation found in type-I $Ba_8In_{16}Ge_{30}$. The influence of atomic motion on the NMR and also the atomic structures of these alloys is further discussed in this work.

ACKNOWLEDGMENTS

First, I would like to express my sincere gratitude to my advisor Dr. Joseph H. Ross, Jr., for all his support, encouragement and patience during these years. I enjoyed all the work and discussions we had during my graduate study. I'd like to thank many people I have worked with in Dr. Ross's group: Dr. Sergio Rodriguez, Laziz Saribaev, Jing-Han Chen, Dr. Venkat Goruganti, Dr. Weiping Gou and Haoyu Qian. It was a great pleasure to work with them and I really appreciate all their help and suggestions.

Many thanks to the members of my committee Dr. Donald G. Naugle, Dr. Glenn Agnolet, and Dr. Steven M. Wright for their time and suggestions. I'd like to thank the Chemistry Department for the use of XRD and MAS devices. Many thanks go to Dr. Naugle's lab for the help on Arc melting and PPMS.

Very special recognition to all my family and friends for all the encouragement and support through all these years. Also, I owe special gratitude to my girl friend, Chun Wu, for her understanding, inspiration, and all that she has done for me over these years.

Last but not least I would like to acknowledge the Robert A. Welch foundation and the Physics Department for financial support during my Ph.D. studies.

TABLE OF CONTENTS

CHAPTER Page

LIST OF TABLES

LIST OF FIGURES

FIGURE Page

FIGURE Page

FIGURE Page

FIGURE Page

FIGURE Page

FIGURE Page

CHAPTER I

INTRODUCTION

Currently, the demand for energy is becoming larger and larger. The environment and global climate have been impacted by the widespread use of petroleum and coal, and the existing stores of these energy sources is becoming highly limited. It is very important to find alternative clean energy and better ways to save energy.

For alternative energies, nuclear energy, bio-energy, solar-energy, natural gas, hydrogen, wind and water have already been used widely. For energy saving, one way of doing that is through the recycling of waste heat with thermoelectric generators. Solid state cooling and power generation based on thermoelectric effects have been known since the Seebeck effect and the Peltier effect were discovered in the 1800s [1]. As thermoelectric generators are solid-state devices, they are silent, reliable and scalable, making them ideal for small, distributed power generation [2].

In order to make this happen with lower cost, materials with high thermal efficiency will be needed. Most of the traditional materials have poor thermoelectric properties or are too expensive to use. Therefore people started to search for new generations of thermoelectric materials decades ago and many potential candidates have been reported [3, 4, 5, 6, 7, 8, 9]. Certain complex intermetallic materials and the group IV clathrates are important examples [10, 11]. Before putting them into practical use, a better understanding of their properties, such as lattice structure, electronic structure, transport properties, and magnetic properties, will be necessary.

In this work, we will focus on intermetallic clathrates and some related materials with interesting vibrational properties, trying to understand their basic properties.

The journal model is *IEEE Transactions on Applied Superconductivity.*

CHAPTER II

BACKGROUND AND REVIEW OF RECENT WORK

A. Thermoelectric materials

In 1807, Joseph Fourier made a major step by introducing the parameter κ, which is called the thermal conductivity, to describe heat transfer [12]. It is defined with respect to the steady-state flow of heat down a long rod with a temperature gradient, $J_u = -\kappa dT/dx$, where J_u is the flux of thermal energy [13]. κ usually comes from two sources: electrons and holes transporting heat (κ_e) and phonons travelling through the lattice (κ_l).

In 1821, Seebeck found that a voltage potential is created by the temperature difference between the hot and cold ends of the thermoelectric elements. The Seebeck coefficient is defined as $\alpha = \Delta V/\Delta T$. In a specific simple band case, it can be expressed by

$$\alpha = \left(\frac{8\pi^2\kappa_B^2}{3eh^2}\right) m^* T \left(\frac{\pi}{3n}\right)^2, \tag{2.1}$$

where n is the carrier concentration and m^* is the effective mass of the carrier. The maximum efficiency of a thermoelectric material for both power generation and cooling is determined by its figure of merit (zT),

$$zT = \left(\frac{\alpha^2 T}{\rho\kappa}\right) \tag{2.2}$$

where zT depends on Seebeck coefficient (α), absolute temperature (T), electrical resistivity (ρ), and thermal conductivity (κ). To maximize power generation efficiency, zT should be as high as possible. One way of doing that is to decrease κ.

For most materials, the longitudinal acoustic phonons are the most significant

feature determining κ. Since longitudinal waves have a greater group velocity than that of transverse waves, the relaxation length of longitudinal phonons will be greater. Thus, κ may be determined by the longitudinal phonons, especially low-frequency phonons with long wavelength, which will be limited in relaxation length by scattering. In principle, the thermal conductivity and electrical conductivity may be independently optimized because different length scales are associated with phonons and electric charge carriers. So it may be possible to minimize κ without making much change in the electric properties.

One popular way to find or produce low κ materials is to enhance the phonon scattering. Also note that a large and complex unit cell will minimize the number of accoustic phonons. Clathrates, layered materials and other nano scale materials are very good examples. The loosely bound guest atoms in clathrates and the large number of layer boundaries in layered materials will all increase the phonon scattering and reduce the thermal conductivities to some extent.

B. Review of recent clathrate studies related to this work

Investigations on clathrates have been going on for almost 200 years starting from the hydrate clathrates. In the early 1960s, researchers had already started to pay some attention to the thermoelectric properties of Si and Ge based clathrates [14, 15, 16]. Then in the 1990s, the concept of phonon glass electron crystal (PGEC) was proposed and applied to clathrates [2, 11]. Under this theory, PGEC materials would have electronic properties normally associated with good semiconductor crystals but a thermal conductivity normally associated with amorphous materials, which includes a lower thermal conductivity. G. S. Nolas *et al.* reported their results on the semiconducting Ge clathrate $Sr_8Ga_{16}Ge_{30}$ in 1998 [11], which demonstrated an

excellent example of PGEC behavior and brought much more attention to clathrates and their thermoelectric properties.

1. Crystal Structures

There are many different structure types for clathrates. Two of the most common structures are type I and VIII. As shown in Fig. 1, type-I clathrate contains two dodecahedral cages and six tetrakaidecahedral cages, while type-VIII is built up by dodecahedral cages, formed by three five-rings, three six-rings and three seven-rings per cage [17]. In this work, we are going to focus on these two structures among clathrate materials.

2. Thermoelectric properties

As mentioned above, the lattice thermal conductivity, κ_L , of $Sr_8Ga_{16}Ge_{30}$ was reported to be glass-like with a T^2 dependence at low temperatures and to be more than an order of magnitude smaller than that of crystalline germanium [11]. Later the same behavior was found in $Eu_8Ga_{16}Ge_{30}$ [18, 19]. From the neutron diffraction data reported by Sales [20], which showed large guest atom off-center displacements, guest atom resonant phonon scattering and scattering on tunneling states were believed to be responsible for the glass-like κ_L . But for clathrates with much less guest atom off-center displacement, glass-like behavior can still be observed in some cases, such as $Ba_8Ga_{16}Ge_{30}$ [21]. So it was suggested [21] that charge carrier scattering could also lead to a T^2 behavior of κ_L .

Later, type-I $Ba_8Ga_{16}Sn_{30}$ was reported to have one of the lowest thermal conductivities for a bulk compound, as shown in Fig. 2, while still behaving electronically as a heavy doped semiconductor [22, 23]. Its relatively large guest atom off-center displacement agreed with previous predictions and tends to point to the rattling

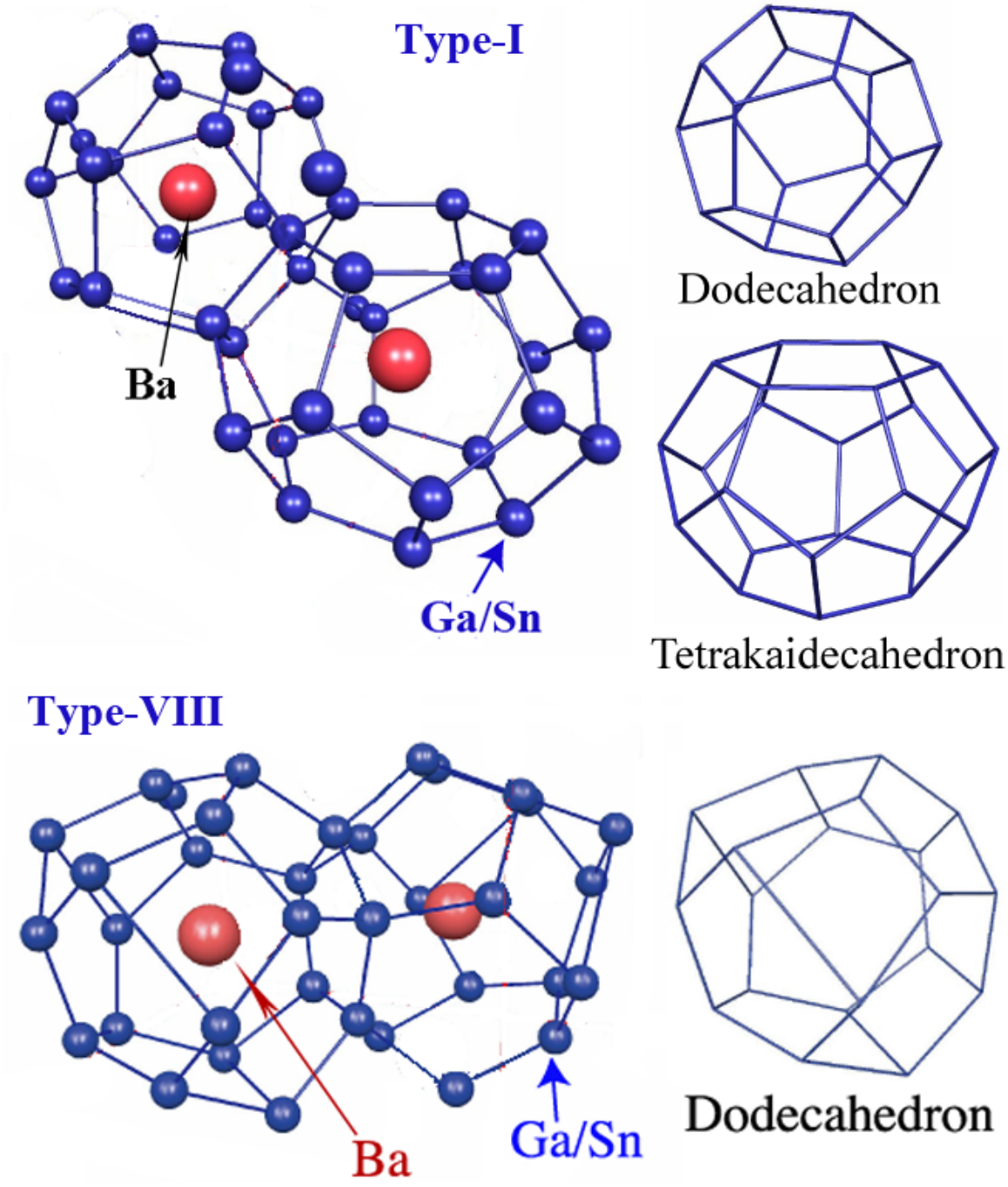

Fig. 1. Structures for type-I (upper) and type-VIII (lower) clathrates.

mechanism for reduction in κ_L.

There are many additional studies focused on optimizing thermal properties by different methods. For example, $Sr_8Ga_xGe_{46-x}$ was reported to have decreasing absolute value of Seebeck coefficient with increasing carrier concentration [24]. Okamoto *et al.* reported that lower thermal conductivity and higher zT in $Ba_8Ga_{16-x}In_xGe_{30}$ could be reached by increasing the lattice parameter and cage size slightly, which was dominated by the value of x [25]. Many similar examples can be found in other materials, including $Ba_8In_{16}Ge_{30-x}M_x$ (M=Si, Sn) [26], $Ba_8Cu_{6-x}Ge_{40+x}$ [27], and $Ba_8Ga_{16-x}Al_xSn_{30}$ [28].

Fig. 3, a reprint from ref. [26], shows a collection of data comparing clathrates lattice thermal conductivities and their corresponding cage sizes and guest atom free spaces, which is defined as the difference of the size between the cage and the guest atom [26]. These data indicate lower lattice thermal conductivities in clathrates is correlated with bigger guest free spaces, whereas the cage radius does not show much effect alone. This might be a good guide for the search for better thermoelectric clathrate materials. Also, this can lead to a discussion about the possible influence of guest atom motion to the thermal properties.

3. Guest atomic motions, models and discussions

As described above, the thermoelectric figure of merit in clathrate materials is believed to have close connection with its guest atom, and it is commonly believed that the phonon scattering caused by these guest atoms may be one of the major reasons for such low lattice thermal conductivities.

Shortly after the glass-like thermal behavior of $Sr_8Ga_{16}Ge_{30}$ was reported, several structural studies about related clathrates were published. X-ray and neutron diffraction measurements on $Sr_8Ga_{16}Ge_{30}$ and $Eu_8Ga_{16}Ge_{30}$ showed a clear off-center

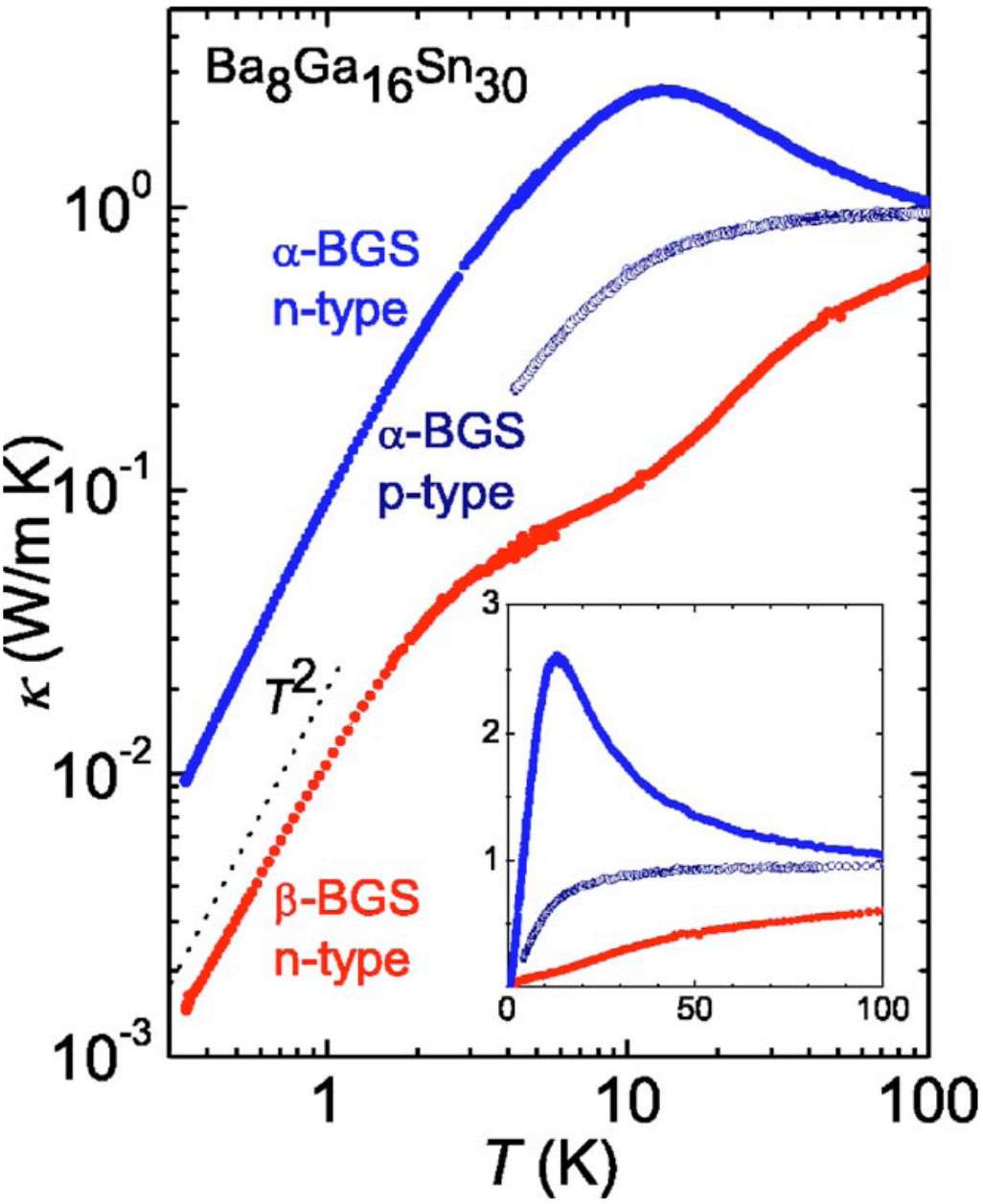

Fig. 2. Thermal conductivity of $\alpha-$ (type-VIII) and $\beta-$ (type-I) $Ba_8Ga_{16}Sn_{30}$. The inset shows the same data in a linear scale. Reprinted figure with permission from [23] ©(2008) by American Institute of Physics.

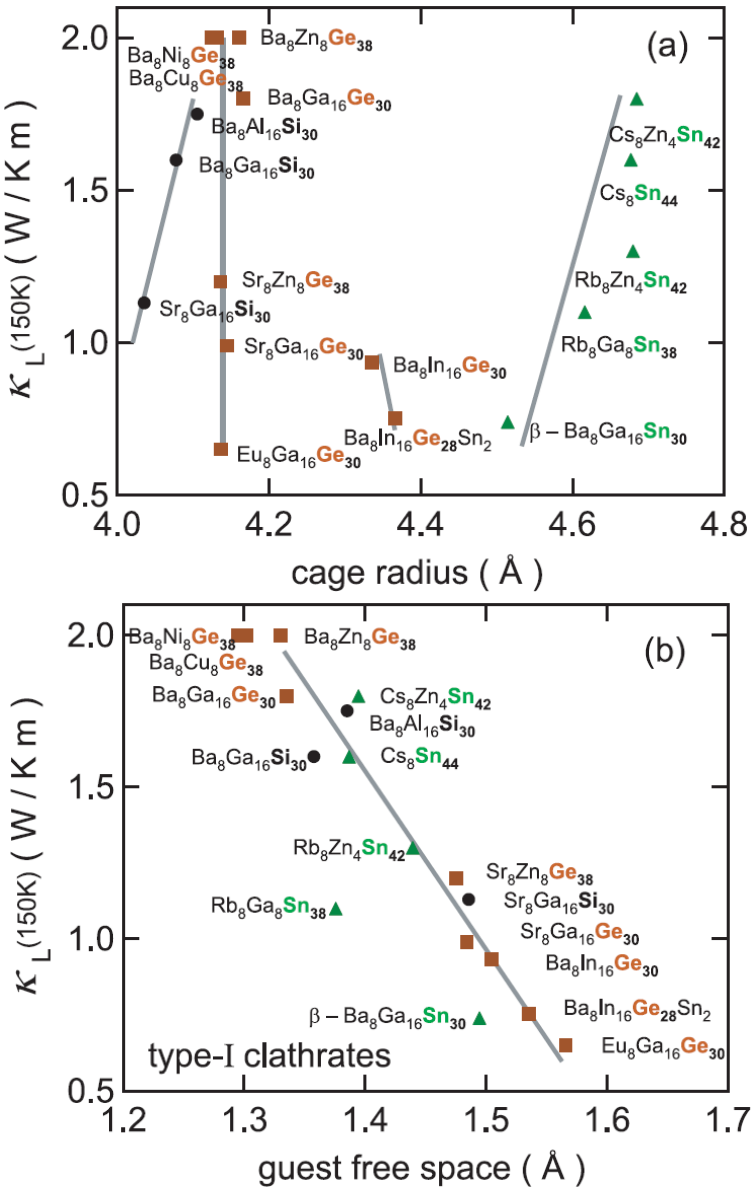

Fig. 3. Lattice thermal conductivities of clathrate materials with different cage radii (a) and guest free space (b). Reprinted figure with permission from [26] ©(2008) by the Physical Society of Japan.

displacement of the guest atom in the larger cage, by about 0.3-0.4 Å [19, 20, 29]. It was suggested that for these materials both rattling and tunneling states are important for the forming of their glass-like thermal conductivity. Also the existence of tunneling states was confirmed by Mössbauer spectroscopy for the case of $Eu_8Ga_{16}Ge_{30}$ [30].

In $Ba_8Ga_{16}Ge_{30}$, both x-ray and neutron diffraction showed very small off-center displacement for its guest atom Ba, which suggests a smaller contribution of tunneling states to its thermal properties. Raman scattering was later used to study the guest atom in $Ba_8Ga_{16}Ge_{30}$, with the result that p-type samples have much larger movable space for guest atoms than n-type. This explained why glass-like thermal behavior can be observed in p-type but not in n-type $Ba_8Ga_{16}Ge_{30}$ [22, 31], but it is still not clear what electronic feature causes this difference. The temperature dependence of the Raman spectra also showed that thermal rattling, not tunneling, is the major guest motion [31].

Similar studies were later carried out on type-I $Ba_8Ga_{16}Sn_{30}$ after it had been reported to have a particularly low thermal conductivity. A similar Ba(2) off-center displacement was reported, measuring around 0.4 Å from x-ray refinement, and a fourfold split off-center minimum was found for the guest position, which suggested a four-well potential model for the rattling Ba(2) [18, 23].

In order to get quantitative information about the connection between guest motion and thermal and electrical properties, different models have been established for different situations. For rattlers with harmonic motion or tiny off-center guest displacements, an Einstein oscillator model has been found to be successful to describe the motion, for example in $Ba_8Ga_{16}Ge_{30}$ and $Sr_8Ga_{16}Si_{30}$ [22, 32]. However for many clathrates with relatively large guest off-center displacement, the motion is better described as anharmonic. A simple approximation is to assume that the

potential is one-dimensional, which is a starting assumption for many studies [33]. A soft-potential model is one example for which one can numerically calculate κ_L and transport properties through its soft vibrational density of states and the tunneling of two level systems [34, 35]. A significant contribution from two level tunneling systems and a very broad distribution of oscillation frequencies are considered in this model, which can be used for both anharmonic and harmonic systems.

A 1-D double well potential has been successfully used for investigations of anharmonic behaviors in many cases [33, 36, 37, 38]. Here we used NMR techniques to measure the spin-lattice relaxation as one of our main analysis tools. A 1-D double well potential and a simplified 2D potential together with a two phonon Raman process have been used to fit the quadrupolar relaxation behavior. Furthermore, the fitted results can be used to analyze the corresponding anharmonic contribution to the transport and heat capacity properties [33, 39, 40]. Such studies are major parts of this work, and the details will be described in the following chapters. Such a 1-D approximation has also been used to analyze optical measurements [38], which has yielded results comparable to those from our NMR analysis, indicating a consistency of this method. However, a 2-D multi-well potential, suggested from the XRD and neutron scattering results, is also important and may lead to a better understanding of the anharmonic peoperties. Four-well 2-D potentials with tunneling states have been used for some computational work and shown good agreement with experimental results [41].

There are still conflicting opinions about the influence of the guest atom in reducing the thermal conductivity. For example, M. Christensen *et al.* reported phonon dispersion studies on $Ba_8Ga_{16}Ge_{30}$ that showed a much higher phonon lifetime than expected from its low thermal conductivity [42, 43]. They suggested that the actual influence of the guest atom is to lower the velocity of the acoustic phonons

by making the acoustic branches very flat through hybridization rather than providing a distinct local scattering mechanism. But this might only work for systems with small off-center displacement. For Sr or Eu clathrates with much bigger off-center displacement, a different phonon dispersion relation will show up [20], that would not exclude the rattling effect.

4. Zintl phase

Zintl phases were named for the German chemist Eduard Zintl. They are made up of electropositive cations and electronegative anions,where anions form a complex of bonds in order to satisfy valence [44, 45]. Although Zintl phases are usually considered to be semiconductors, the semiconducting band gaps can diminish and show metallic conductivity in many cases.

Zintl phases are prime candidates for applying this concept to obtain high zT thermoelectric materials because of their semiconducting properties and complex structures. Our group has performed some studies on the Zintl phase materials, such as Ba-Al-Ge clathrates [46], and in this work we also investigated some Zintl phases related to the clathrates.

5. NMR properties

Nuclear magnetic resonance (NMR) is another method for the investigations of materials, including clathrates. It has been used for dynamical studies, structure determination, electronic structure analysis and many other purposes [47, 48, 49, 50]. Our group have has performed studies on several of the group IV clathrates using our NMR system [51, 52, 53, 54, 40]. Dr. Weiping Gou, one of our former group members investigated the atomic slow motion for the $Sr_8Ga_{16}Ge_{30}$ clathrate from the NMR spectrum and relaxation behavior [51]. Dr. Sergio Rodriguez, another group

member of ours, did structure *ab-initio* calculations on many clathrate samples based on NMR results [55, 54]. I also did many NMR measurements on clathrates and related materials, and I will discuss these results in the following chapters.

CHAPTER III

SOLID STATE NMR THEORIES AND TECHNIQUE

Nuclear Magnetic Resonance (NMR) was first introduced by Rabi in 1938 in molecular beam measurements. In 1946, Bloch and Purcell refined the technique for use on liquid and solids. It was first used to detect radio frequency (RF) absorption, but after many decades' development, NMR became widely used in many fields such as physics, chemistry, biology, medical examination. It is now considered as one of the most powerful techniques for scientific research [56, 57].

A. Basic principle in NMR

For NMR purposes, nuclei can be considered as combinations of many particles with a fixed total magnetic moment $\vec{\mu}$ and angular momentum $\hbar\vec{I}$. We have the relationship $\vec{\mu} = \gamma_n \hbar \vec{I}$, where γ_n is the nuclear gyromagnetic ratio. When placed in an external magnetic field $\vec{H}$ the Hamiltonian due to the Zeeman effect is

$$\mathcal{H} = -\vec{\mu} \cdot \vec{H} = -\gamma_n \hbar H_0 I_z \tag{3.1}$$

with eigenvalues

$$E_m = -m\gamma_n \hbar H_0, m = -I, -I+1, ..., I. \tag{3.2}$$

Due to the existence of the energy difference between energy levels, it is possible to observe an absorption spectrum by applying a RF pulse with a proper frequency ω_0 that satisfies $\hbar\omega_0 = \Delta E = \gamma_n \hbar H$, where $H = H_0 + H_{loc}$ includes both the external field and local environment.

B. Relaxation time and equation of motion

Applying an external magnetic field $\vec{H}$ to a nuclear spin system, with a magnetization $\vec{M}$, will produce a torque $\vec{M} \times \vec{H}$ to force $\vec{M}$ to precess about $\vec{H}$. Writing the equation of motion in the laboratory frame and including exponential relaxation processes, we obtain

$$\begin{aligned} \frac{dM_{x,y}}{dt} &= \gamma_n(\vec{M} \times \vec{H})_{x,y} - \frac{M_{x,y}}{T_2}, \\ \frac{dM_z}{dt} &= \gamma_n(\vec{M} \times \vec{H})_z - \frac{M_z - M_0}{T_1}, \end{aligned} \tag{3.3}$$

where $\vec{M_0}$ is the equilibrium magnetization, T_1 is spin-lattice relaxation time and T_2 is the spin-spin relaxation time. From an analysis of the T_1 and T_2, it is possible to quantify the atomic motion or even transport properties.

C. Knight shift and Korringa relation

The Knight shift is named after Professor Walter Knight, who first observed the phenomenon in ^{63}Cu NMR for metallic copper, where the shift is an order of magnitude larger than the chemical shifts [58]. Later, this was found to be typical for metallic materials [59]. Considering the interaction between a nucleus and a free electron, there are three terms that need to be considered: the Fermi contact interaction, magnetic dipole interaction and angular momentum interaction. The Hamiltonian describing the interactions between the nucleus and conduction electrons can be expressed as:

$$\mathcal{H} = 2 \cdot \frac{8\pi}{3}\mu_B\gamma_n\hbar\vec{I} \cdot \vec{S}\delta(\vec{r}) - 2\mu_B\gamma_n\hbar\vec{I} \cdot \left[\frac{\vec{S}}{r^3} - \frac{3\vec{r}\left(\vec{S} \cdot \vec{r}\right)}{r^5}\right] - \gamma_n\hbar\frac{e}{mc}\left[\vec{I} \cdot \frac{(\vec{r} \times \vec{p})}{r^3}\right] \tag{3.4}$$

where μ_B is the Bohr magneton, γ_n is the gyromagnetic ratio, $\vec{I}$ and $\vec{S}$ are the nuclear spin and electron spin respectively, $\vec{r}$ is the radius vector of the electron with the nucleus at the origin [59].

The first term of equation (3.4) is the Fermi contact term, which is usually used to explain Knight shift in a simple metal. The second term describes the spin-dipole interaction, which is a source for NMR lineshape broadening for powders. The last term represents the spin-orbit interaction, which is usually important in transition metals and contributes to the anisotropic Knight shift.

If we just consider s-state electrons, only the Fermi contact term will survive after taking an average over the electron wave function. By assuming the external field is in the z direction, the effective Fermi contact interaction can be written as [56]

$$\mathcal{H} = -\gamma_n \hbar I_z \left(\frac{8\pi}{3} \left\langle |\Phi_s(0)|^2 \right\rangle_{E_F} \chi_P H_0 \right), \tag{3.5}$$

where χ_P is the Pauli paramagnetic spin susceptibility and $\Phi_S(0)$ is the electron wave function measured at the nucleus. This energy can be treated as a small perturbation of the external field (ΔH) and will lead to a small resonance frequency shift, called the Knight shift, as below:

$$K = \frac{\Delta H}{H_0} = \frac{8\pi}{3} \left\langle |\Phi_s(0)|^2 \right\rangle_{E_F} \chi_P. \tag{3.6}$$

If one expresses the relationship between the experimental resonance frequency ν_m in a metal and the resonance frequency ν_d in a diamagnetic reference as

$$\nu_m = \nu_d + \Delta\nu, \tag{3.7}$$

there are four standard facts for this phenomenon [56]:

(1). $\Delta\nu$ is always positive.

(2). $\Delta\nu/\nu_d$ is unaffected by external field change.

(3). $\Delta\nu/\nu_d$ is nearly temperature independent.

(4). $\Delta\nu/\nu_d$ increases with increasing nuclear charge.

For metallic materials, conduction electrons will control the relaxation mechanism and only electrons at the Fermi level need to be considered. In this case, the Korringa relation can be derived from the Fermi contact interaction and gives an expression

$$K^2 T_1 T = \frac{\hbar}{4\pi k_B} \frac{\gamma_e^2}{\gamma_n^2} \tag{3.8}$$

where γ_e is the electron gyromagnetic ratio and k_B is the Boltzmann constant. Note that this is only correct for metallic materials, and the relationship is more complicated for semiconductors. The Korringa ratio can also be affected by a number of sources, such as electron-electron interactions, and exchange enhancement. So, although a constant behavior can be observed, the $K^2 T_1 T$ value is not necessary to be exactly the same as calculated from the equation above [52, 51].

D. Chemical shift and shielding

Nuclei are always surrounded by an electron cloud which interacts with the nuclear spin angular momentum. The surrounding electrons will build up a magnetic shield around the nuclei and affect the spin energy levels by a small amount. The change of nuclear magnetic resonance frequencies for the same kind of nucleus, due to variations in the electron distribution, is called the chemical shift. The Hamiltonian term associated with this chemical shift is simply a Zeeman operator [60],

$$\mathcal{H}_{CS} = -\vec{I} \cdot \vec{\sigma} \cdot \vec{B}_0, \tag{3.9}$$

where $\vec{\sigma}$ is the chemical shift tensor.

For solid state environments, the Hamiltonian for axial conditions is

$$\mathcal{H}_{CS} = -\sigma_i \omega_0 I_z - 1/2(3cos^2\theta - 1)(\sigma_{zz} - \sigma_i)\omega_0 I_z \tag{3.10}$$

where $\sigma_i = 1/3(\sigma_{xx} + \sigma_{yy} + \sigma_{zz})$ is the isotropic chemical shift given by the diagonal sum of the shift tensor $\vec{\sigma}$, and θ is the polar angle between the polarizing field direction and the principal axis of $\vec{\sigma}$. Knight shifts tend to be an order of magnitude larger than the small paramagnetic chemical shift for metallic materials, so that if high accuracy is not required, we can pick a standard reference and define the Knight shift in percentage as:

$$K = \frac{\nu_m - \nu_{ref}}{\nu_{ref}} \times 100\%, \tag{3.11}$$

where ν_m and ν_{ref} are the measured resonance frequencies for the object and the reference under the same external field. This is the method used to define the Knight shift for most of the cases in this work.

E. Dipole coupling and Quadrupole Interactions

In solid state NMR, dipolar coupling and quadrupolar interactions are also important. The dipolar coupling describes the interaction between the dipole moments of different nuclei. The Hamiltonian of the interaction between two magnetic dipoles can be written as

$$\mathcal{H} = -\frac{\mu_0}{4\pi r_{jk}^3}\left(3(\vec{m}_j \cdot \vec{e}_{jk})(\vec{m}_k \cdot \vec{e}_{jk}) - \vec{m}_j \cdot \vec{m}_k\right) \tag{3.12}$$

where $\vec{e}_{jk}$ is a unit vector parallel to the line joining the center of the two dipoles, r_{jk} is the distance between two dipoles, $\vec{m}_k$ and $\vec{m}_j$. For two interacting nuclear spins,

this can be expressed by

$$\mathcal{H} = -\frac{\mu_0}{4\pi}\frac{\gamma_j\gamma_k\hbar^2}{r_{jk}^3}\left(3(\vec{I_j}\cdot\vec{e}_{jk})(\vec{I_k}\cdot\vec{e}_{jk}) - \vec{I_j}\cdot\vec{I_k}\right) \tag{3.13}$$

where γ_j and γ_k are gyromagnetic ratios of the two nuclei with spin $\vec{I_j}$ and $\vec{I_k}$.

The direct dipole coupling is useful for structural studies. Estimation of this coupling provides a direct spectroscopic route to the distance between nuclei and hence the geometrical form of the molecule, or additionally also on intermolecular distances in the solid state leading to NMR crystallography notably in amorphous materials. Although internuclear magnetic dipole couplings contain a great deal of structural information, in isotropic solutions, they average to zero as a result of rotational diffusion. In addition, the pseudo-dipolar interaction often can be large, which may need further consideration.

Quadrupolar effects have to be taken into consideration when $I > 1/2$. For $I = 1/2$ the average quadrupole interaction is zero in any crystallographic environment so that no quadrupole effects are seen in the NMR spectra. When $I > 1/2$, the charge distribution is no longer spherical, and can interact with an electric field gradient to produce a change in the energy levels in addition to the Zeeman effect, as shown in Fig. 4. The interaction energy E of a charge distribution of density ρ with a potential V can be expressed as

$$E = \int \rho V d\tau, \tag{3.14}$$

and the leading term in its expansion gives the the effective quadrupolar Hamiltonian $\mathcal{H}_Q$,

$$\mathcal{H}_Q = \frac{eQ}{6I(2I-1)}\Sigma_{\alpha\beta}V_{\alpha\beta}\left[\frac{3}{2}(I_\alpha I_\beta + I_\beta I_\alpha) - \delta_{\alpha\beta}I^2\right], \tag{3.15}$$

where $V_{\alpha\beta}$ is the field gradient and Q is the quadrupole moment of the nucleus [56].

The frequency shift of NMR transitions can also be calculated from equation (3.15) as a series of perturbations for the case that the eigenvalues of equation (3.15) are small compared to $\hbar\omega_0$. For example, the first order quadrupolar effect for high symmetry systems gives

$$\nu(m \leftrightarrow m-1) = \nu_0 + 1/2\nu_Q(3\mu^2 - 1)(m - 1/2), \tag{3.16}$$

where m is the energy level, $\mu = cos(\theta)$ and $\nu_Q = \frac{3e^2qQ}{2I(2I-1)h}$ is the pure quadrupolar frequency with $eq = V_{zz} = \partial^2 V/\partial z^2$, the $z - z$ term of the field gradient [59]. This indicates that the central transition ($m = 1/2$) will not be shifted by the first order quadrupole effect. But higher order quadrupolar effects, most importantly the second order, will still bring additional changes to the frequency shift. For the cases with axial symmetry or higher, the effect can be described as

$$\nu(m \leftrightarrow m-1) = \nu_0 + 1/2\nu_Q(3\mu^2 - 1)(m - 1/2) + \frac{\nu_Q^2}{32\nu_0}(1 - \mu^2) \times \tag{3.17}$$
$$\{[102m(m-1) - 18I(I+1) + 39]\mu^2 - [6m(m-1) - 2I(I+1) + 3]\}$$

F. NMR Pulse Sequences

The most commonly used pulse sequences in our work are based on the spin-echo sequence, which is usually used for simple resonance frequency mapping. This sequence is shown in Fig. 5. With proper combinations of multiple spin-echo sequences and variable parameters, we can construct T_1 and T_2 sequences to obtain relaxation properties.

In this work, we use the RF pulse sequence ($-180^o - T_{wait} - 90^o - T_{Delay} - 180^o - T_{wait}-$) to measure the spin-lattice relaxation time, T_1. With the results corresponding to different T_{wait}, we are able to get a T_1 value from the fit of the

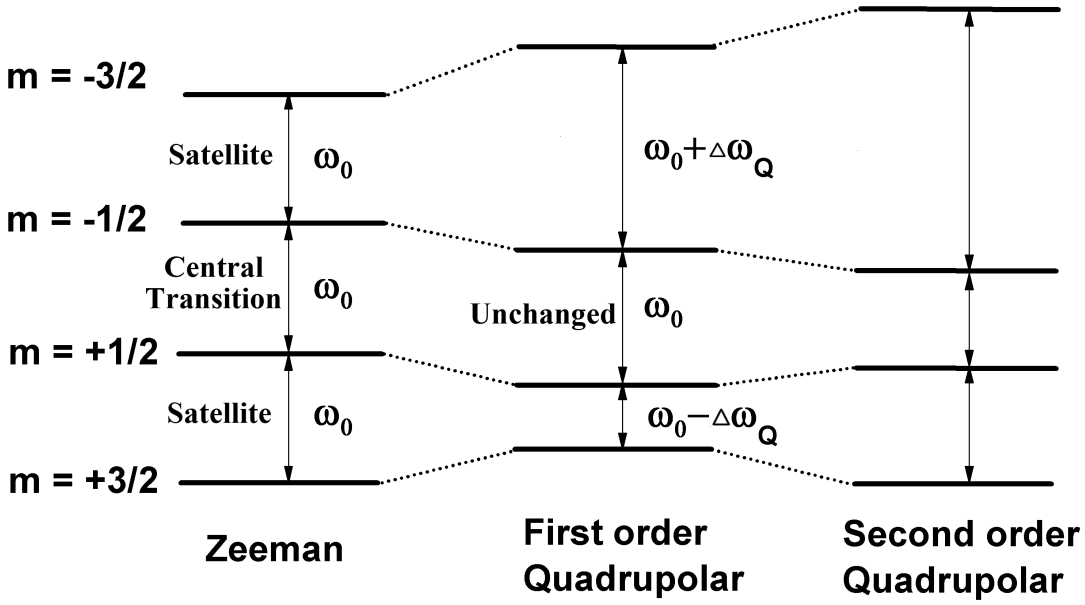

Fig. 4. Energy levels with quadrupole interaction in spin 3/2 system.

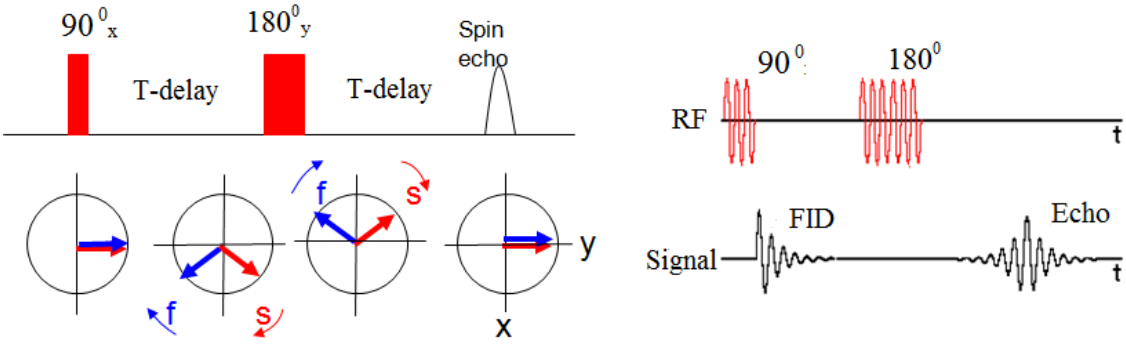

Fig. 5. Example of Spin-Echo sequence.

magnetization recovery curve. For nuclei with spin 3/2, like Ga, the central transition recovery curve for the magnetic contribution is given as

$$M(T_{wait}) = M(0)\left[1 - B\left(0.1e^{-\frac{T_{wait}}{T_1}} + 0.9e^{-\frac{6T_{wait}}{T_1}}\right)\right], \tag{3.18}$$

and for nuclei with spin 5/2, such as Al, the corresponding recovery curve is given as

$$M(T_{wait}) = M(0)\left[1 - B\left(0.028e^{-\frac{T_{wait}}{T_1}} + 0.178e^{-\frac{6T_{wait}}{T_1}} + 0.793e^{-\frac{15T_{wait}}{T_1}}\right)\right], \tag{3.19}$$

where $M(0)$ is the fitted initial magnetization and B is a fitted amplitude.

For the measurement of T_2, we change the T_{Delay} time between the 90 and 180 degree pulses in the spin-echo sequence and record the corresponding signal intensity. The value of T_2 can be fitted from the function

$$M(2T_{Delay}) = M_0\left[\alpha e^{-\frac{2T_{Delay}}{T_{2e}}} + e^{-\left(\frac{2T_{Delay}}{T_{2g}}\right)^2}\right], \tag{3.20}$$

where T_{2e} and T_{2g} represent the relaxation times for exponential and Gaussian contributions, and α describes the ratio between these two components.

G. Magic Angle Spinning NMR

Magic Angle Spinning (MAS) was first introduced in 1958 by Andrew, Bradbury, and Eades [61]. The purpose of using this technique in NMR is to make the normally broad lines become narrower in order to get higher resolution spectrum.

In ordinary NMR experiments, the sample is fixed inside the sample coil, which is perpendicular to the external magnetic field. The nuclear spins of the sample will experience orientation dependent interactions such as dipole-dipole coupling, anisotropic chemical shifts and quadrupole interactions. These interactions will lead to broadening of the NMR peaks which will reduce the resolution of the spectrum. According

to the Hamiltonian of the spin system, the dipole-dipole and first order quadrupolar interactions have an angular dependence connected to the second rank spherical harmonic, which has an angular dependence of $3cos^2(\theta) - 1$. In order to reduce such interactions, it is best to set $3cos^2(\theta) - 1 = 0$, which gives the magic angle of $\theta = 54.7^o$. Rapidly spinning the entire sample about an axis at this magic angle to the external field will average out most of these interactions and make the NMR peaks narrower.

CHAPTER IV

EXPERIMENTAL APPARATUS

A. NMR Spectrometer

NMR experiments in this work were performed using a home-made NMR pulse spectrometer, which could cover a temperature range from 4.2 K to 500 K. The major components of our NMR instrument are: a field-adjustable superconducting magnet, the pulse sequence generator (PSG), the RF synthesizer, transmitters, signal receivers, the detecting probe, the cryostat system and the controlling system based on a Labview program. The details are shown in Fig. 6

While executing a certain pulse sequence, the RF is produced by a frequency synthesizer, and the PSG is used to control the pulses. The transmitter is used to deliver the RF radiation to the sample to perturb the nuclear spin system from its equilibrium state. During the relaxation process of the spin system, an electric signal can be recorded from the pick-up coil. The receiver detects, amplifies, and digitally records the signal. Normally the voltage induced in the pick-up coil is as low as one microvolt, and it has to be amplified before being digitally recorded by the computer.

The circuit of the probe is basically a tunable LC circuit, and the sample coil serves as the inductor of the LC circuit. It is used to excite and detect NMR signals from the sample inside the coil. There is a general requirement that all components must be non-magnetic. There are also many other add-ons to the probe for additional functions. A Cu-Ni thermocouple is attached inside the sample can for temperature detection from 60 K to 400 K, but it does not work well at lower temperatures. Therefore a calibrated thermometer is also located next to the sample coil for temperature measurement at lower temperatures, in the range from 4.2 K to 70 K, but its reading

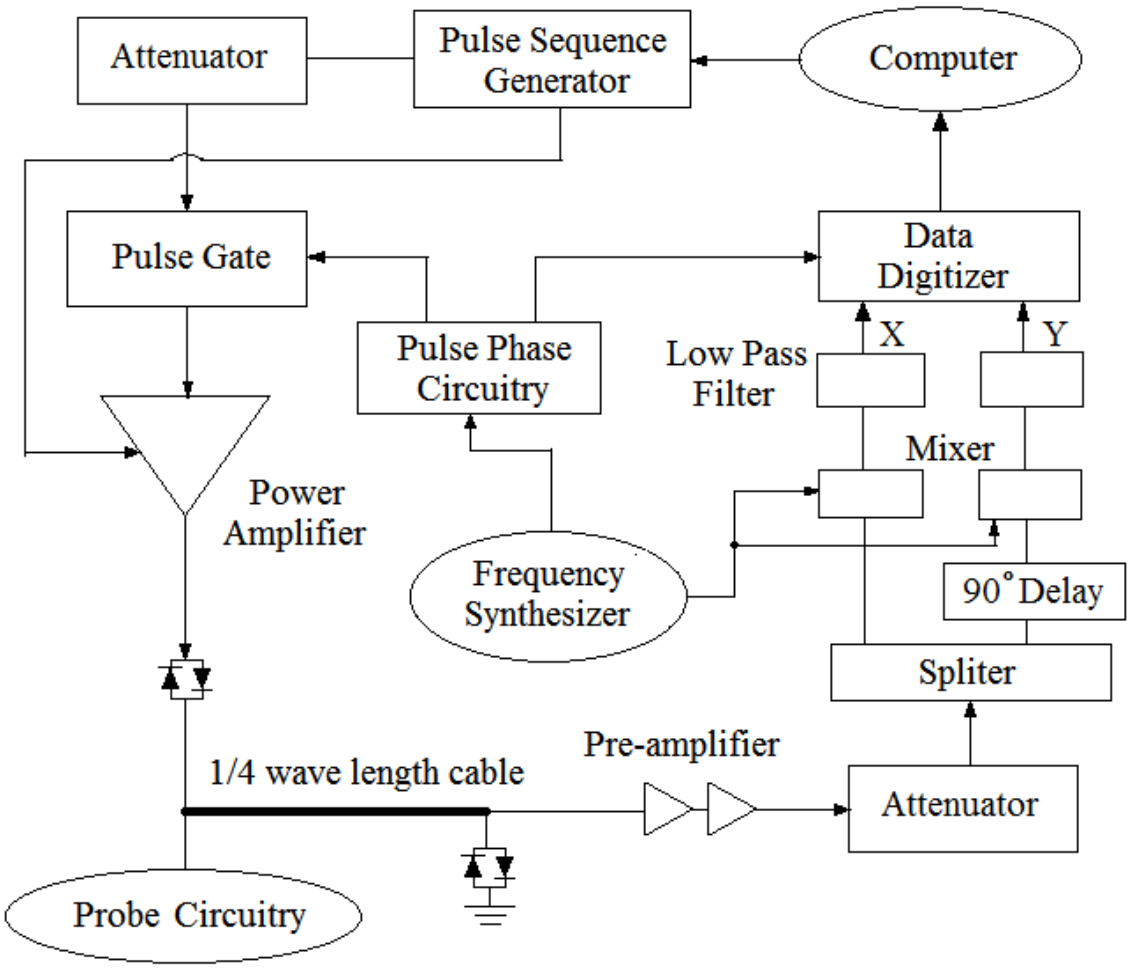

Fig. 6. NMR control and receiving circuit.

is less sensitive at higher temperatures. A home-made resistance heater, a Cu-Ni wire, is attached to the sample can of the probe for temperature adjustment. Two other thermometers are located along the probe support shaft to measure the helium level inside the probe chamber when measurement at 4.2 K is needed. In this work, I have made and rebuilt four probes, which have been used for Ga, Cu, In and Al NMR measurements.

A cryostat system is needed to perform low temperature NMR. In our case, liquid nitrogen was used to perform measurements from 77 K to 300 K, while liquid helium was used for the range from 4.2 K to 77 K respectively. The NMR field was calibrated using corresponding liquid samples. For example, we used a dilute $Ga(NO_3)_3$ solution as zero-shift reference for Ga NMR, and a dilute $AlCl_3$ solution for Al/Cu NMR. The samples for NMR measurements were several cubic millimeters of powder mixed with quartz powder.

Magic Angle Spinning (MAS) measurements on Ga based samples were performed at the NMR facility in the Chemistry Department, using a Bruker Avance 400 MHz NMR instrument with $Ga(NO_3)_3$ as reference.

B. PPMS, X-ray and WDS

A Physical Property Measurement System (PPMS) from Quantum Design was used for measurements of resistivity and specific heat in this study. Resistivity was measured by a 4 probe method in the temperature range from 2 to 300 K, and the specific heat was measured in the same temperature range.

X-ray diffraction (XRD) measurements were performed on a Bruker D8 X-ray Powder Diffractometer in the Chemistry Department. Wavelength dispersion spectroscopy (WDS) measurements were done in a Cameca SX50 spectrometer in the

Geology Department. All of these were performed at room temperature. All WDS results were performed by Laziz Saribaev, one of our group members.

C. Computational package and coding program

$Ab - initio$ calculations on density of states, band structures, optimized structures, electric field gradients and many other properties were carried out using in the WIEN2k package [55, 54]. Generalized Gradient Approximation (GGA) was used to simulate the NMR spectrum to compare with the experimental results [54]. All these calculations were performed by Dr. Sergio Rodriguez and Jing-Han Chen, members of our group. The fitting programs for NMR relaxation, resistivity and heat capacity were written and operated in C/C++ and FORTRAN by myself.

D. Sample preparation

Most of the samples discussed in this work are prepared by an arc-melting method followed by proper annealing processes. The $Ba_8Ga_{16}Sn_{30}$ samples, some $Ba_8Cu_xGe_{46-x}$ samples and the layered $BaGa_3Sn$ sample were prepared by Dr. Sergio Rodriguez. The $Ba_8In_{16}Ge_{30}$ and layered $BaGa_4$ samples were prepared by Laziz Saribaev. The $Ba_8Ga_{16}Ge_{30}$ sample was from a previous study by Dr.Weiping Gou. I made the $Ba_8Cu_xGe_{46-x}$ sample with $x = 5.3$.

CHAPTER V

EXPERIMENTAL RESULTS AND DISCUSSIONS

In this work, several different materials have been studied. Most of them are clathrate materials, such as type-I and type-VIII $Ba_8Ga_{16}Sn_{30}$, type-I $Ba_8In_{16}Ge_{30}$, $Ba_8Cu_xGe_{46-x}$ and $Ba_8Ga_{16}Ge_{30}$. There are also other group IV materials which are not clathrates but still interesting, such as the layered $BaGa_3Sn$ and $BaGa_4$. NMR, PPMS, X-ray, as well as other methods have been used for the investigations.

A. Type-I $Ba_8Ga_{16}Sn_{30}$*

Type-I $Ba_8Ga_{16}Sn_{30}$ clathrate is considered to be one of the possible candidates as new generation thermoelectric materials for applications because it has been reported to have one of the lowest thermal conductivities for a bulk thermoelectric material [23]. Due to the cage structure, the Ba guest atoms are believed to exhibit anharmonic motion, which may be a primary reason for the low thermal conductivity. Previous structural studies have also shown large guest atom off-center displacements for this material, which may support the anharmonic assumption. In this work, NMR, transport and heat capacity measurements have been performed on this material. A double well potential model [33, 40] has been used for the analysis on NMR, transport and heat capacity behaviors. Most of the content in this section has been published

---

*Part of this chapter is reprinted with permission from "NMR relaxation and rattling phonons in the type-I $Ba_8Ga_{16}Sn_{30}$ clathrate" by X. Zheng, S. Y. Rodriguez, and J. H. Ross, Jr., 2011, *Phys. Rev. B*, vol. 84, no. 2, pp. 024303, ©(2011) by The American Physical Society.

Part of this chapter is reprinted with permission from "Transport and thermodynamic properties under anharmonic motion in type-I $Ba_8Ga_{16}Sn_{30}$ clathrate" by X. Zheng, S. Y. Rodriguez, L. Saribaev and J. H. Ross, Jr., 2012, *Phys. Rev. B*, vol. 85, pp. 214304 ©(2012) by The American Physical Society.

[40, 54, 62].

1. Sample preparation

Both the type-I and the type-VIII $Ba_8Ga_{16}Sn_{30}$ samples for this work were prepared by Dr. Sergio Rodriguez, using the self-flux method, following a technique reported previously [35, 54]. Because of the existence of a type-I/type-VIII dimorphism in $Ba_8Ga_{16}Sn_{30}$, a carefully controlled annealing process is needed. For type-I $Ba_8Ga_{16}Sn_{30}$, the pure elements were mixed together based on the nominal composition followed by an initial arc melting in an argon environment. The sample then was annealed in an evacuated quartz tube at 900 °C for 50 hours, followed by a controlled slow cooling to 500 °C in 80 hours [35, 54]. X-ray diffraction (XRD) measurements and wavelength dispersion spectroscopy (WDS) measurements were then performed. Rietveld refinements of the XRD results were performed using EXPGUI [63].

These XRD and WDS measurements indicated that all samples consist of a type-VIII or type-I major phase, with a small $Ba(Ga,Sn)_4$ minor phase as well as a small amount of remaining Sn and Ga flux. The $Ba(Ga,Sn)_4$ amount is such that only about 1% of Ga atoms occur in this phase, giving negligible contribution to the NMR measurements. No evidence was found for coexistence of type-I and type VIII clathrate structures in these samples. Assuming the framework sites are completely full, the WDS results gives a composition of $Ba_{7.80}Ga_{16.15}Sn_{29.85}$ for the type-I sample. If we assume that the framework occupation is similar to the sum of the Ga and Sn atoms from Rietveld XRD refinements, the composition is $Ba_{7.64}Ga_{16.00}Sn_{29.58}$. This indicates some vacancies on Ba and Sn, which leads to a p-type configuration. Thus, the WDS and XRD results are consistent [54].

2. NMR results and discussion

NMR experiments were carried out under external magnetic fields of 8.8 T and 7 T in a temperature range from 4.2 K to 295 K using the NMR system introduced previously. The nuclei measured are ^{71}Ga and ^{69}Ga with different gyromagnetic ratios γ and quadrupole moments Q, where $^{71}\gamma$ = 8.1355 rad/s G^{-1}, $^{69}\gamma$ = 6.4208 rad/s G^{-1} [59], ^{71}Q = 10.7 fm^2, and ^{69}Q = 17.1 fm^2 [64]. The inset to Fig. 7 shows the ^{71}Ga NMR central transition lineshapes at 295 K, 77 K and 4.2 K in 8.8T. No significant change in average shift vs. temperature has been observed in the spectrum. The small changes at the base of the lineshape vs. temperature are caused by unreacted Ga metal. From the plot, the ^{71}Ga central transition peak is not a simple peak but has some detailed structure, which can be caused by the distribution of multiple sites of Ga atoms or quadrupole splitting [54]. Further studies of the quadrupole broadening of the spectrum have been perfermed at 77 K for ^{71}Ga, as shown in Fig. 8, which contains the full quadrupole spectrum. The background broadening is caused by the first order quadrupole effect, and a closer look is shown in the inset of Fig. 8. As reported previously [54], Dr. Sergio Rodgriguez also performed computational modeling for the NMR spectrum, including modeling the first-order quadrupole broadening at the base of the lineshape. The parameters come from *ab-initio* calculations for various distributions of framework atom occupation. The results agreed with the experimental data quite well and were able to provide new insight into the site occupation by Ga and Sn in this material [54].

Here we consider only the behavior at the center of the resonance. The weighted center shift of this resonance is 0.033% at 295 K. For comparison, the ^{69}Ga lineshape under the same conditions, has a weighted shift of 0.023%. The shift includes magnetic, quadrupole and chemical shift terms, which can be expressed as

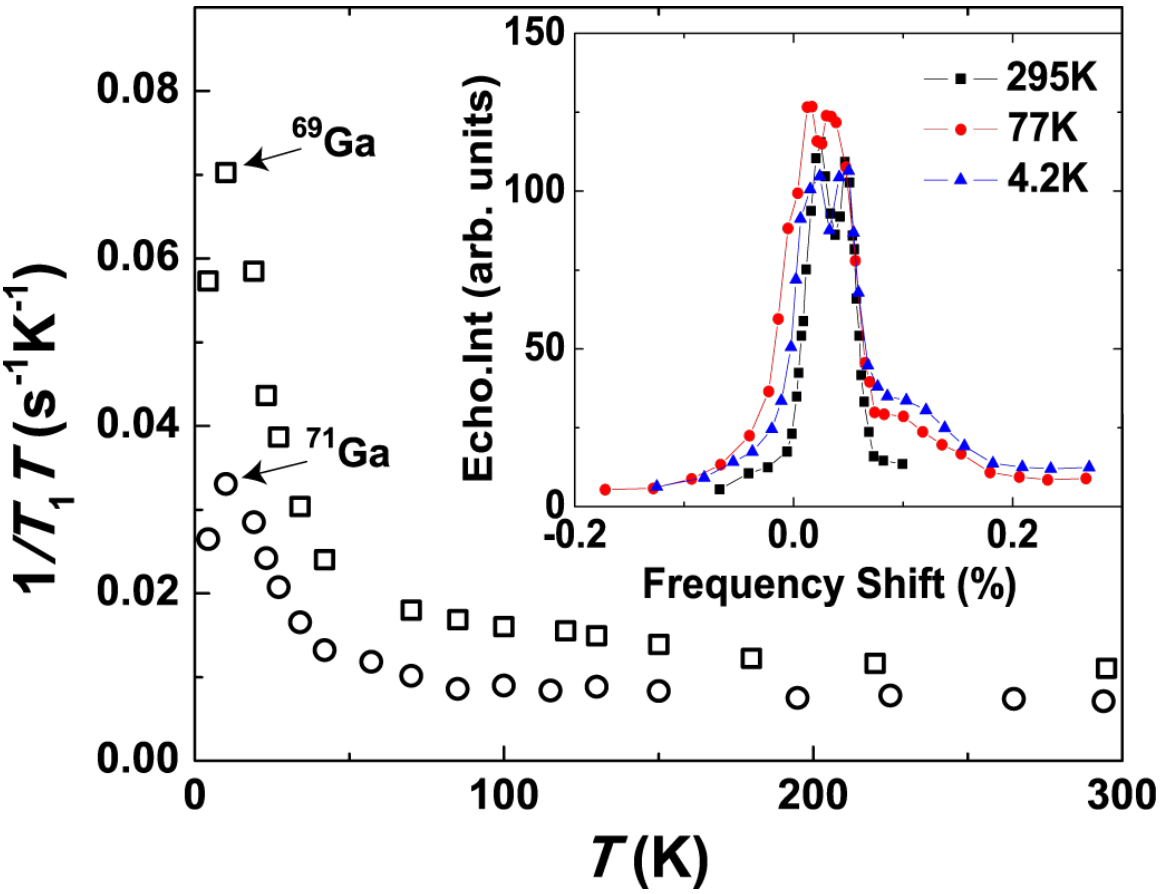

Fig. 7. ^{71}Ga and ^{69}Ga NMR spin-lattice relaxation rates for type-I $Ba_8Ga_{16}Sn_{30}$ at the central transition frequency under 8.8 T from 4.2K to 295 K. Inset: ^{71}Ga NMR lineshapes at temperatures 4.2 K, 77 K and 295 K, scaled proportional to $1/T$.

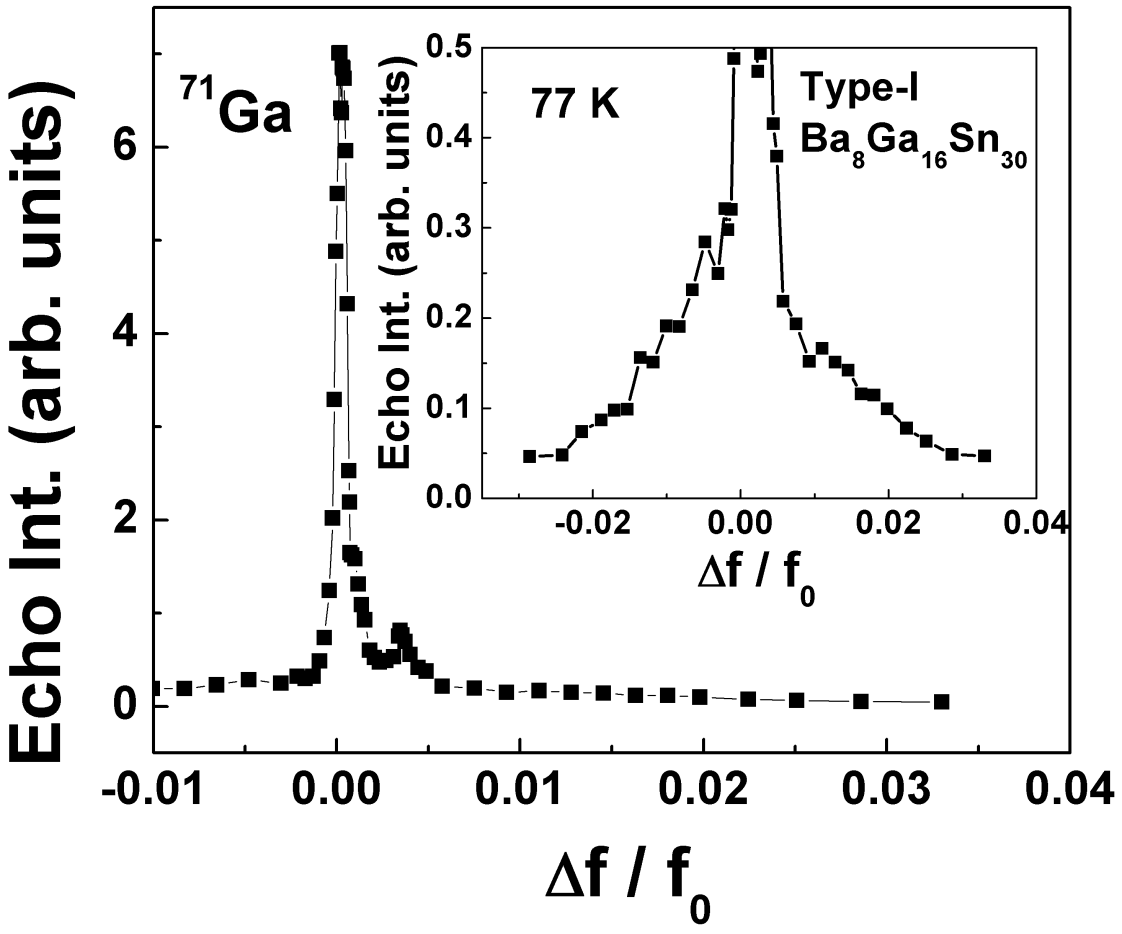

Fig. 8. ^{71}Ga NMR lineshape with full quadrupole background at 77 K. Inset: detailed lineshape for the first order quadrupole broadening background.

$\Delta f/f_0 = K + BQ^2/H$, where K includes not only the magnetic shift but also the chemical shift, whereas Q is the quadrupole moment of the nucleus and H is the external field, which is fixed here. From the ^{71}Ga and ^{69}Ga results under 8.8T we extracted $K = 0.039\%$ as the center-of-mass shift and a negative quadrupole shift. In this case K is dominated by Knight shifts due to conduction electrons, with some contribution due to chemical shifts. We will use this K to represent this combined shift for simplicity. Note that we did not observe any significant change in K vs. temperature, such as those observed in Na-Si type II clathrates [49], indicating a lack of excitations involving sharp electronic features in this system.

NMR spin-lattice relaxation measurements were performed at the central transition frequency, which was measured by the mass center of the lineshape. The relaxation time, T_1, is a fitted value based on a magnetic relaxation mechanism using a standard multi-exponential function, equation (3.18), for recovery of the central transition [51, 56]. The quadrupole relaxation process entails a different relaxation function, which however leads only to an overall scaling of the T_1, and does not affect any of the dynamical fitting parameters described below. Although the signal is also a superposition of different framework sites, a single average T_1 was chosen. Fig. 7 shows the resulting rates for both ^{71}Ga and ^{69}Ga under a field of 8.8 T. A clear peak at a temperature around 10 K can be observed for both nuclei.

According to hyperfine relaxation theory [57], if the relaxation mechanism contains only a magnetic part, T_1 should be inversely proportional to γ^2 which gives $^{69}T_1/^{71}T_1 \cong 1.67$, whereas if the quadrupolar relaxation is dominant, T_1 should be inversely proportional to Q^2 which gives $^{69}T_1/^{71}T_1 \cong 0.4$. The calculated isotopic ratio, $^{69}T_1/^{71}T_1$, in 8.8 T is shown in the inset of Fig. 9. The experimental ratio for our sample (close to 0.5) is consistent over a wide temperature range and is close to the quadrupole moment ratio. Thus, the relaxation is mainly dominated by the

quadrupole mechanism, indicating that lattice vibrations are the most important contribution. As our experimental data are a mixture of magnetic and quadrupole parts, it is better to separate them for further investigations. The corresponding relationships are [57],

$$\frac{1}{T_1} = \frac{1}{T_{1Q}} + \frac{1}{T_{1M}} \tag{5.1}$$

$$\frac{1}{T_{1M}} \propto \gamma^2, \frac{1}{T_{1Q}} \propto Q^2 \tag{5.2}$$

where T_1 is the overall experimental relaxation time while T_{1M} and T_{1Q} represent the magnetic and quadrupole parts. Note that, equation (5.2) in our previous publication contains a typo, where Q^2 was written as $1/Q^2$ by mistake [40]. According to equation (5.1) and equation (5.2), the relaxation rates were separated into two contributions as shown in Fig. 10. Again, the result confirms the dominant role of the quadrupole relaxation rate.

As there is no big change in the Knight shift, the values of K^2T_1T do not change much at high temperatures. Therefore the sample appears to follow a Korringa-like relation [57, 65] at high temperatures, which would normally indicate the influence of metallic electrons if $1/T_1$ were magnetic. However a recent model [33] for relaxation dominated by anharmonic localized vibrations also indicates such behavior as a high-temperature limit, along with a low-temperature peak much as observed here. A simulation based on this anharmonic model will be compared with the quadrupolar relaxation rates we have separated.

3. Anharmonic model and fitting

From XRD refinements for $Ba_8Ga_{16}Sn_{30}$, the guest Ba(2) atom has a location probability concentrated near four equivalent off-center positions with off-center dy-

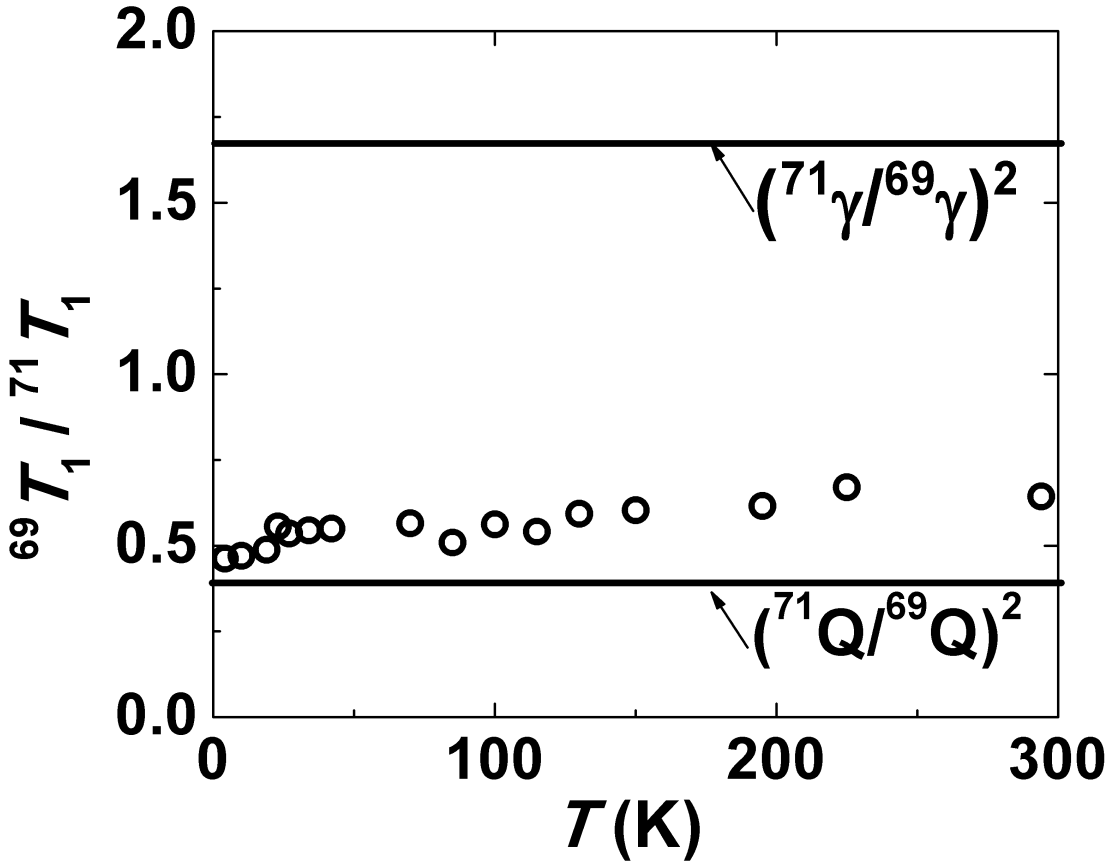

Fig. 9. Isotopic T_1 ratio of type-I $Ba_8Ga_{16}Sn_{30}$ under 8.8 T, with limits for pure quadrupolar/magnetic relaxation indicated.

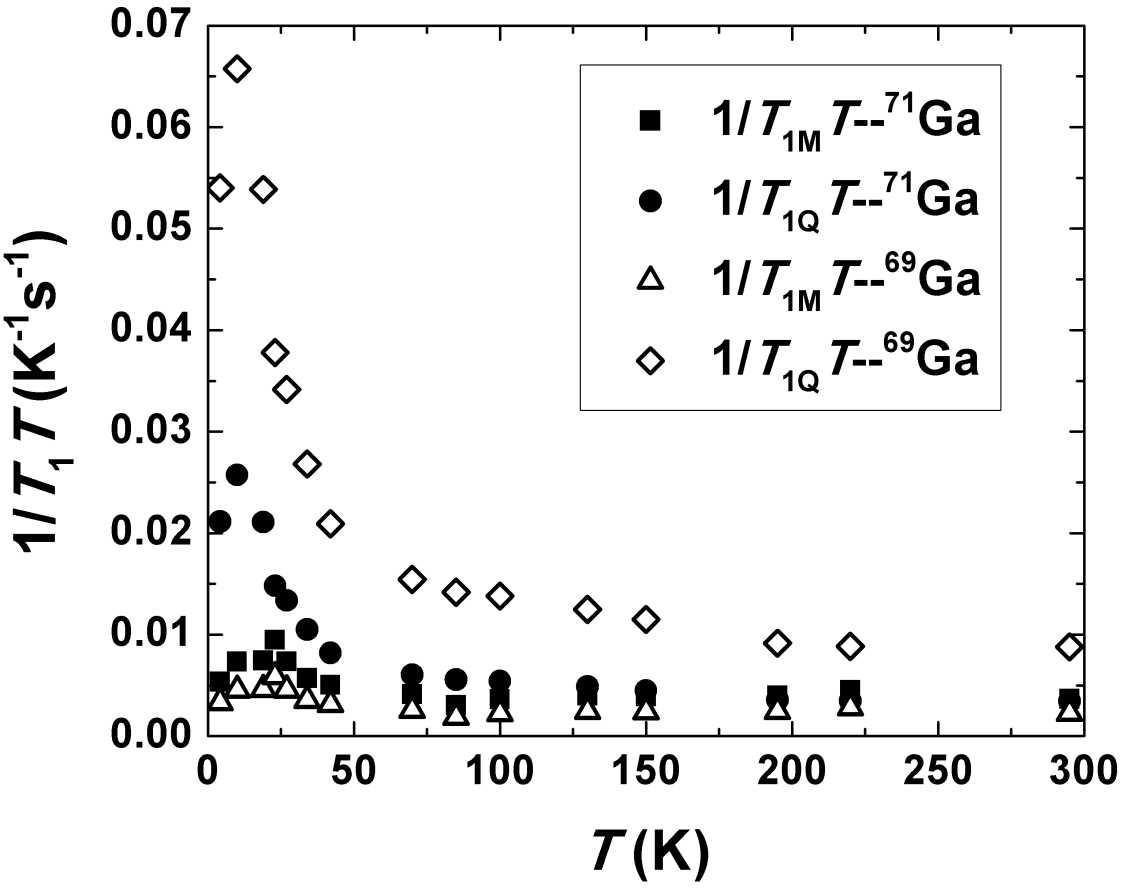

Fig. 10. Separated type-I $Ba_8Ga_{16}Sn_{30}$ T_1 relaxation rates for ^{71}Ga and ^{69}Ga: ^{69}Ga-quadrupole (diamonds, as labeled), ^{71}Ga-quadrupole (circles, as labeled), ^{71}Ga-magnetic (squares), ^{69}Ga-magnetic (triangles).

namic displacements around 0.4 Å[23]. Our previous first principles calculations [54, 55], performed by Dr. Sergio Rodriguez, also gave similar values for the static displacement of the Ba atom due to cage asymmetry. A model including anharmonic dynamics within a 1-D double well potential was introduced by Dahm and Ueda to analyze this kind of problem, and has shown good agreement for the pyrochlore case [33], where the spin-lattice relaxation rate ($1/T_1T$) showed a low temperature peak due to anharmonic contribution and settled down to a constant at higher temperatures. The same model was used here for our simulation. The Hamiltonian used here is,

$$\mathcal{H} = \frac{p^2}{2M} + \frac{1}{2}ax^2 + \frac{1}{4}bx^4 \tag{5.3}$$

where M, p, and x are the mass, momentum and spatial coordinate of the guest atom, Ba [39, 33]. An effective localized phonon frequency, ω_0, and thermal average of x^2 were introduced in a self-consistent quasiharmonic approximation giving $M\omega_0^2 = a + b\langle x^2\rangle_{\omega_0,T}$, where

$$\langle x^2\rangle_{\omega_0,T} = \frac{\hbar}{M\omega_0}\left(\frac{1}{e^{\hbar\omega_0/k_BT}-1} + \frac{1}{2}\right), \tag{5.4}$$

and the relationship between ω_0 and T is given by,

$$\left(\frac{\omega_0}{\omega_{00}}\right)^2 = 1 + \beta\frac{\omega_{00}}{\omega_0}\left(\frac{1}{e^{\hbar\omega_0/k_BT}-1} + \frac{1}{2} - \frac{\omega_0}{2\omega_{00}}\right), \tag{5.5}$$

where $\omega_{00} = \omega_0(T=0)$, and $\beta = b\hbar/M^2\omega_{00}^3$ is a dimensionless anharmonicity factor.

As the observed relaxation is dominated by the quadrupole mechanism, a two-phonon Raman process can be used to describe the NMR relaxation [57]. This can be expressed [33] as

$$\frac{1}{T_1^R} = V_2^2\int_{-\infty}^{\infty} dt\exp\{i\omega_L t\}\langle x^2(t)x^2(0)\rangle$$

$$= 2\pi \left(\frac{\hbar}{2\omega_0 M}\right)^2 V_2^2 \int_{-\infty}^{\infty} d\omega A^2(\omega)[n(\omega)+1]n(\omega) \tag{5.6}$$

with

$$A(\omega) = -\frac{1}{\pi}\mathrm{Im}D(\omega) = \frac{1}{\pi}\frac{4\omega_0\Gamma_0\omega}{(\omega^2-\omega_r^2)^2+4\Gamma_0^2\omega^2} \tag{5.7}$$

where V_2 is the second spatial derivative of the electric field gradient, ω_L is the nuclear Lamor frequency, $A(\omega)$ is the phonon spectral function, $n(\omega)$ is the Bose function, $D(\omega)$ is the retarded phonon propagator, Γ_0 is a phonon damping rate and ω_r^2 is the renomalized phonon frequency determined by the phonon self-energy, $\omega_r^2 = \omega_0^2 + 2\omega_0 \mathrm{Re}\Pi(\omega)$. Here, we assume the real part of the phonon self energy, $\mathrm{Re}\Pi(\omega)$, to be temperature independent as assumed in [33]. By carefully choosing parameters, we obtained a good fit to our data as shown in Fig. 11. These results clearly show that the spin-lattice relaxation can be explained well by the rattling phonon model.

The values of fitted parameters are $\omega_{00} = 20$ K, $\beta = 50$, $\Gamma_0 = 12$ K and $\omega_r(T = 0) = 19.5$ K. The potential well is given by the calculated expression,

$$V(x) = -18.74x^2 + 1.11 \times 10^{23}x^4, \tag{5.8}$$

where $V(x)$ is in J with x given in meters. Also from equations (5.4) and (5.5), when $T = 296$ K, $\omega_0 \cong 11$ THz and $\langle x^2\rangle_{\omega_0,T}^{1/2} \cong 0.12$ Å. Considering $\langle r^2\rangle_{\omega_0,T} = 2\langle x^2\rangle_{\omega_0,T}$ in the case of 2D configuration, this would correspond to a guest atom rms displacement of 0.17 Å, which is not far from the values reported previously [23, 54].

Solving the Schrödinger equation numerically, the energy levels of this double well potential can be calculated as shown in Fig. 12. The energy difference between the lowest two states, $\Delta E_{12} \cong 30$ K, is much smaller than those for higher energy levels, which is similar to recently reported results from other methods [38], but with

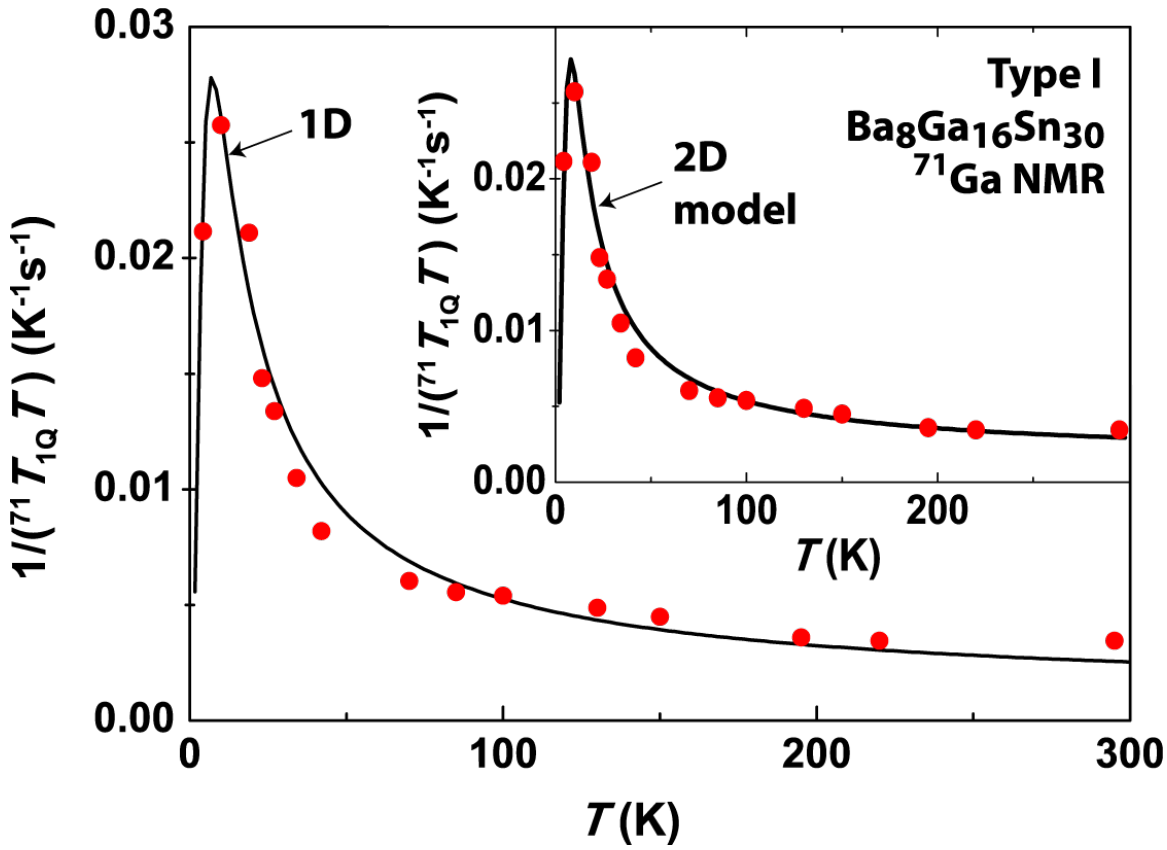

Fig. 11. Quadrupole NMR relaxation rate for ^{71}Ga compared with the fitted 1-D anharmonic model (main plot, solid curve) and simplified 2-D model (inset, solid curve).

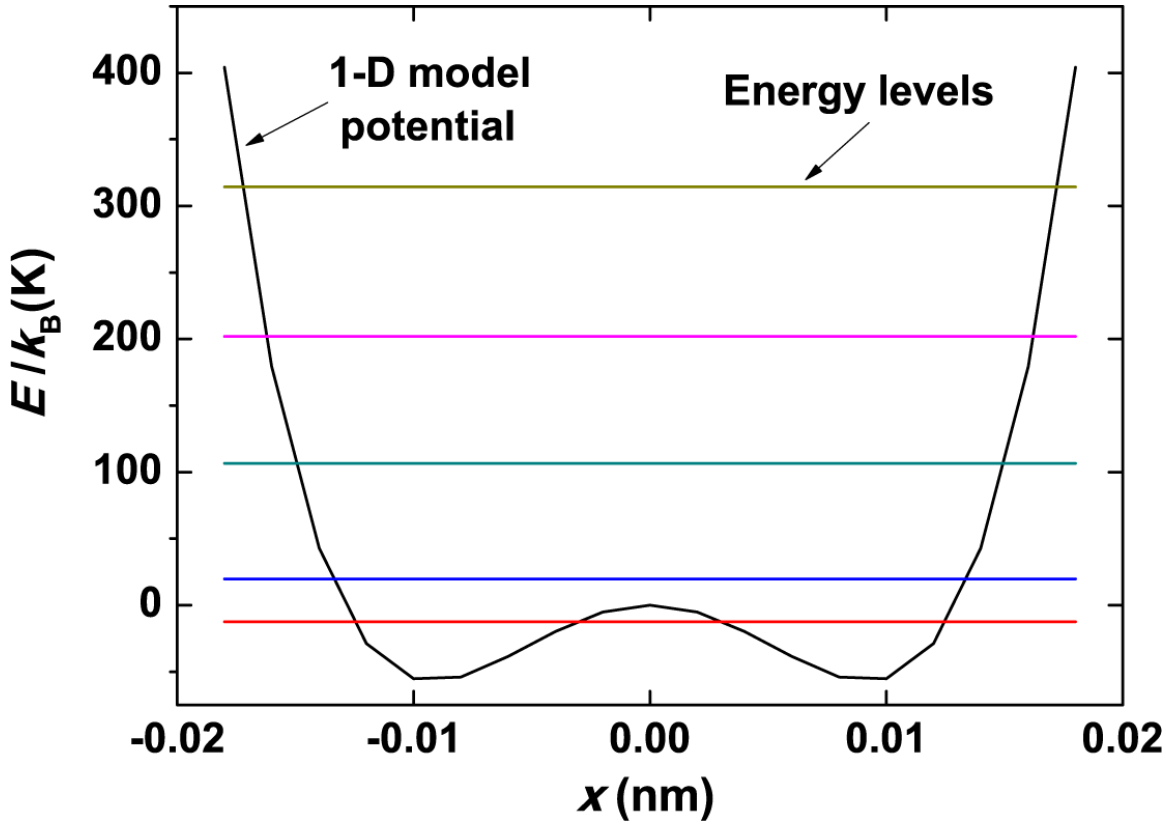

Fig. 12. Fitted 1-D double well potential for type-I $Ba_8Ga_{16}Sn_{30}$ and its lowest energy levels.

a larger ΔE_{12}. This calculated energy levels were used later for the heat capacity analysis. I will discuss this in detail in the following sections.

Previous studies suggested that the off-center rattling behavior should be 2-dimensional, and the corresponding potential would more likely be a four-well potential [41, 23]. I have also used a simplified 2D ring-well potential to investigate this in 2D, as shown in Fig. 13. This simplified 2-D potential used $\langle r^2 \rangle_{\omega_0,T} = \langle x^2 \rangle_{\omega_0,T} + \langle y^2 \rangle_{\omega_0,T} = 2\langle x^2 \rangle_{\omega_0,T}$ instead of $\langle x^2 \rangle_{\omega_0,T}$ in equation (5.4). This is shown in Fig. 13. We correspondingly modified the relationship in equation (5.5). Then, following the same procedure, we obtained a fitting similar to that of the 1-D model. The result is shown in the inset of Fig. 11, with the fitted values $\omega_{00} = 20$ K,

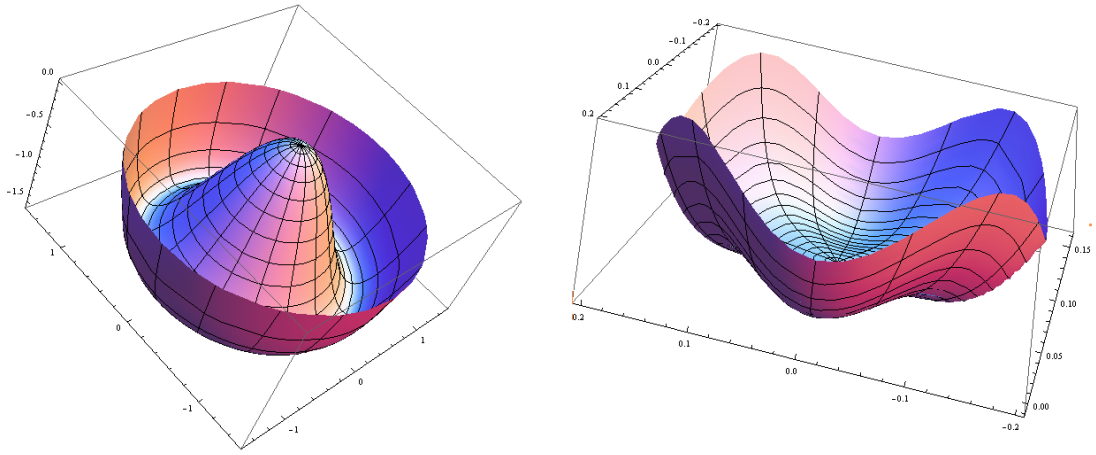

Fig. 13. Simplified ring-shape two dimensional potential well (left) and four-well potential (right).

$\beta = 25$, $\Gamma_0 = 12$ K and $\omega_r(T = 0) = 19.5$ K. The corresponding potential is $V(r) = -8.98r^2 + 5.52 \times 10^{22} r^4$, where $V(r)$ is in J with r given in meters. The average displacement is still 0.17 Å, which indicates a consistency of the model compared with the 1-D case.

The energy levels of the simplified 2D potential well were also calculated, as shown in Fig. 14. These contain certain degeneracies as expected. Later in the heat capacity analysis, I will show that this 2D potential could not give a good fit to the behavior. So, although it is able to offer a good fit to the NMR result, the simplified 2D model may not be the right choice to describe other properties.

Compared to previous Ga NMR results for $Sr_8Ga_{16}Ge_{30}$, also identified to behave as an anharmonic rattler system [11, 37], it seems initially surprising that the $(T_1T)^{-1}$ in $Sr_8Ga_{16}Ge_{30}$ does not show a similar phonon-dominated behavior but instead follows a Korringa law quite closely for several decades of temperature [51]. However, a previous report for Sr-Ge clathrates used density functional theory to extract potential well parameters for Sr in the large cage [37], giving a 2D anharmonic potential much like the model used here. The resulting potential has a very

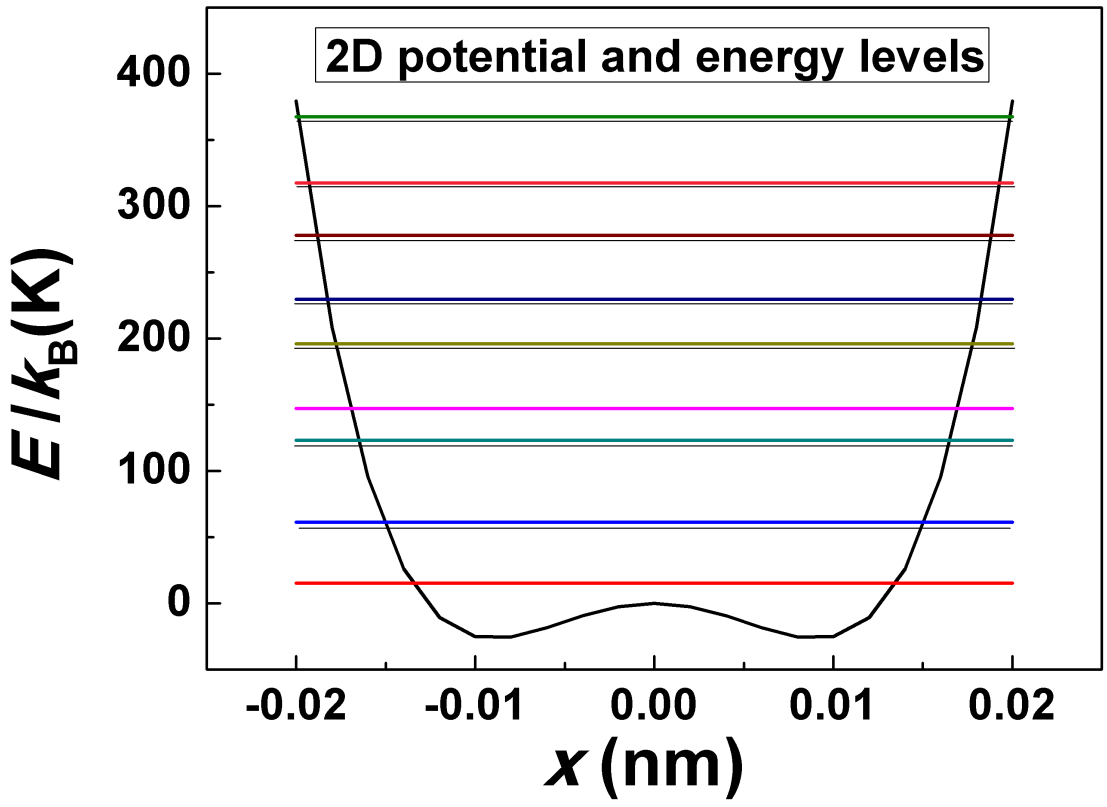

Fig. 14. Energy levels for the simplified ring-shape two dimensional potential well for type-I $Ba_8Ga_{16}Sn_{30}$. Degenerate levels shown with small separations for clarity.

small quadratic term, but also a much smaller anharmonicity parameter (β) than found here, and we find that inserting the calculated parameters into the relaxation theory described above yields a smaller quadrupole contribution to $(T_1T)^{-1}$, rising slowly with temperature without exhibiting a peak as in Fig. 11. Also in the analysis reported for the elastic response of Eu- and Sr-filled Ge clathrates [41] a four-well potential was used to model the vibrational response for Eu, but for Sr a harmonic Einstein oscillator model provided satisfactory agreement. Thus it is consistent that the $(T_1T)^{-1}$ in $Sr_8Ga_{16}Ge_{30}$ is dominated by interactions with the charge carriers, while the quadrupole-dominated peak observed in $Ba_8Ga_{16}Sn_{30}$ is indicative of the much larger anharmonicity for rattler atoms.

In our measurements, we prepared a second sample of type-I $Ba_8Ga_{16}Sn_{30}$ in the same way, and the $1/T_1T$ results for ^{71}Ga from this second sample are shown in Fig. 15, while the $1/T_1$ results are potted in the inset. Its $(^{71}T_1T)^{-1}$ value exhibits a low-temperature maximum that is nearly identical to that of the first sample in Fig. 7. In fitting to the model oscillator potential, the position of the $(^{71}T_1T)^{-1}$ peak is particularly sensitive to ω_{00}, which is close to the spacing of the two lowest levels in Fig. 12. The ability to model this behavior with a single set of parameters attests to the lack of irregularity of the cage potential, despite the presence of quasi-random framework substitution. This is apparently due to the Sn-based cage size, providing space for the relatively unconstrained motion of the Ba(2) atoms without allowing for a permanent distortion [23]. Thus, type-I $Ba_8Ga_{16}Sn_{30}$ can be viewed as possessing a more or less uniform array of strongly anharmonic local oscillators. The NMR relaxation times are particularly sensitive to the low-frequency anharmonic motion of these atoms, and thus provide an excellent probe for this behavior.

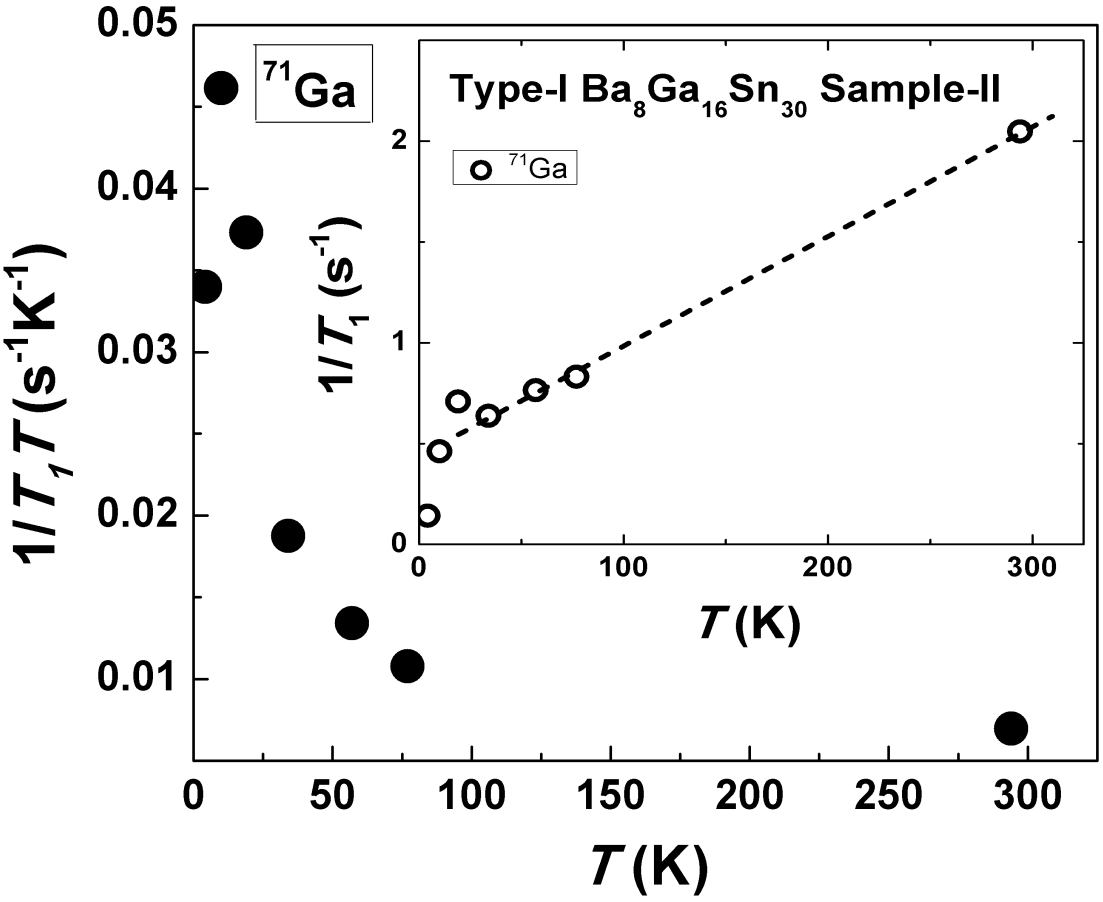

Fig. 15. ^{71}Ga NMR spin-lattice relaxation rates at the central transition frequency in 8.8 T from 4.2K to 295 K for the second sample. The behavior is the same as the first sample. Inset: The corresponding $1/T_1$ values vs. temperature. A linear relation can be observed at high temperatures.

4. Resistivity and modeling

The resistivity was measured in a Quantum Design PPMS system, and the data are plotted in Fig. 16. Note that there is a superconducting jump at about 4 K, which can be associated with the Sn minor phase observed in the XRD result. In this work, only the non-superconducting part will be shown and analyzed, while the superconducting contribution will be removed.

Here, I assume that the majority of the electrical resistivity is caused by the ordinary electron-phonon interaction and follows the standard Bloch-Grüneisen law [66],

$$\rho_B(T) = \rho_0 + A\left(\frac{T}{\Theta_D}\right)^5 \int_0^{\Theta_D/T} \frac{x^5 dx}{(e^x - 1)(1 - e^{-x})}, \tag{5.9}$$

where Θ_D is the Debye temperature, ρ_0 is the residual resistivity and A is a constant. Sometimes this is not sufficient for a system with strong contribution from localized harmonic and anharmonic oscillators. According to Cooper's theory [67], the Einstein contribution is proportional to $C_E T/\Theta_E^2$ as

$$\rho_E(T) = \frac{\alpha C_E T}{\Theta_E^2} = \left(\frac{\kappa}{T}\right) \frac{e^{\Theta_E/T}}{(e^{\Theta_E/T} - 1)^2}, \tag{5.10}$$

where α and κ are constants, C_E is the Einstein contribution to the specific heat and Θ_E is the Einstein temperature. Since Ba atoms exist in two different types of cages for this type-I sample, we should consider two different oscillator behaviors of this type. These local modes are resonances within the phonon bands, however the localized model works relatively well, implying a weak coupling to other lattice models.

We started with a fit including one Bloch-Grüneisen term and two Einstein terms with the results shown in Fig. 16. Here, we define Θ_{E1} and Θ_{E2} as the Einstein tem-

peratures for Ba(1) and Ba(2) atoms. The fitted parameters from standard deviation calculations are $\Theta_D = 230$ K, $\Theta_{E1} = 56$ K, $\Theta_{E2} = 49$ K and $\rho_0 = 243$ $\mu\Omega$ cm. This gives noticeable improvement over the fit with a single Bloch-Grüneisen contribution (not shown). Note that Bloch-Grüneisen term works well for metallic systems and the NMR results described earlier[40] show that a Korringa-like behavior is followed in this material, which is a typical sign of metallic properties. These results therefore agree with each other.

The overall resistivity fit matches the experimental data quite well, but the inset of Fig. 16 shows a mis-match at the low temperature end. Previous studies have shown a T^2 resistivity behavior in low temperatures caused by anharmonic phonons [33, 39], which is close to what is observed here. For example, a fit of the data up to 12 K to a function of the form T^α gives $\alpha = 2.2$. An alternative explanation for the deviation from T^5 resistivity behavior at low temperatures might be semiconducting behavior as expected in low-carrier density systems. For example in non-polar semiconductors [68] acoustic phonon scattering can introduce a term proportional to $T^{1.5}$. On the other hand, as described above, the NMR shifts and magnetic T_1 term provide additional local measures to confirm that the carrier behavior should be regarded as metallic [40]. Combined with the strong evidence for anharmonic rattling observed in the NMR relaxation results, which becomes evident in the same range of temperatures, it seems reasonable to model the observed resistivity behavior according to the anharmonic behavior of the guest Ba(2) atom.

The electrical resistivity due to localized anharmonic phonons has been addressed in recent theoretical work [33, 39] and can be calculated from the electron lifetime (τ), which describes the electron scattering from phonons [66, 13]. The corresponding

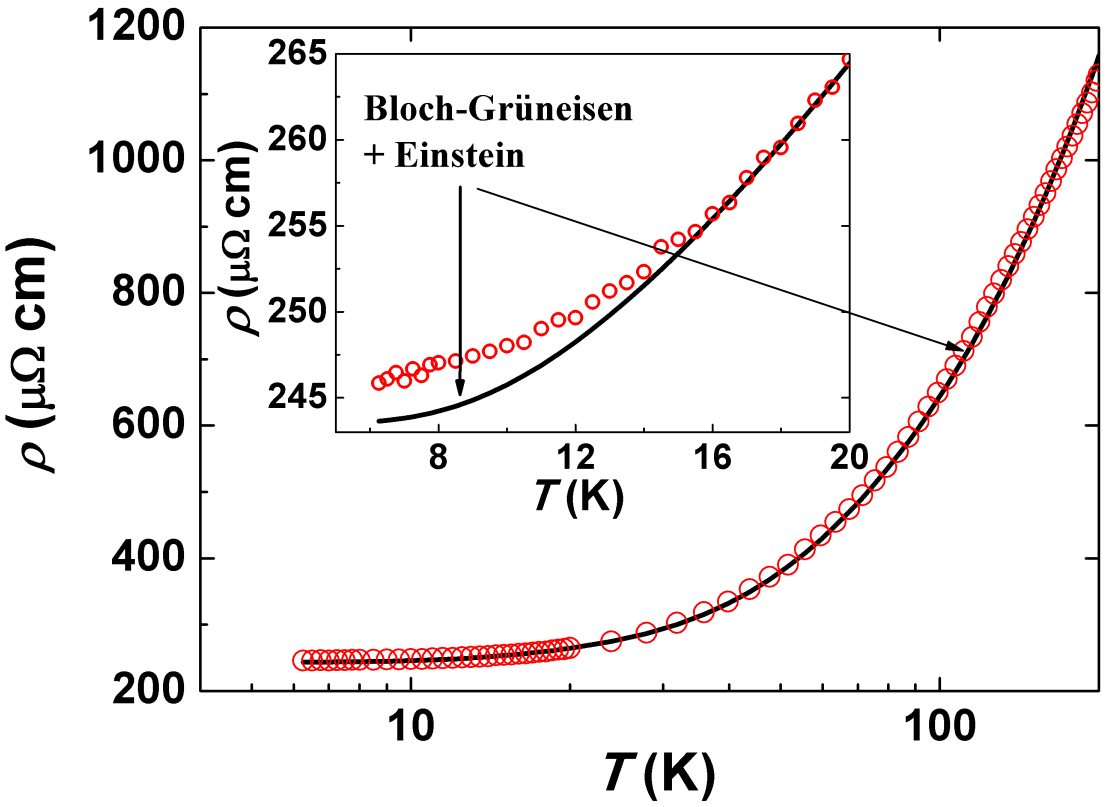

Fig. 16. Type-I $Ba_8Ga_{16}Sn_{30}$ resistivity measurements (open circles) and fitting (solid curve) from Bloch-Grüneisen function and Einstein model with $\Theta_D = 230$ K and $\Theta_{E1} = 56$ K, $\Theta_{E2} = 49$ K. Inset: Expanded view at the low temperature end of the data and fitting. There is a clear mis-match between the model and data.

resistivity is given by,

$$\rho_A(T) = \frac{m^*}{n_0 e^2 \tau(T)}. \tag{5.11}$$

The temperature-dependent electron lifetime ($\tau(T)$) can be obtained by averaging the energy-dependent lifetime,

$$\tau(T) = \int_{\infty}^{\infty} dE \tau(E) \left(-\frac{df(E)}{dE} \right), \tag{5.12}$$

where $f(E) = \frac{1}{\exp\{E/k_B T\}+1}$ is the Fermi function. Furthermore, $\tau(E)$ can be obtained from the imaginary part of the retarded self-energy [39, 33],

$$\tau^{-1}(E) = \pi g^2 N(0) \int_0^{\infty} d\Omega A(\Omega)[2n(\Omega) + f(\hbar\Omega + E) + f(\hbar\Omega - E)] \tag{5.13}$$

where $A(\Omega) = -\frac{1}{\pi} ImD(\Omega) = \frac{1}{\pi} \frac{4\omega_0 \Gamma_0 \Omega}{(\Omega^2 - \omega_r^2)^2 + 4\Gamma_0^2 \Omega^2}$ is assumed to be the phonon spectral function as defined in equation (5.7). The effective localized phonon frequency (ω_0), phonon damping rate (Γ_0) and renormalized phonon frequency (ω_r) are also all defined in this way as for the NMR results [33, 40]. The analysis of the NMR results yielded a large damping coefficient, $\Gamma_0 = 12$ K, which will tend to enhance the corresponding resistivity contribution at low temperatures. Note that a damped 1D anharmonic model was also considered in an analysis of the optical conductivity [38], yielding a damping coefficient $\Gamma \approx 0.5$ THz $= 24$ K at low temperatures, not far from the value we reported. For $k_B T << \hbar\omega_r$, the calculated resistivity will follow a $\rho \sim T^2$ relationship as described above [33]. Thus we examine a combination of the Bloch-Grüneisen function, Einstein model and anharmonic model with respect to the resistivity in the low temperature region.

In fitting the resistivity, we used the model for Θ_D, Θ_{E1}, Θ_{E2}, ρ_0 as above with the addition of the anharmonic contribution with the same damping rate Γ_0 and temperature dependent phonon frequencies (ω_0, ω_r) from the NMR analysis [40].

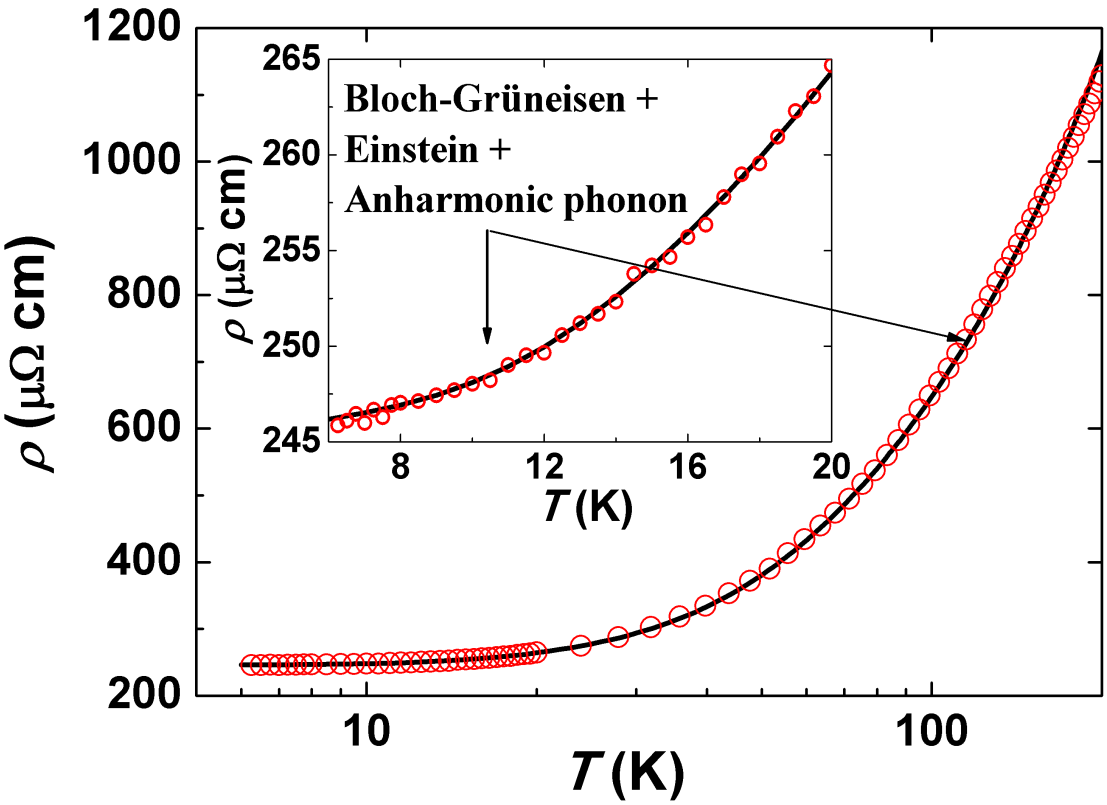

Fig. 17. Type-I $Ba_8Ga_{16}Sn_{30}$ resistivity data (open circles) and fitting (solid curve) with rattler contribution added to the previous model, $\Theta_D = 230$ K, $\Theta_{E1} = 66$ K and $\Theta_{E2} = 54$ K. Inset: Expanded view of the low temperature region. The mis-match between the data and the model has been reduced significantly compared to that of Fig. 16.

Fig. 17 shows the result from this combined model with fitted parameters $\Theta_D = 230$ K, $\Theta_{E1} = 66$ K, $\Theta_{E2} = 54$K, $\rho_0 = 245\ \mu\Omega$ cm. A single additional parameter represents the overall strength of the anharmonic contribution. The high-temperature agreement is not affected by this additional anharmonic term, but the inset of Fig. 17 shows an improved fit in the low temperature region. Note that the anharmonic portion only exhibits a strong contribution at low temperatures. We emphasize that this combined model starts directly from specific physical mechanisms in this system, so the results should be consistent with heat capacity as we examine later.

5. Heat capacity and modeling

Heat capacity were also measured with the PPMS system. Data from 2 K to 200 K are shown in Fig. 18 with a fit including several mechanisms as described below. In fitting the data, the leading contribution was taken as a Debye model for the framework atoms, Ga/Sn,

$$C_D = 9N_D R(\frac{T}{\Theta_D})^3 \int_0^{\Theta_D/T} \frac{x^4 e^x dx}{(e^x - 1)^2}, \tag{5.14}$$

where Θ_D is the Debye temperature, and N_D is fixed at 46, the number of framework atoms per cell.

In a similar way as for the resistivity, the six Ba(2) atoms were considered to be rattlers with both anharmonic and harmonic motions corresponding to the different directions. We started from the assumption that the anharmonicity will only be active in one direction, so the simulation starts with six 1D anharmonic oscillators and six 2D Einstein oscillators for these atoms. We use Θ_{E2} as their Einstein temperature, N_{E2} as the 2D Einstein oscillator number and N_{Anh} as the 1D anharmonic oscillator number. Two Ba(1) atoms, inside the smaller cages, were treated by a 3D Einstein

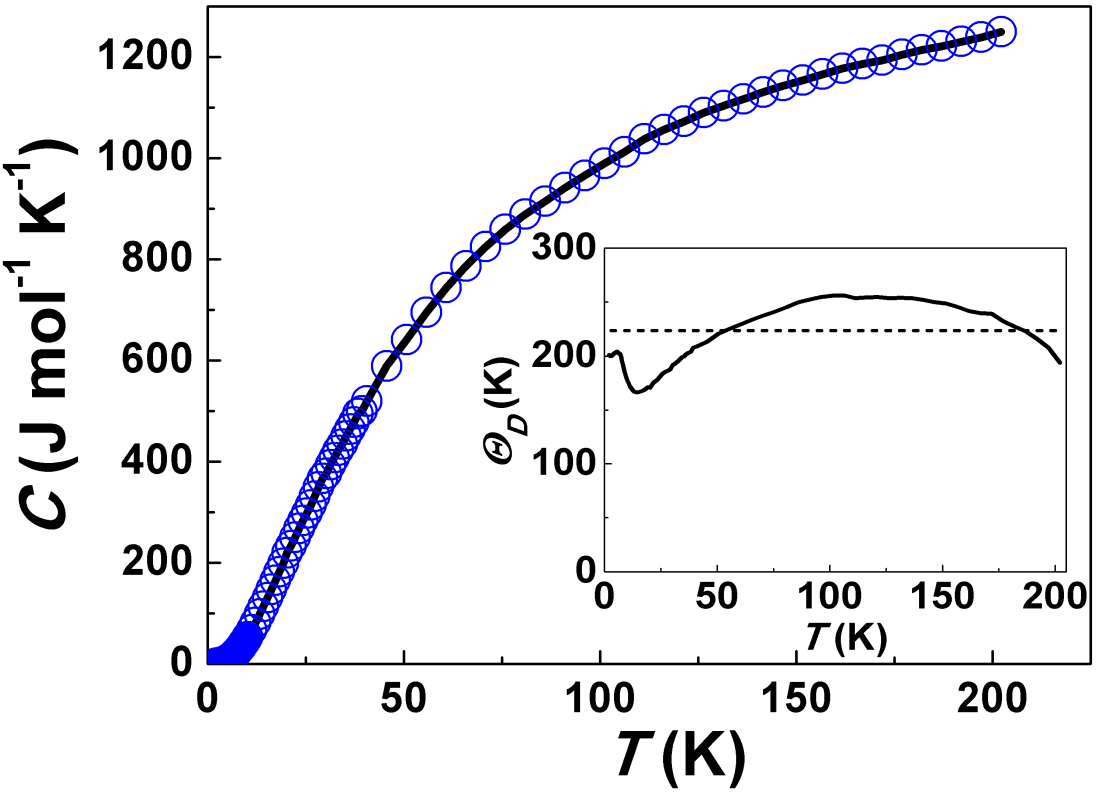

Fig. 18. Type-I $Ba_8Ga_{16}Sn_{30}$ heat capacity measurement (open circles) and fitting (solid curve) to the model described in text. Inset: Temperature dependent $\Theta_D(T)$. For comparison, the Debye temperature from resistivity fit is represented here by the dotted line.

model with parameters Θ_{E1} and N_{E1}. They follow the standard Einstein behavior,

$$C_E = 3N_E R \left(\frac{\Theta_E}{T}\right)^2 \frac{e^{\Theta_E/T}}{(e^{\Theta_E/T}-1)^2}. \tag{5.15}$$

For the anharmonic contribution, we used

$$U = \frac{\sum_{n=0}^{\infty} E_n \exp\{-E_n/k_B T\}}{\sum_{n=0}^{\infty} \exp\{-E_n/k_B T\}},\ C_A = \frac{dU}{dT}, \tag{5.16}$$

where the energy levels E_n, shown in Fig. 12, are those corresponding to the anharmonic potential from the NMR results [40]. The lowest 13 levels were used, after we verified that higher levels only added a sufficiently small contribution to the sum to be ignored.

The fitting result shown in Fig. 18 gives $N_{E1} = 2$, $\Theta_{E1} = 70$ K, $N_{E2}= 6$, $\Theta_{E2} = 55$ K, $N_{Anh} = 5.4$. Also, we used a temperature dependent Debye temperature $\Theta_D(T)$ for the fitting, resulting in a typical behavior as shown in the inset of Fig. 18, with values near 230 K, consistent with the resistivity result. See the comparison in Table. I. The electronic contribution, γT, is given by $\gamma = 1.85$ mJ/mol K^2 per atom. Note that a reduced number of anharmonic oscillators is obtained ($N_{anh} = 5.4$) with about 10% missing, relative to the expected 6 per cell. To account for the missing oscillator strength and the observed low temperature tail in C, we added a low energy 1D Einstein term with $N_{E3} = 0.6$, $\Theta_{E3} = 14.2$ K. The C/T^3 vs. T plot in Fig. 19 shows the contribution of each term. The Einstein curve in the figure is a superposition of the three Einstein terms. With the exception of the small Θ_{E3} term, the fitted results are in good agreement with those obtained from resistivity. Notice that the Θ_{E3} term only contributes significantly below 5 K, so it will not introduce noticeable influence on the resistivity fit. The broad peak in C/T^3 at low temperatures agrees well with the anharmonic parameters taken directly from the NMR fit, and the result serves

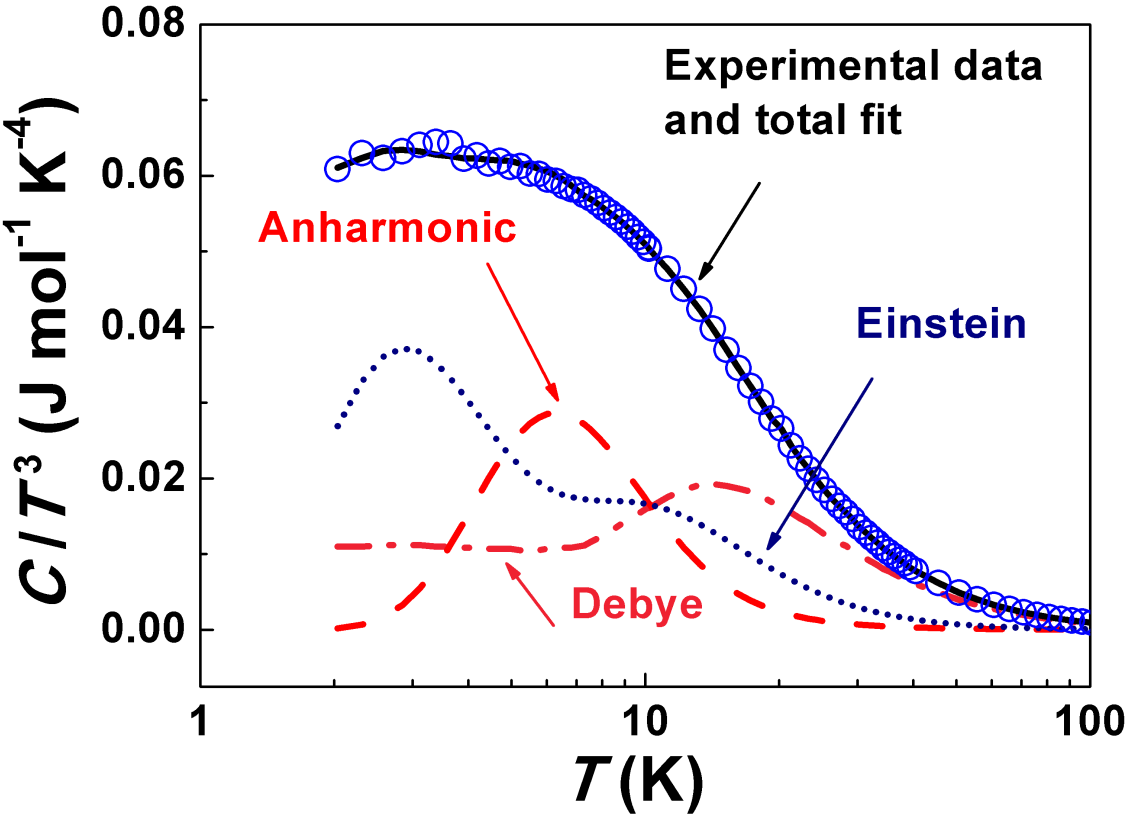

Fig. 19. Measured C/T^3 vs. T for type-I $Ba_8Ga_{16}Sn_{30}$ and the fit to models described in text (solid curve). Individual contributions as labeled: Debye (dash-dotted), Einstein (dotted) and anharmonic oscillator (dashed). The Einstein part is a superposition of several oscillators.

to quantify the corresponding number of anharmonic oscillators. The model dividing the oscillator strength into localized and extended parts thus provides a consistent explanation for these results.

6. Discussion

Often for modeling of the heat capacity in clathrate systems, a multi-Einstein model is used to describe the broad distribution representing the low temperature peak in C/T^3 vs. T plot. This works reasonably well for $Ba_8Ga_{16}Ge_{30}$, $Sr_8Ga_{16}Ge_{30}$

Table I. Comparison of fitted parameters from resistivity and heat capacity analysis.

	Θ_{E1} (K)	Θ_{E2} (K)	Θ_{E3} (K)	Θ_D (K)
Resistivity	66	54	–	230
Heat capacity	70	55	14.2	[170-260]

among others [22, 35]. However, $Ba_8Ga_{16}Sn_{30}$ exhibits a broad peak, and correspondingly the large cage-center position is marginally stable [23] or perhaps unstable to off-center ion displacements [38], which suggests an anharmonic rattling model as has been applied here. Our analysis shows that a specific local potential of this type can be connected to several experimental results in a consistent way, thus providing a good physical picture for the vibrational behavior. The large damping coefficient indicated by the resistivity as well as the NMR results implies that these modes are strongly coupled to other excitations, and thus cannot be regarded as completely independent oscillators. Recent research on phonon dispersion in clathrates, including $X_8Ga_8Si_{128}$, $A_8Ga_{16}Si_{128}$ and $Rb_2Sr_6Ga_{14}Ge_{32}$, have shown strong interactions between localized rattler modes and the framework atoms [43, 37, 69, 70, 71, 72, 73, 74, 75, 76, 77], which may offer other explanations for this phenomenon.

Our fitting works surprisingly well based on the initial assumption that the anharmonic motion is one dimensional, giving six 1D anharmonic oscillators. This differs from the expected two dimensional behavior, often described as a four-well potential due to the configuration of the Ba(2) cages [41]. However recent studies point to an off-center symmetry for Ba(2) oscillations [23], and previous *ab-initio* results from our group [54] indicate a static off-center displacement of about 0.5 Å for Ba on this site based on Ga-Sn alloy disorder. With sufficient cage distortion, rattling-type vibrations near the cage minimum could be constrained to be effectively one-dimensional,

with a harmonic restoring potential in other directions. An alternative view might be that among the two-dimensional anharmonic oscillators, approximately half of the rattlers are not activated, accounting for the corresponding missing spectral weight from the heat capacity fit. The presence of stronger defects, such as vacancies, possibly leads to this situation in some of the cages.

However, we also note that a fit of our heat capacity data using a 2-D rotationally symmetric anharmonic potential as was also fitted to the NMR relaxation results [40], did not work as well as the 1-D assumption. The heat capacity peak was pushed to higher temperatures away from the center of the experimental C/T^3 peak, as shown in Fig. 20, and this requires a much bigger Einstein contribution at lower temperatures and Einstein temperatures significantly different from the resistivity results. In this fit, the 2-D well parameters are those taken from the NMR fit described previously and the fitted Einstein temperatures are $\Theta_{E1} = 50$ K, $\Theta_{E2} = 36$ K and $\Theta_{E1} = 15$ K. Comparing to the 1-D results in Fig. 19, it is clear that a series of widely-distributed harmonic oscillators must contribute much more weight in this 2-D model, which is similar to the soft-potential model that I will discuss below. Note that the 2-D model is a simplified potential with high symmetry. A four-well 2-D potential may have additional splitting which could lead to better modeling of the heat capacity. This could still be interesting for future study, and might offer an improved understanding of the actual motion mechanism for this anharmonic system.

We should remark that both the WDS and XRD results show a small reduction of the Ba atom content relative to the stoichiometric composition. However this amount is much too small to account for any significant discrepancy in the number of rattler atoms as obtained in our heat capacity fit. According to WDS measurements at several places in the ingot [54] the Ba content is reduced by about 2%. According to the measured small Ga excess, this sample would be expected to be p-type [35]. Such

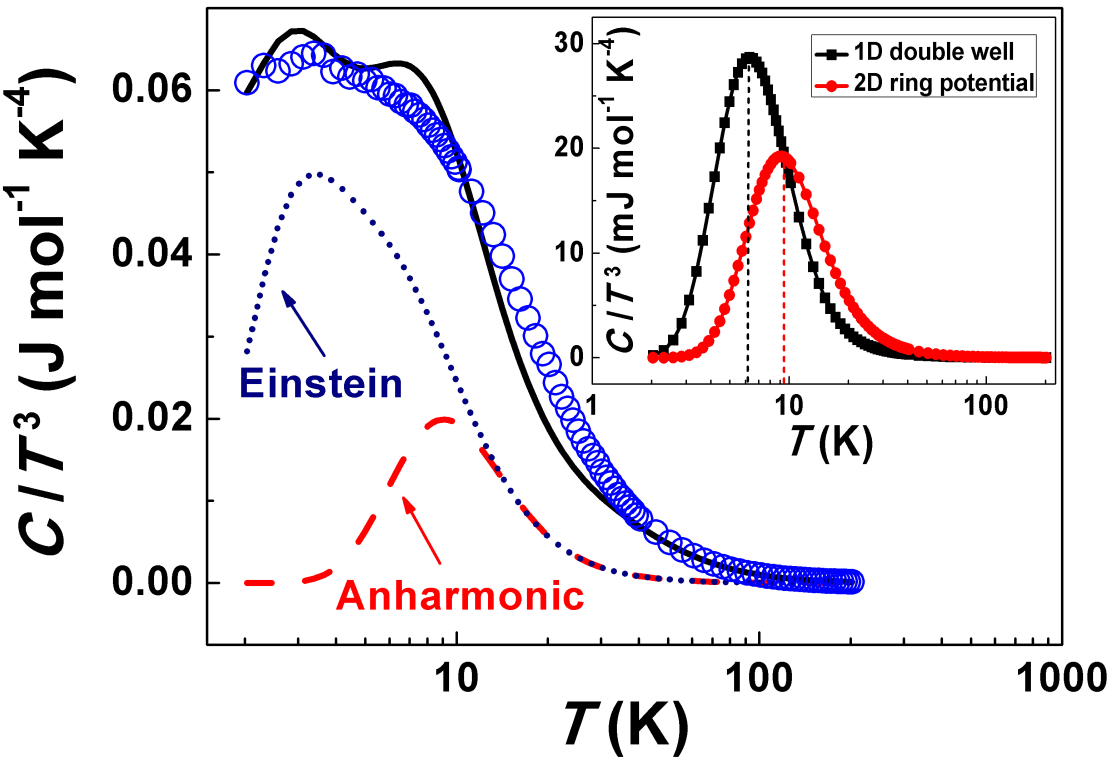

Fig. 20. A fit to the heat capacity of the type-I $Ba_8Ga_{16}Sn_{30}$ with the simplified 2-D ring potential, including the total fit (solid curve), the anharmonic contribution (dashed curve) and the total Einstein term (dotted curve). Inset: comparison of the anharmonic contribution between the 1-D (solid squares) and 2-D (solid circles) assumptions.

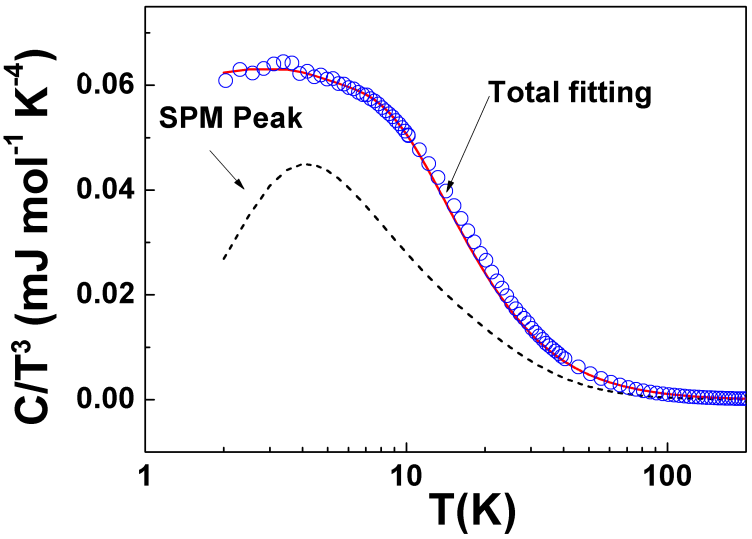

Fig. 21. A fit to the heat capacity of the type-I $Ba_8Ga_{16}Sn_{30}$ using SPM model for the anharmonic contribution. The total fit is the solid line and the SPM contribution is the dashed line.

a composition also would not be expected to exhibit a large number of spontaneous vacancies, as they are not needed to maintain the Zintl electron count.

Another well known approximation, the soft potential model (SPM), has been introduced into the analysis of the heat capacity in many systems with anharmonic contributions and has shown good agreement with experimental results [78, 34, 35, 79]. This model is based on a soft vibrational density of states and the tunneling of an assumed wide distribution of two level systems. A significant contribution from two level tunneling systems was deduced in $Ba_8Ga_{16}Sn_{30}$ and $Sr_8Ga_{16}Ge_{30}$ at low temperatures [34, 35]. A very broad distribution of oscillation frequencies is considered in this model, which can simulate both the anharmonic contribution and harmonic contributions. Indeed, the small added Einstein term at low temperatures in the heat capacity fit may represent a distribution of tunneling sites of this type.

It is not clear what may be the origin of these additional tunneling systems, however their number is relatively low.

I also tried using the SPM model to fit the heat capacity data, as a simple comparison, and obtained a similar overall fit, as shown in Fig. 21. The results appear to be as good as that shown in Fig. 18. The values of the two Einstein terms Θ_1 and Θ_2 are about the same as in the previous fit, however small changes were made to the temperature dependent Debye term. It is clear that the SPM peak is much broader than the anharmonic contribution shown in Fig. 19, and it can be considered to express the contribution of a broad distribution of oscillation frequencies, including the anharmonic term and some other low energy local oscillators for this case. However the anharmonic potential introduced above has the advantage that it fits the NMR and resistivity as well as the heat capacity data, and thus provides a more specific physical basis for the observations than the SPM model. Thus, while the SPM model alone does work reasonably well in analyzing the heat capacity, the results shown here point to a strongly damped anharmonic potential as a more physical model for this system.

The sensitivity of the overall fit to the fitting parameters is also important to discuss. For the heat capacity, the fitted oscillator numbers are important, because they not only determine the overall shape of the fit, but also offer a physical picture of the localized motions. For the anharmonic contribution, a variation in the anharmonicity affects the energy levels, changing the position as well as magnitude of the anharmonic contribution to the C/T^3 plot. In the original fit I used anharmonic well parameters taken directly from the reported NMR results, however Fig. 22 shows results for which the anharmonic potential well width was scaled by $\pm 10\%$, without changing its shape. This corresponds to a scaling of the energy levels by $\pm 20\%$. For these curves, the Debye and Einstein temperatures were not changed, however the

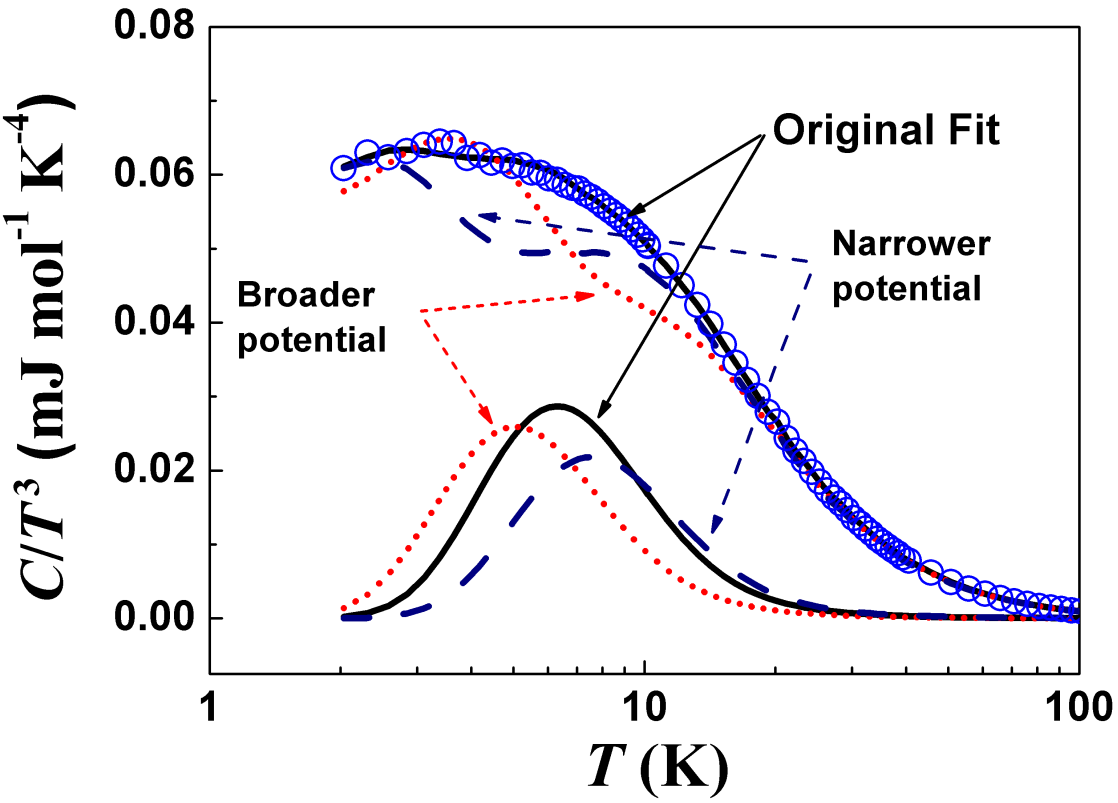

Fig. 22. Comparison of the anharmonic contribution and the total calculated heat capacities from different anharmonic potentials of the type-I $Ba_8Ga_{16}Sn_{30}$. Solid lines: results from previous NMR calculation. Dotted lines: energy levels compressed by 20%, which corresponds to higher anharmonicity. Dashed lines: energy levels extended by 20%, which corresponds to lower anharmonicity.

oscillator numbers were allowed to adjust, with a result that the numbers no longer match the composition, and the agreement with the measured curve is clearly made worse. This indicates the sensitivity of the fit to the anharmonic potential. It is possible to obtain an improved agreement with such a scaled potential by allowing the Einstein temperatures to change, however this occurs by shifting the lowest Θ_E values on top of the anharmonic peak, a result that is similar to the SPM model discussed above, in which a distribution of harmonic oscillators approximates the distribution of energy levels.

B. Type-VIII $Ba_8Ga_{16}Sn_{30}$

Type-VIII $Ba_8Ga_{16}Sn_{30}$ has a different cage structure compared to the type-I crystal structure. The guest atom free space and off-center displacement are much smaller than the larger type-I cage, which indicates less possibility to have strong anharmonic guest atom vibration.

1. Sample preparation

The sample preparation process was the same as type-I, and performed by Dr. Sergio Rodriguez. The pure elements were mixed together at the nominal composition followed by an initial arc melting in an argon environment. The samples were annealed in an evacuated quartz tube at 900 ^oC for 50 hours, followed by a controlled slow cooling to 500 ^oC in 80 hours. Then, XRD and WDS measurements were performed. Assuming the framework sites are completely full, the WDS results give a composition of $Ba_{7.66}Ga_{16.28}Sn_{29.72}$ for this type-VIII sample. If we assume that the framework occupation is given by the Ga and Sn atom occupations from Rietveld refinements, the composition is: $Ba_{7.37}Ga_{15.69}Sn_{28.63}$. X-ray and WDS result are in good agreement

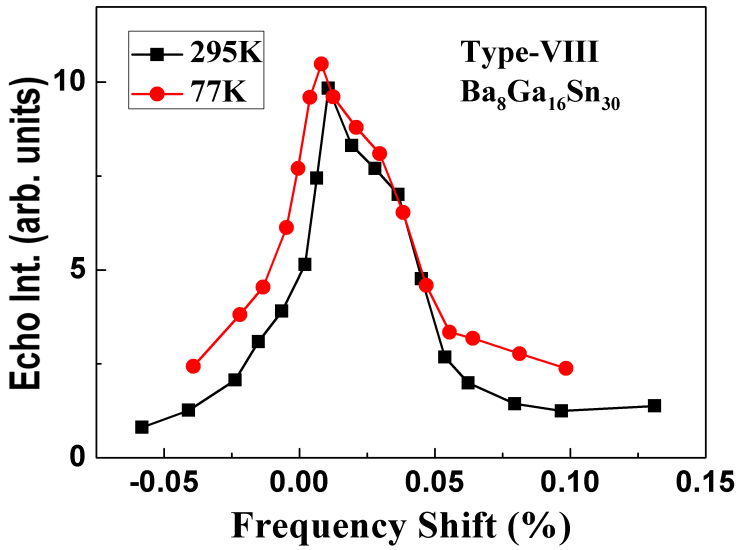

Fig. 23. ^{71}Ga lineshape of type-VIII $Ba_8Ga_{16}Sn_{30}$ clathrate at 295K (solid squares) and 77K (solid circles) after temperature renormalization.

[54].

2. NMR results and discussion

NMR experiments were carried out under an external magnetic field of 8.8 T in a temperature range from 4.2 K to 295 K using the same pulse spectrometer and probe as the type-I samples. The nuclei measured are ^{71}Ga and ^{69}Ga. Fig. 23 shows the ^{71}Ga NMR lineshape comparison between 295K and 77K. There is no significant change in the spectra shape, but line broadening and a center of mass shift can be observed vs. temperature. The result from ^{69}Ga gives a similar behavior (not shown). The frequency shift is very small for this sample. The center of mass value is only about 0.02%.

Magic angle spinning (MAS) NMR was also performed on this sample under an external field of 9.5 T. Two spinning rates of 10 kHz and 13kHz have been used. The

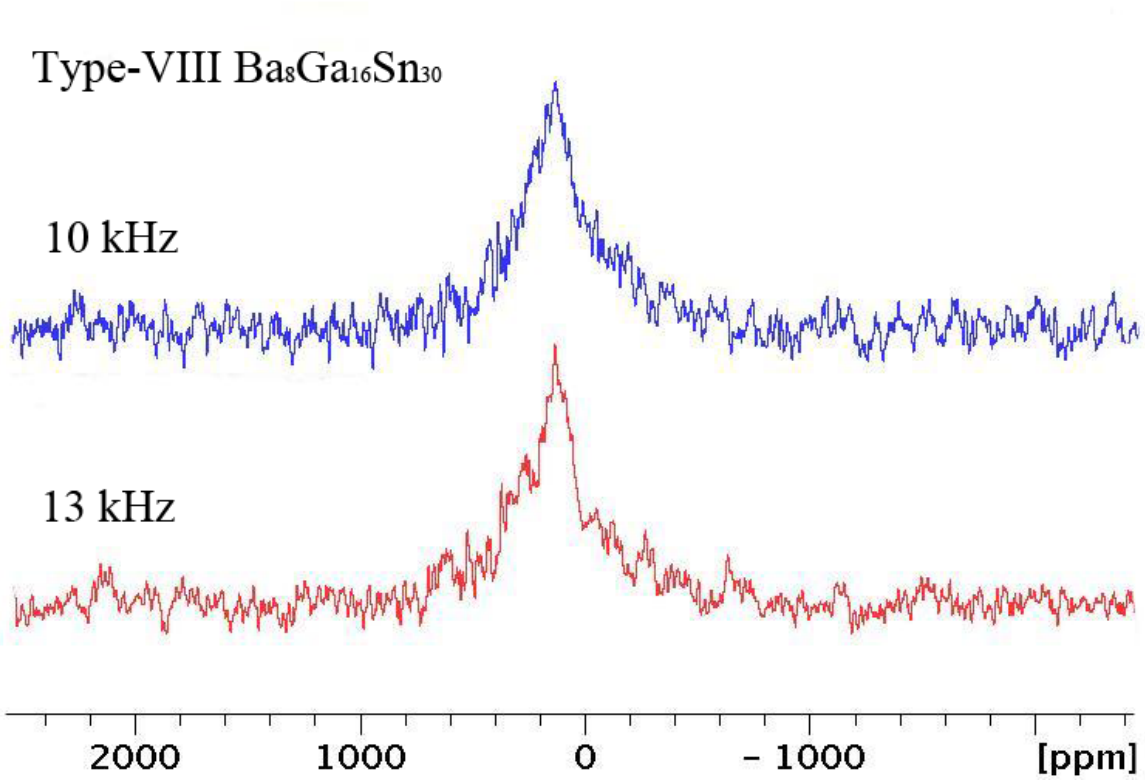

Fig. 24. The MAS NMR spectrum with rotating speeds of 10 kHz (upper) and 13 kHz (lower) for ^{71}Ga. No significant linewidth narrowing is observed.

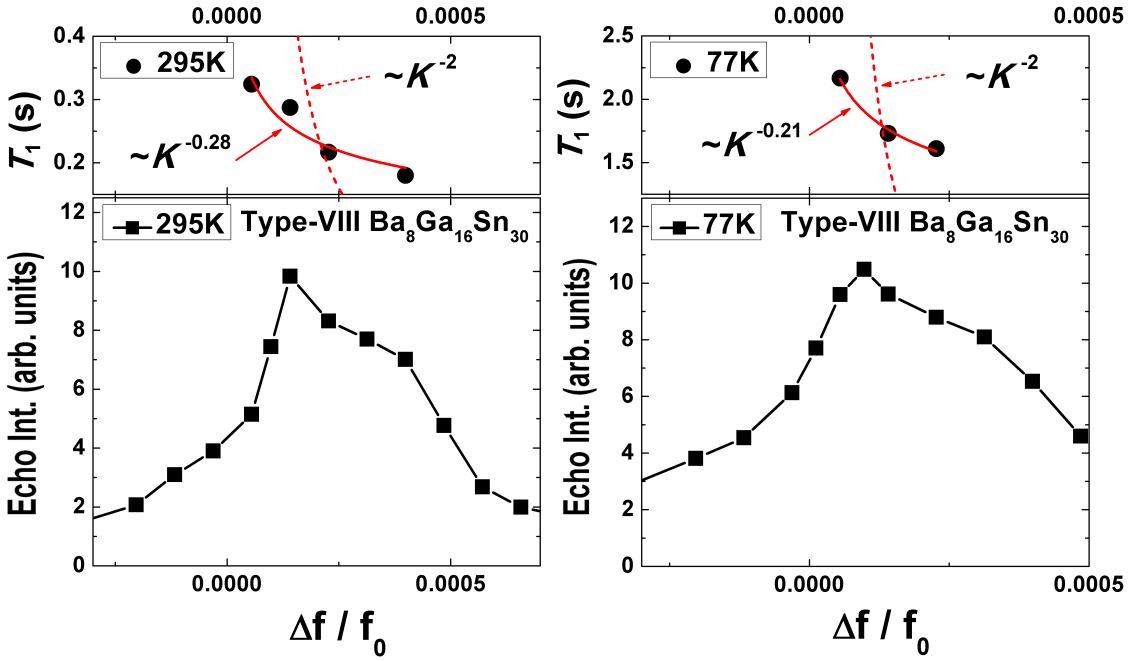

Fig. 25. ^{71}Ga T_1 of type-VIII $Ba_8Ga_{16}Sn_{30}$ vs. frequency at 295 K (left) and 77 K (right) plotted in comparison to the measured lineshapes. Also shown: T_1 fits to a function $A \cdot K^B$ (solid curves), assuming $K = \Delta f / f_0$. For comparison, a Korringa K^{-2} behavior is also shown (dashed curves).

MAS results are shown in Fig. 24, where no significant narrowing has been observed for this sample and the results are similar to the static result. Also, the spinning side-bands, with about 100 ppm separations, are not clearly shown in the MAS results, indicating possible overlappings of the side-bands from mutilple sites. In this case, the overall lineshape is more likely to be a superposition of of multiple peaks due to the local environment, which do not have large temperature dependences.

The spin-lattice relaxation time (T_1) was measured at 295 K and 77 K for different frequencies along the lineshape, as shown in Fig. 25. The decrease in T_1 with increasing frequency shift agrees with the basic trend of the Korringa law, which may indicate that a distribution of metallic shifts is partially responsible for the broadening. A similar result was observed for ^{71}Ga NMR in $Sr_8Ga_{16}Ge_{30}$ and ^{27}Al NMR in

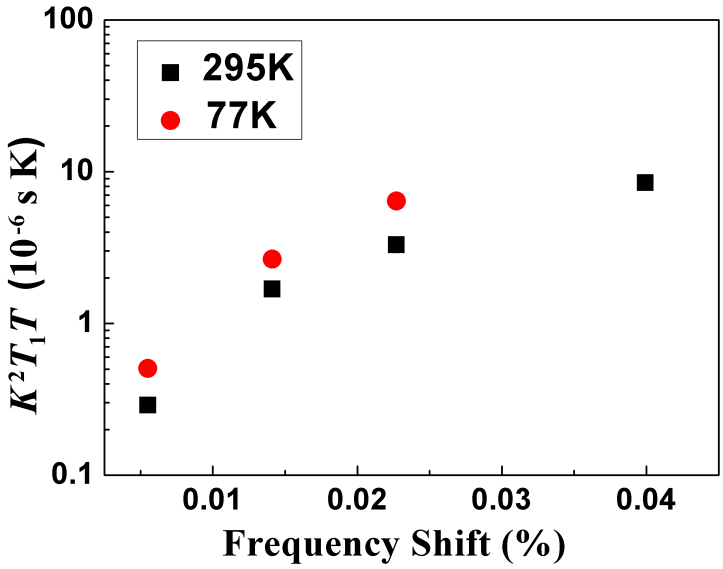

Fig. 26. The values of K^2T_1T in 77 K (solid circles) and 295 K (solid squares) for ^{71}Ga of type-VIII $Ba_8Ga_{16}Sn_{30}$ are plotted for different frequencies and compared, assuming $K = \Delta f/f_0$.

$Ba_8Ge_{30}Al_{16}$ [52]. However, if we fit the T_1 values to a function $T_1 = A \cdot K^B$, where $K = \Delta f/f_0$ is the frequency shift, we get $B \cong -0.21$ for 77 K and $B \cong -0.28$ for 295 K. These clearly do not follow a Korringa behavior, $K^2T_1T = \text{const}$. For comparison, the corresponding K^2T_1T values at given frequencies, the same as in Fig. 25, are calculated and shown in Fig. 26. So it is apparent that the metallic shift is not the only contribution here.

The spin-lattice relaxation time (T_1) was measured vs. temperature from 4.2 K to 295 K for both ^{69}Ga and ^{71}Ga, as was also measured for the type-I sample. Note that T_1 here is frequency-dependent, so a small frequency shift vs. temperature would bring some additional uncertainty to the measured T_1 values. All measurements were performed at frequencies corresponding to the maximum Echo intensity in order to reduce the influence from the frequency-dependence. The relation,

$\Delta f/f_0 = K + BQ^2/H$, where the second term is the quadrupole contribution, was used to calculate the corrected magnetic shift (K), which also may contain some chemical shift contribution. The peak frequencies from ^{71}Ga and ^{69}Ga were used: $^{71}(\Delta f/f_0) = 0.015\%$ and $^{69}(\Delta f/f_0) = 0.0084\%$ at room temperature. As there is no significant change of the peak position vs. T, the calculated value $K \cong 0.019\%$ was used for the magnetic shift associated with the measured T_1. The corrected K^2T_1T value at 295 K and 77 K are now 3.1×10^{-6} s·K and 4.8×10^{-6} s·K, which are closer to the theoretically expected value of 2.7×10^{-6} s·K for ^{71}Ga.

The quadrupolar and magnetic contributions to the total relaxation rate were calculated and plotted in Fig. 27 using equations (5.1) and (5.2). It is clear that the relaxation rates behave differently compared to those of type-I, although the rapid increase of T_{1Q} in the very low temperature region still indicates the possible existence of localized oscillators. This behavior could be the upper edge of an anharmonic peak of the same type as observed for type-I $Ba_8Ga_{16}Sn_{30}$, assuming that the lower edge of the relaxation peak falls below the measurement range. However, this would imply a less confining potential for the rattler, which is not consistent with the smaller observed cages in type-VIII. Nevertheless, since the upturn appears in the quadrupole channel, it implies a vibrational feature of some type that slows down at these temperatures. The physical origin of this feature remains unclear.

By investigating the isotopic ratio of the overall relaxation rate, we also found that in contrast to type-I $Ba_8Ga_{16}Sn_{30}$, the entire system is not simply dominated by the quadrupolar mechanism, but has contributions from the magnetic term, as shown in Fig. 28. The leading contribution changes from quadrupolar to magnetic as the temperature increases.

There are other mechanisms that can offer explanations for the NMR relaxation behavior. One choice would be a two-level disorder model, as has been used to describe

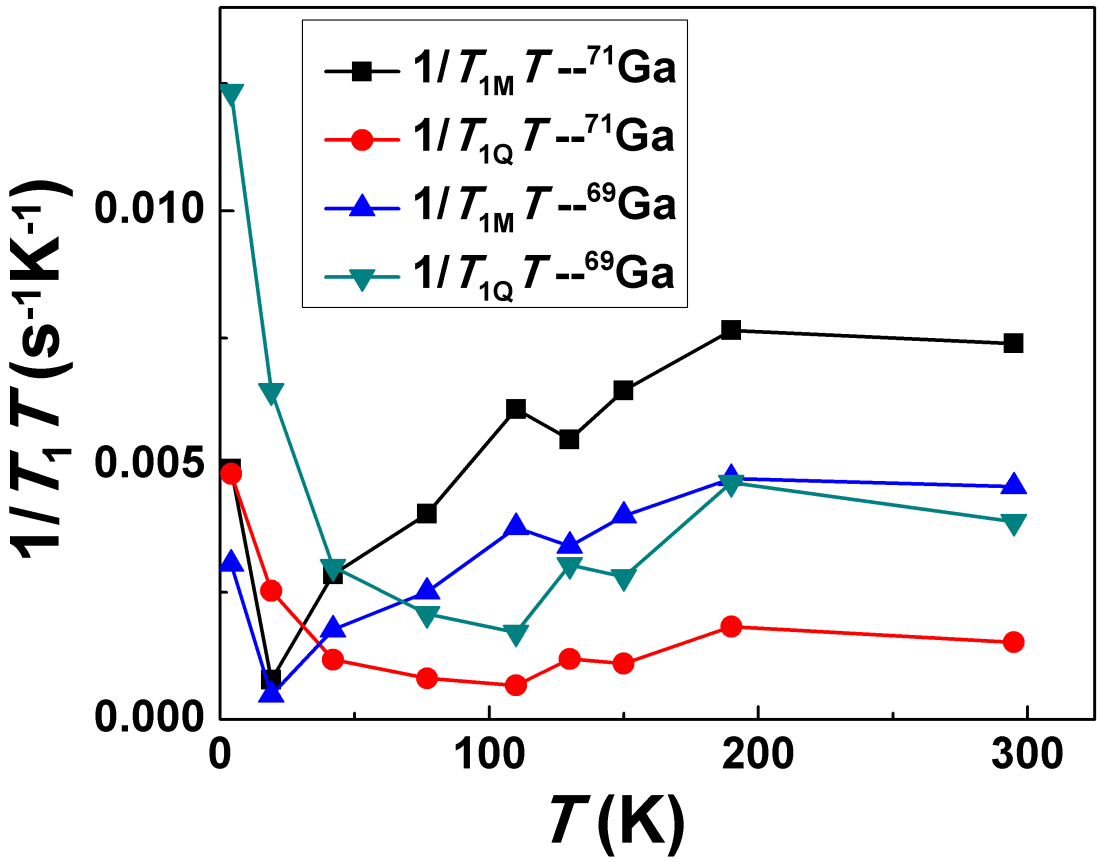

Fig. 27. Separated T_1 relaxation rates for ^{71}Ga and ^{69}Ga of type-VIII $Ba_8Ga_{16}Sn_{30}$: ^{69}Ga-quadrupole (diamonds, as labeled), ^{71}Ga-quadrupole (circles, as labeled), ^{71}Ga-magnetic (squares), ^{69}Ga-magnetic (triangles).

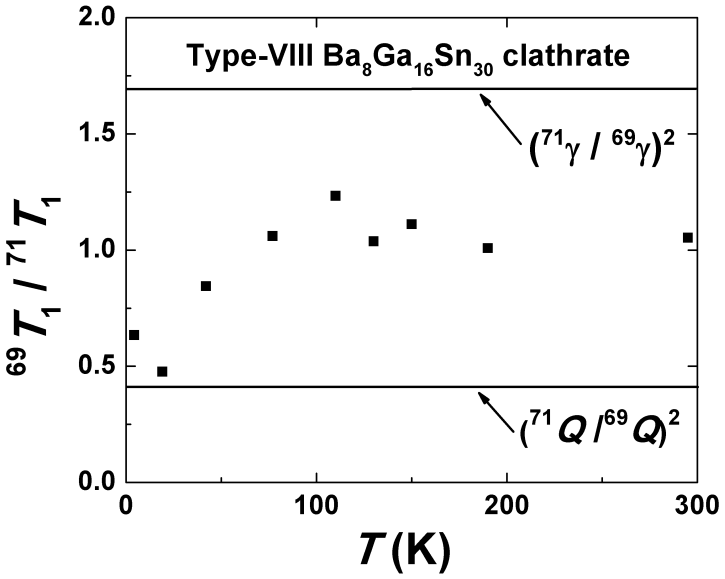

Fig. 28. Isotopic ratio of overall spin-lattice relaxation rates under 8.8 T, with limits for pure quadrupolar/magnetic relaxation indicated.

the spin-lattice relaxation behavior in glass-like materials [80, 81, 82]. This model contains a set of two-level modes with a continuous distribution of energy splittings and an appreciable potential barrier between the two levels, as shown in the inset of Fig. 29. These modes are thought to arise from the motion of groups of atoms which can occupy two configurations of nearly equal energy [83, 84]. A process only involving the excitation and deexcitation of such a disordered set of modes, interacting with the nuclear spin, contributes to T_1^{-1}, as given in the lowest order perturbation theory, according to

$$\frac{1}{T_1} = \frac{4\pi}{\hbar^2}\int_0^{E_m} Q_m^2 |V_{i,j}|^2 \rho_D^2(E) \left[1 + \cosh\left(\frac{E}{k_B T}\right)\right]^{-1} dE, \tag{5.17}$$

where ρ_D is the energy density of the modes, E is their energy splitting (see inset of of Fig. 29) and E_m is the maximum energy of the splitting. In glasses, it is found that the

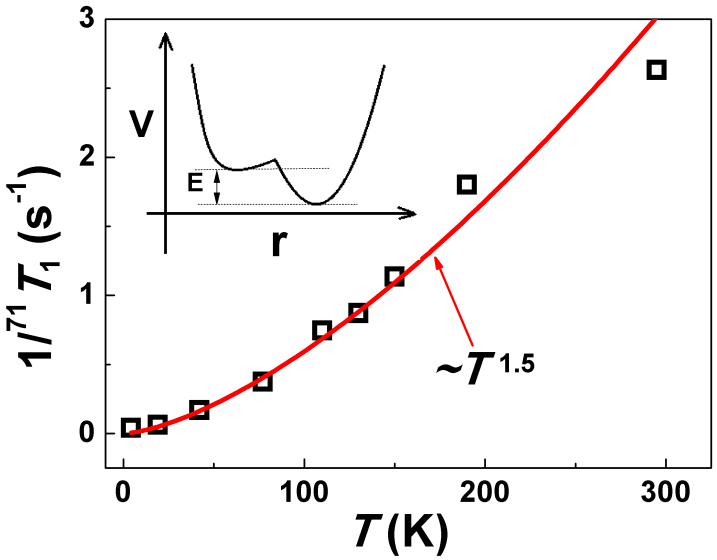

Fig. 29. $1/T_1$ for ^{71}Ga (open squares) of type-VIII $Ba_8Ga_{16}Sn_{30}$ and a fit (solid curve) from the tunnel-disorder model. Inset: sketch of a characteristic potential energy in this model. E is the excitation energy splitting.

density of tunneling modes varies as $\rho_D(E) = \rho_0 E^\eta$, where E is the energy splitting, η is positive and less than unity to give a weak variation [80]. Also the coupling to the nuclear spins is considered to be independent of E. At low temperatures ($K_B T \ll E_m$), the relation resulting from equation (5.17) is

$$T_1^{-1} \propto T^\alpha, \alpha = 1 + 2\eta. \tag{5.18}$$

This model works very well in many amorphous materials, such as B_2O_3, As_2S_3, As_2Se_3 and borosilicate glass [82, 85]. We found that our NMR results also follow such a T-dependent variation quite well below 150 K, as shown in Fig. 29. The fitted value for α is about 0.5, which is similar to what was reported for the amorphous materials described above. Thus, tunneling modes in a disordered potential could be a possible explanation for the observed NMR relaxation behavior. Although type-

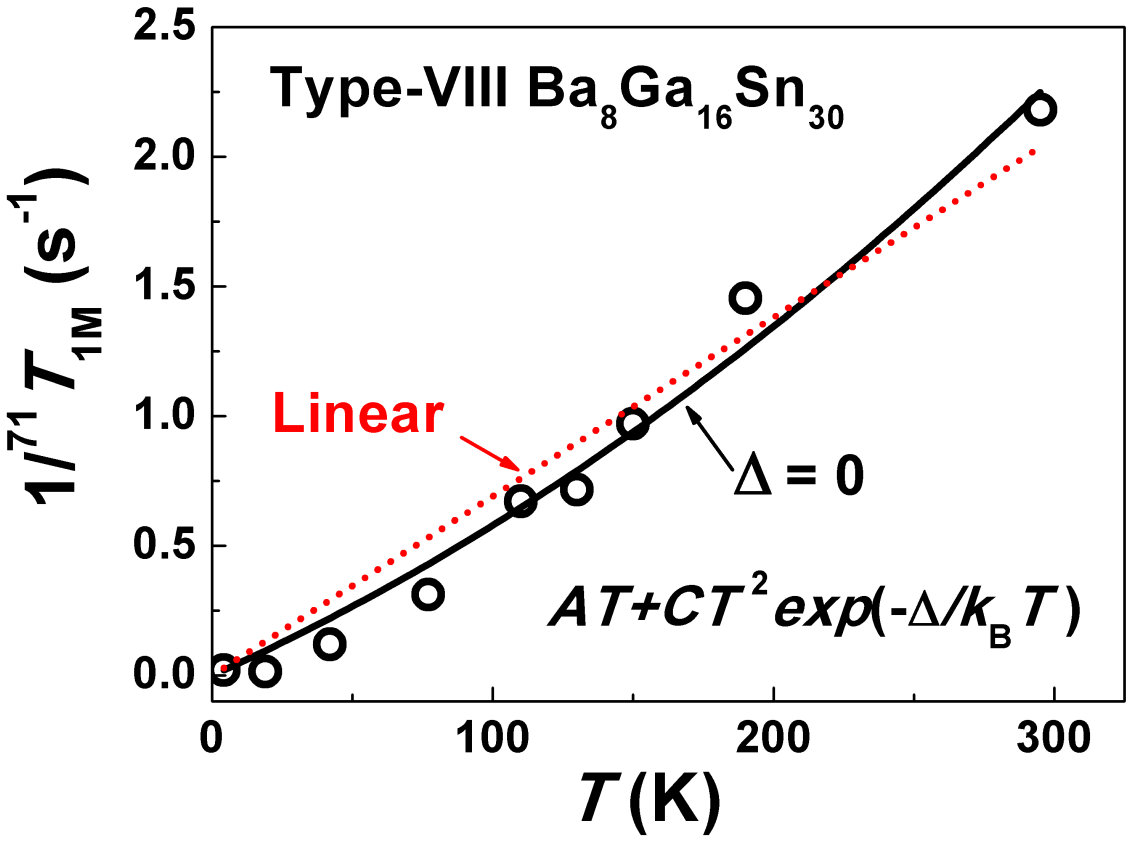

Fig. 30. $1/T_1$ of ^{71}Ga (open circles) and a few fits from the semiconducting two-band model. For the fit from 4 K to 300 K, there are two stable fits with $\Delta \cong 0$ (solid curve) and $\Delta \cong +\infty$ (dotted line).

VIII $Ba_8Ga_{16}Sn_{30}$ is not an amorphous material, its thermoelectric properties have shown glass-like behavior [23], so it is not a big surprise to see that other features of amorphous materials can also be observed. Also, note that this material is a Zintl phase and thus it is possible that the tunneling system is due to the vacancies associated with this sample. From the XRD results, the vacancy number is small, which is less than one per unit cell. This offers a possible fit to the relaxation data. But notice that the atomic motion normally couples more strongly to the quadrupole channel, which has to be addressed as a drawback of this model. So this could not give a clear physical explaination to the NMR relaxation behavior.

An alternative option is a model in which the change in $1/T_{1M}$ is due to excitation of carriers across a gap, called as semiconducting model in this work. For a simple case, assume a two-band model, with one band overlapping the Fermi level while the other is separated from the Fermi level by an energy gap Δ. In this situation, the magnetic NMR spin-lattice relaxation rate is given by,

$$\frac{1}{T_1T} = \frac{1}{T_{1K}T} + CTe^{-\Delta/k_BT} \tag{5.19}$$

where $1/T_{1K}T$ is the Korringa portion of the relaxation rate and the second term represents the effect from the band edge separated from the Fermi surface [86, 87]. The band structure is described by a standard semiconducting situation, where $g(E) \sim \sqrt{E}$. Here, as we do not have a pre-determined Korringa term ($1/T_{1K}T$), which could come from low-T constant T_1T values in the experimental data, its value is set to be a parameter. The fitted results with respect to different temperature ranges are shown in Fig. 30. For the data fitted from 4 K to 300 K, there are two stable fits with $\Delta \cong 0$ and $\Delta \cong +\infty$. The fit with $\Delta \cong 0$ indicates no gap or a cusp at the Fermi level. A huge uncertainty in Δ is also associated with the fit. For the $\Delta \cong \infty$ case, only the linear term shows its contribution, which should be a sign of

metallic behavior. But note that none of these fits is good for the entire temperature range, which makes them less plausible. Compared with previous tunneling studies on type-VIII $Ba_8Ga_{16}Sn_{30}$ [88], where two gaps were reported, with the minimum energy gap calculated being about 40 meV, no clear gap is observed from this fit. This may indicate that either the gap is too small or there is no real gap. Note that, as the random occupation of the atoms makes the theoretical calculation of such electronic structures difficult, NMR measurements can offer other resonable and practical approaches. As the magnetic T_1 is dominated by the electron contribution, it seems most likely that this model together with a modified $g(E)$, which indicates some features near the Fermi surface, can lead to a good explanation for these results.

3. Summary

For type-VIII $Ba_8Ga_{16}Sn_{30}$, the NMR lineshape can be considered as a superposition of contributions from multiple sites. The line width broadening is only partially controlled by the metallic broadening. Its quadrupole spin-lattice relaxation rate, $1/T_{1Q}T$ also has an upturn at low temperatures, which is possibly caused by anharmonic motion, but no clear anharmonic peak is observed here as was seen for the type-I sample. An amorphous model and a semiconducting-gap model were used to analyze the T_1 results. The semiconducting model might seemed more likely to represent the physical situation as the K^2T_1T value is close to the free electron calculation, which indicates that the conduction electron mechanism dominates. A modified energy gap density of states seems likely to further improve the fit.

C. Other related clathrate materials

In analyzing the type-I $Ba_8Ga_{16}Sn_{30}$ clathrate, we were able to characterize its interesting rattling behavior according to a very specific model for its anharmonic motion. We also examined whether similar rattling behavior may exist in other clathrate materials, affecting the NMR and other properties. Studies of n-type $Ba_8Ga_{16}Ge_{30}$ and type-I $Ba_8In_{16}Ge_{30}$ are reported here for comparison. Although the results did not show a strong anharmonic influence as was found in type-I $Ba_8Ga_{16}Sn_{30}$ as expected, other interesting behavior will be described and analyzed, leading to a better understanding of these materials. The Ba-Cu-Ge clathrates are also of interest since our previous structural studies of $Ba_8Cu_xGe_{46-x}$ indicate that x=5.3 may be a semiconductor, and a Zintl phase composition [89].

1. $Ba_8Ga_{16}Ge_{30}$

a. Previous work

$Ba_8Ga_{16}Ge_{30}$ clathrate has been studied by a previous group member, Dr. Weiping Gou [52]. In his spin-lattice relaxation (T_1) measurements, he found that this system does not follow a Korringa relation. Also, the Knight shift and linewidth change with temperature. Those results were explained by carrier freezout, and the development of a dilute set of magnetic moments due to these localized carriers. Several samples were used in his study. One made with a Ga flux method is p-type, while others made from the elements with a stoichiometric starting ratio are n-type. One of the n-type samples was prepared by the G. S. Nolas group in the same way as $Sr_8Ga_{16}Ge_{30}$ [18]. The carrier freezout behavior was observed in the n-type samples, but not in the p-type.

After discovering that the low-T quadrupole T_1 could be used to characterize

rattling, we initiated a follow up study of $Ba_8Ga_{16}Ge_{30}$ to search for similar behavior. The n type sample made by Nolas' group was used for this investigation.

b. NMR results and discussion

NMR lineshape measurements for the central transition agree with the previous results [52], indicating that the sample is stable vs. time. In this work, I measured the spin-lattice relaxation at more than ten temperature points for both ^{69}Ga and ^{71}Ga at the peak of the lineshape. The magnetic and quadrupolar contributions have been separated following the same relationship as equation (5.1) and (5.2). The results are plotted in Fig. 31.

It is clear that the $1/T_1T$ behavior is different from that of type-I $Ba_8Ga_{16}Sn_{30}$, since an anharmonic rattling peak is not observed at low temperatures in the $1/T_1T$ plot. Also there is almost no quadrupolar contribution at temperatures below 100 K. Note that for both types of $Ba_8Ga_{16}Sn_{30}$, we observed a low temperature up-turn in the quadrupole relaxation rate, $1/T_{1Q}$, which is completely absent here. Although there is an up-turn in $1/T_{1M}$, the previously discussed anharmonic model would be expected to apply only to the quadrupole behavior, so it is not appropriate to use it here. At high temperatures, a mixed mechanism is in control and the magnetic relaxation rates for both nuclei are almost constant, indicating a high temperature Korringa-like relation. But, considering the Knight shift results from previous studies [52], where the shift was also defined as $K = \Delta f/f_0$, K^2T_1T still does not follow a Korringa-like behavior over the entire temperature range.

As shown in Fig. 32, the $1/T_1$ can be fitted with the disorder-tunneling model for amorphous materials, similar to the model used to analyze type-VIII $Ba_8Ga_{16}Sn_{30}$. Following equation (5.18), the $1/T_1$ can be fitted with $T^{1.4}$, and so $\alpha = 0.4$. It is interesting that the overall $1/T_1$ can be fitted to a very similar behavior to that of the

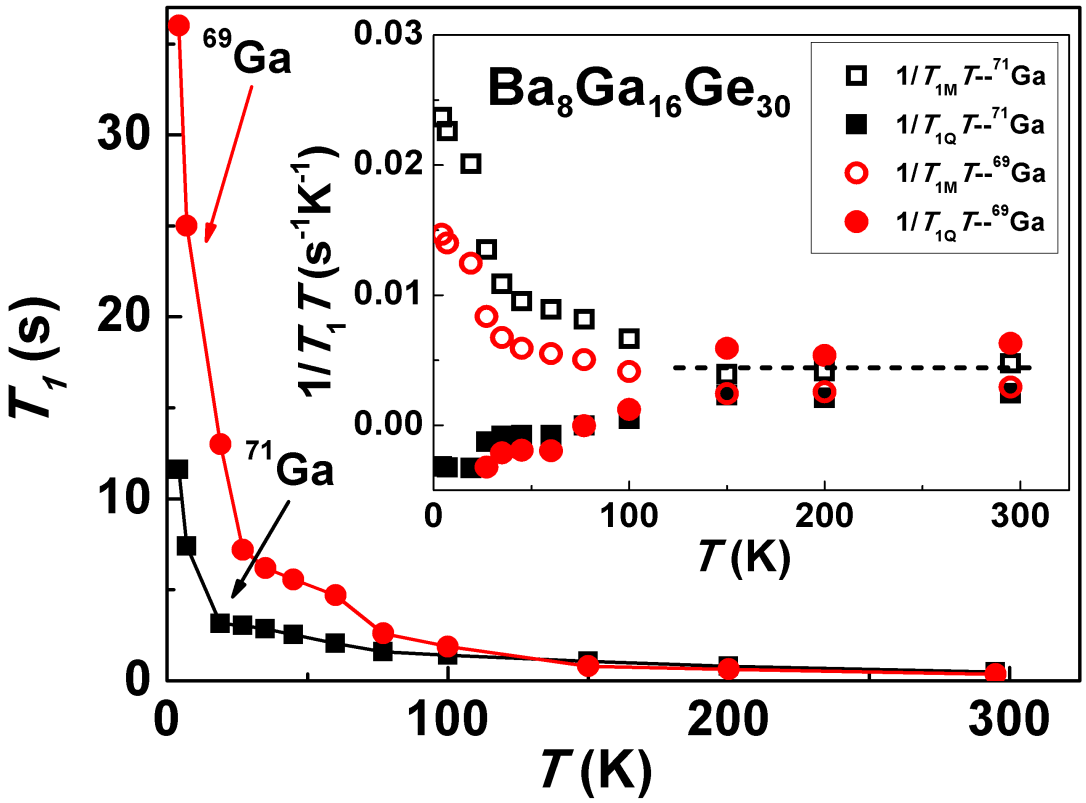

Fig. 31. Spin-lattice relaxation time (T_1) for ^{71}Ga (solid squares) and ^{69}Ga (solid circles) in $Ba_8Ga_{16}Ge_{30}$. Inset: Separated relaxation rates $1/T_1T$ for ^{71}Ga and ^{69}Ga. ^{69}Ga-quadrupole (solid circles), ^{69}Ga-magnetic (open circles), ^{71}Ga-quadrupole (solid squares), ^{71}Ga-magnetic (open squares).

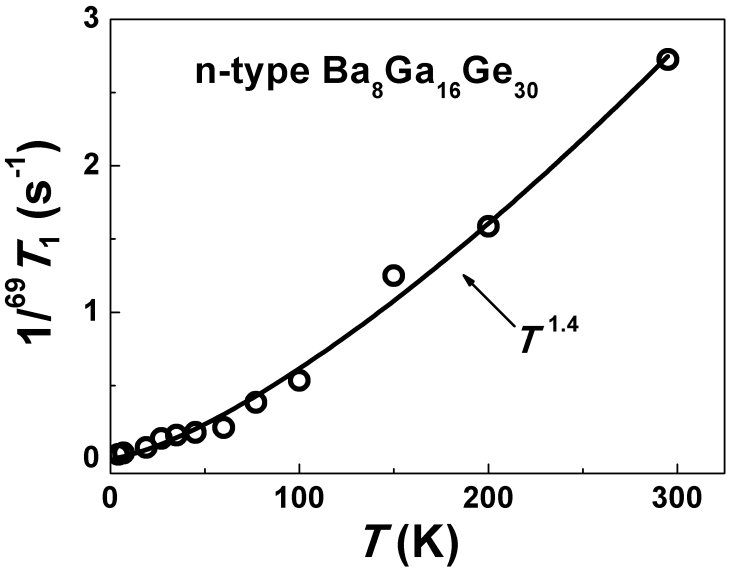

Fig. 32. The spin-lattice relaxation rates ($1/T_1$) of ^{69}Ga (open squares) with a fit (solid curve) from the amorphous assumption.

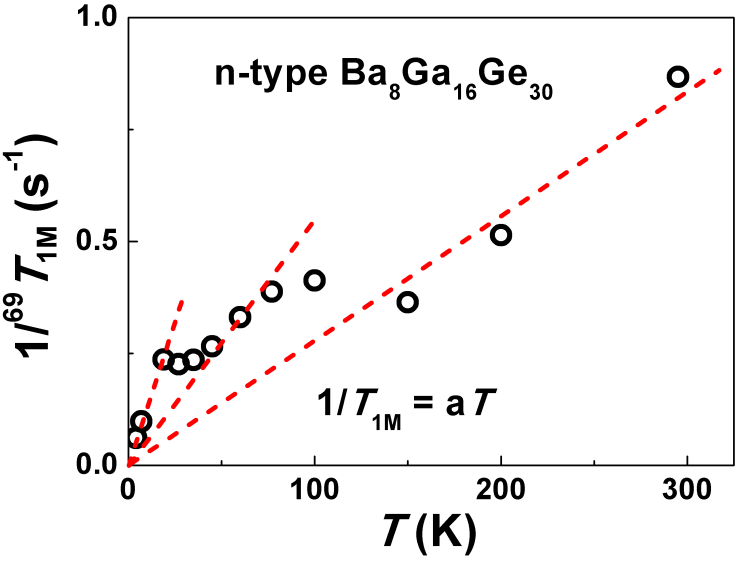

Fig. 33. ($1/T_{1M}$) of ^{69}Ga (open squares). It can be fitted to linear relations with temperature (dashed lines) in different temperature ranges.

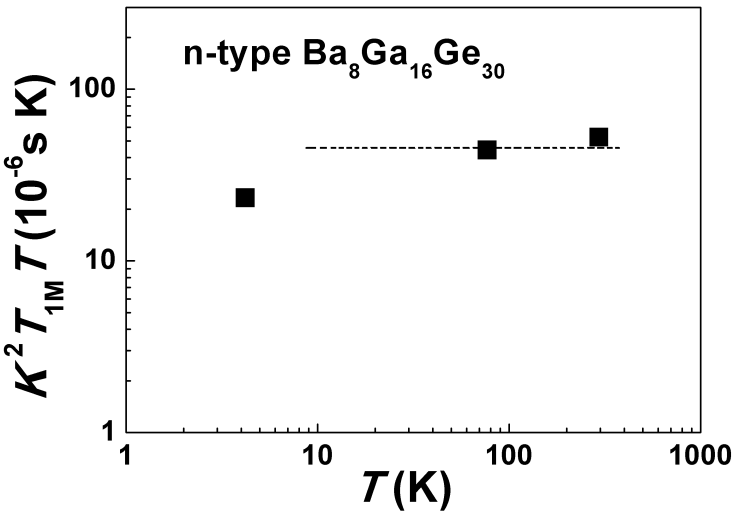

Fig. 34. K^2T_1T values for ^{71}Ga at the NMR central transition peak (solid squares) are plotted in log scale. It is close to a Korringa relation at high T (dashed line) with significant enhancement over the free electron value.

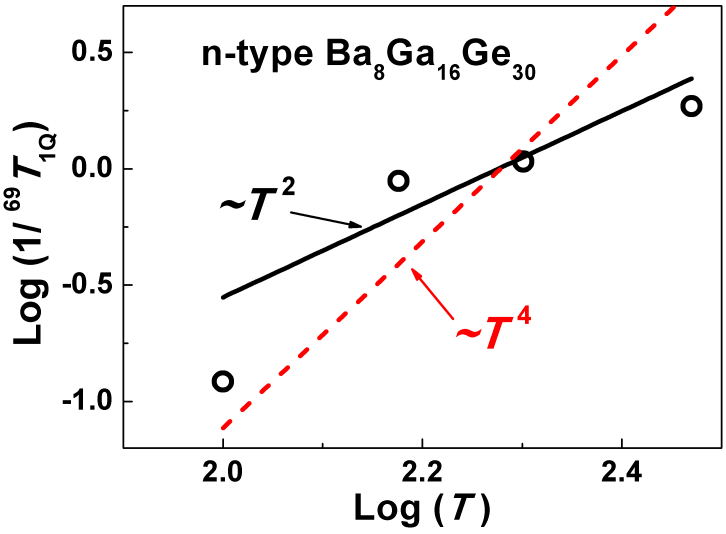

Fig. 35. The quadrupole spin-lattice relaxation rates ($1/T_{1Q}$) of ^{71}Ga (open squares) vs. T in log scale with a linear fit (solid line). A T^2 (solid line) and T^4 (dashed line) behavior from two/four phonon process are also plotted for comparison.

type-VIII $Ba_8Ga_{16}Sn_{30}$ clathrate, and also for type-I $Ba_8In_{16}Ge_{30}$ clathrate, as shown later. However, as for type-VIII $Ba_8Ga_{16}Sn_{30}$, since we identified that the quadrupole mechanism does not dominate, so this agreement may be fortuitous.

The T_1 behavior here cannot be analyzed according to the semiconducting model as we discussed previously [equation (5.19)] since the temperature dependence in this case is quite different. Taking the results from ^{69}Ga for example, as shown in Fig. 33, the magnetic $1/T_{1M}$ has no rise in $1/T_{1M}T$ as T increases. But we see that $1/T_{1M}$ values have linear relationships with T, $1/T_{1M} = aT$, for different temperature ranges, which may indicate some temperature-dependent change of the density of states or the carrier concentration. The existance of an impurity band is characteristic of semiconductor near the metal-insulator transition, and can explain the low-T enhancement of the $1/T_1T$. Similar situations have been discussed in heavily doped systems, such as Ge:As and Si:P [90, 91], where the NMR spin-lattice relaxation also departs from Korringa behaviors at low T. As $1/T_{1M}$ is a function of conduction band density of states, different $1/T_{1M}$ vs. T behavior is observed as the carriers settle into states hybridized with impurity states at the band edge at low T [91]. With the impurity band consisting of multiple peaks in the $g(E)$, it might be possible to have the step-like $1/T_{1M}T$ values at different temperature ranges similar to the situation here, although we are not aware of such behavior in other systems. Note that our sample is a n-type material with a pre-measured carrier density of $n = 8.7 \times 10^{19}$ cm^{-1}. From measurements of its Seebeck coefficient, it can be estimated from an effective mass approximation that $T_F \cong 600$ K [92]. Thus it is not very far into the metallic regime, and the impurity band assumption is a reasonable explanation for the T_{1M} vs. T behavior observed here.

Combining the magnetic $^{71}T_{1M}$ and Gou's K values, the renormalized $K^2T_{1M}T$ becomes more like the expected Korringa behavior than with the overall T_1 [52],

especially at high temperatures, as shown in Fig. 34. The $K^2T_{1M}T$ values exhibit a large enhancement compared to the free electron value. This indicates that the magnetic contribution may still follow the Korringa relation at high temperatures.

The quadrupole T_{1Q} is expected to be controled by phonon interactions. For itinerant phonons, there are two accepted models, associated with a two-phonon and four-phonon process [93], which give $1/T_{1Q} \sim T^2$ or $1/T_{1Q} \sim T^4$ at high temperatures correspondingly. In Fig. 35 we plot the $1/T_{1Q}$ vs. T in a log scale and perform a linear fit. As the quadrupole term is turned off below 77K, only a few points at higher temperatures are used here. The solid and dashed lines represent the standard T^2 and T^4 behavior. It seems T^4 cannot describe the experimental data very well. But the T^2 behavior does give a closer fit for the higher temperature data with a drop off at lower temperatures below Debye temperature, which agrees with the theory and is similar to the observation of the two phonon process for semiconducting materials, such as InP [93]. So it is reasonable to believe that the quadrupole relaxation is dominated by phonon interaction in the material at high temperatures.

c. Summary

No anharmonic rattling behavior is observed here, which is not a surprise as the guest free space is relatively small in $Ba_8Ga_{16}Ge_{30}$. The $1/T_{1M}$ data and fits can be explained by the impurity band structures, while the high temperature up turn of the $1/T_{1Q}$ agrees with the two-phonon T^2 behavior. A Korringa relation is also found at high temperatures. All these results offer additional understanding to our previous studies.

2. Type-I $Ba_8In_{16}Ge_{30}$

Similar to other group IV intermetallic clathrates, $Ba_8In_xGe_{46-x}$ has been also considered for potential thermoelectric applications. As In is a bigger atom, it is reasonable to expect a slightly larger cage for Ba, which has been confirmed by structural studies [26]. As shown earlier in Fig. 3, the large guest free space value might lead to anharmonic rattling behavior as observed in type-I $Ba_8Ga_{16}Sn_{30}$. In this work, type-I $Ba_8In_{16}Ge_{30}$ was investigatied.

a. Sample preparation

This sample was prepared by our group member, Laziz K. Saribaev with an In flux method. The pure elements Ba, In and Ge were mixed together based on the ratio of 8:24:30 in a glove box with nitrogen atmosphere. The sample was then sealed in a quartz tube and heated to 1150 °C over 10 hours. After staying at 1150 °C for 3 hours, it was cooled to 1000 °C over 10 hours, then from 1000 °C to 400 °C over 5 days. After another annealing at 400 °C for 2 hours, the sample was immediately centrifuged to remove excess indium. Crystal-like samples were found. XRD and the refinement results confirmed the structure to be type-I.

b. NMR results and discussion

As the sample was expected to show rattling behavior, I did NMR measurements for this sample similar to those for the type-I Type-I $Ba_8Ga_{16}Sn_{30}$. The NMR measurements were performed under 8.8 T external field at 295 K, 77 K and 4.2 K. The nucleus measured is ^{115}In.

The NMR central transition lineshapes from 295 K and 77 K are shown in Fig. 36, with all amplitudes corrected by corresponding temperature factors due to

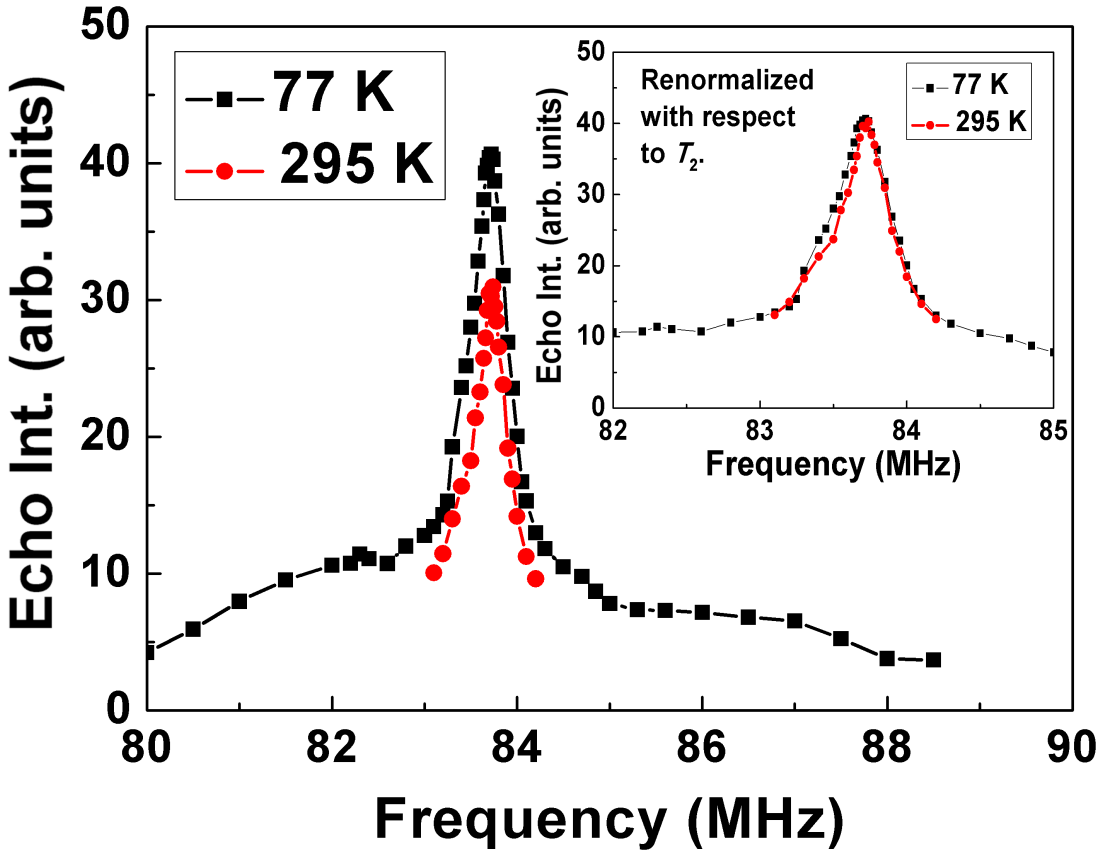

Fig. 36. ^{115}In NMR lineshape for $Ba_8In_{16}Ge_{30}$ clathrate at 295 K (solid circles) and 77 K (solid squares) after temperature correction. Inset: Comparison between the same NMR lineshapes after further renormalization with respect to T_2 results. The small frequency shift and linewidth change cannot be discerned due to the large linewidth.

the temperature-dependent Boltzmann distribution. Note that the 77 K lineshape does not only contain a central transition peak, the central portion with a width about 1 MHz, but also a huge first order quadrupole broadened background. It is clear from the amplitudes at the two temperatures that the central transition signal amplitude does not follow a standard temperature ratio, and it is reasonable to believe that a temperature-dependent in-plane fast dephasing process might be the explanation. This can be tested by spin-spin relaxation (T_2) measurements. Note that due to the huge linewidth for this material, the Knight shift difference between the two temperatures is too small to be seen from the plot.

Compared with other clathrate samples we studied in this work, the linewidth ($FWHM$) for $Ba_8In_{16}Ge_{30}$ is much larger. We have $FWHM \cong 60$ and 50 kHz for ^{71}Ga lineshape of type-I and type-VIII $Ba_8Ga_{16}Sn_{30}$, whereas ^{71}Ga of $Ba_8Ga_{16}Ge_{30}$ gives $FWHM \cong 60$ kHz [52]. But here, $FWHM \cong 500$ kHz for ^{115}In is much larger. *Ab-initio* calculations [94] have produced a good fit to the 1^{st} order part of this lineshape but as compared with other materials, a much larger set of superstructures each gave a reasonable fit. So, a wide distribution of local environments may characterize this material. T_1 has been measured at 3 different frequencies, $\Delta f/f_0 = 0.0011, 0.0021, 0.0029$, within the central transition portion of the peak in order to check if metallic broadening was involved. The T_1 values are almost the same for these three positions, indicating non-metallic broadening. Also, the quadrupole moment Q is about eight times bigger for ^{115}In than that of ^{71}Ga, so the quadrupole broadening is likely to be responsible for the big difference in the linewidth.

Standard Hahn-Echo sequences with variable T_{DEL} settings were used for the T_2 measurements at 295 K, 77 K, and 4.2 K. The results are plotted in Fig. 37. Equation (3.20), $M(2T_{Delay}) = M_0 \left[\alpha \cdot exp\{-\frac{2T_{Delay}}{T_{2e}}\} + exp\{-\left(\frac{2T_{Delay}}{T_{2g}}\right)^2\}\right]$, was used for the fitted curves shown in the figure. The fitted T_2 results and weighting ratio (α)

are listed in Table. II. The dephasing process mostly follows an exponential decay at room temperature, whereas the static-type Gaussian component has to be taken into consideration at low temperatures. Relaxation times for both contributions grow rapidly as the temperature decreases. Comparing the data from 295 K and 77 K, it is the significantly growing exponential contribution that determines the difference of the lineshape amplitude between the two temperatures. Also, compared to the results from $Sr_8Ga_{16}Ge_{30}$ [51, 52], the T_2 values are much smaller in this case.

A slow motion model may offer a good explanation for the small T_2 and its temperature dependent behavior. This has been discussed in the work of Dr. Weiping Gou [51, 52]. The model describes a physical motion of atoms in the framework or guest positions which can change the local field gradient by a small amount. If the frequency of the motion is comparable to the intrinsic spin-spin relaxation rate ($1/T_2$), then it will accelerate the dephasing process during every pulse sequence period, which will lead to a smaller T_2. If the motion frequency is too large, time averaging will cancel the effect. This is called motional narrowing. If it is too small, then no significant influence will be seen. Atomic motions are usually temperature dependent. For thermally activated motion, the frequencies will get larger at higher temperatures, and in the strong interacting regime ($T_2 \sim \tau$) the corresponding relaxation time will become smaller. This will happen at lower temperatures. If the temperature is too high, then either the motion is fast enough so that time averaging occurs, or the material melts and its relaxation time returns to larger values.

Paramagnetic impurities could be an alternative explanation for the change in T_2, as electron spin flip-flops can also affect the local fields and influence the dephasing process accordingly. Later, we will see from susceptibility results that paramagnetism is unlikely to exist in this material at a level required for this mechanism.

In order to investigate the expected rattling behavior of this sample, I also mea-

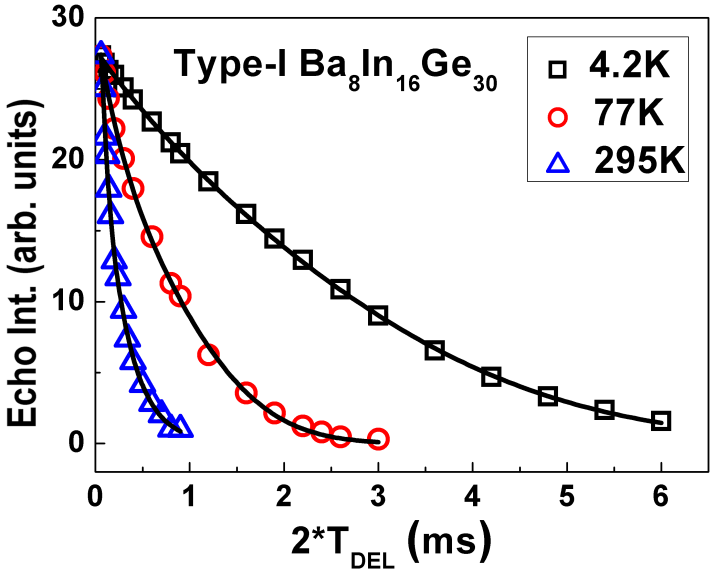

Fig. 37. Spin-spin relaxation (T_2) measurements of $Ba_8In_{16}Ge_{30}$ clathrate at 4.2 K (open squares), 77 K (open circles) and 295 K (open triangles). The fits (solid curves) for all cases from equation (3.20) are also shown for comparison. Hahn-Echo sequences with variable T_{DEL} were used here.

Table II. Fitted T_2 and parameters from equation (3.20) measured at the peak of the central transition.

Temperature (K)	α	$T_{2e}(\mu s)$	$T_{2g}(\mu s)$
295	4.52	257.2	107.9
77	1.22	369.7	1363.8
4.2	1.45	1741.7	3791.7

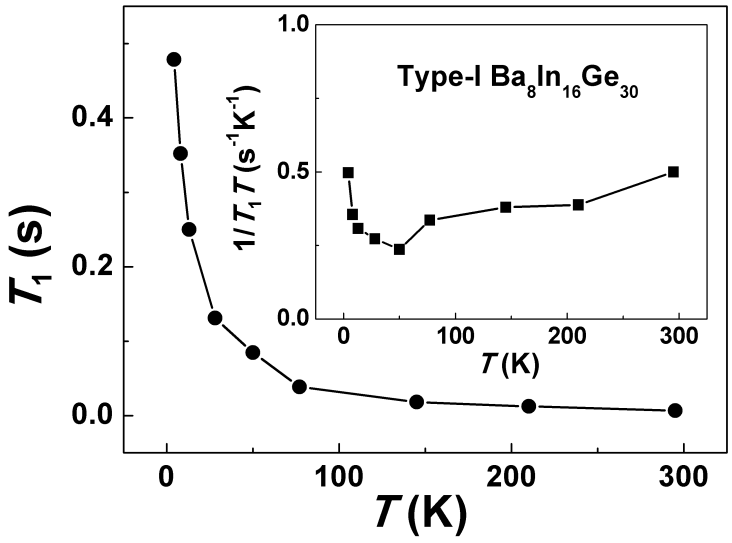

Fig. 38. T_1 for ^{115}In of $Ba_8In_{16}Ge_{30}$ clathrate (solid circles). Inset: corresponding $1/T_1T$ values (solid squares). We observe no anharmonic behavior as found in type-I BaGaSn clathrate.

sured the spin-lattice relaxation time (T_1) vs. temperature. The data are shown in Fig. 38. As the natural abundance of the second isotope, ^{113}In, is too small and the gyromagnetic ratio is too close to ^{115}In, it is not possible to perform NMR measurements on both nuclei and separate the quadrupolar and magnetic contributions to the relaxation process. But from the overall relaxation rates, plotted in the inset of Fig. 38, we do not see the same rattling behavior as discussed earlier for type-I $Ba_8Ga_{16}Sn_{30}$. Instead, the relaxation behavior is closer to that of the type-VIII $Ba_8Ga_{16}Sn_{30}$, because no peak is observed in $1/T_1T$.

Recall that, as described previously, the T_1 of type-VIII $Ba_8Ga_{16}Sn_{30}$ can be fitted by a disorder-tunneling model, $T_1^{-1} \propto T^{\alpha}$, $\alpha = 1 + 2\eta$, at low temperatures ($K_BT \ll E_m$), with $\rho_D(E) = \rho_0 E^{\eta}$, representing an energy dependent density of tunneling modes. As shown in Fig. 39, T_1 of $Ba_8In_{16}Ge_{30}$ can also be fitted by the

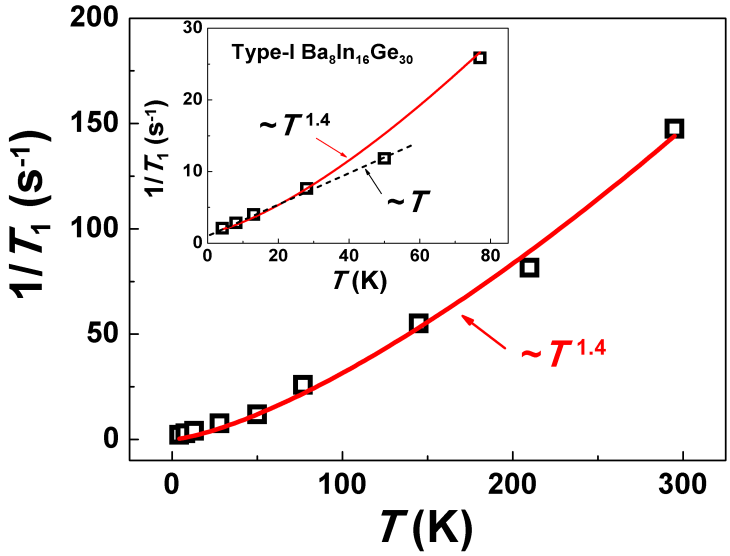

Fig. 39. $1/T_1$ of ^{115}In (open squares) and a $T^{1.4}$ fit (solid curve) from the disorder model. Inset: $(1/T_1)$ of ^{115}In (open squares), a $T^{1.4}$ fit (solid curve) and a linear fit (dashed line) at low temperatures.

same model for the entire temperature range. The fitted value of α is 0.4, which is very close to the values found for type-VIII $Ba_8Ga_{16}Sn_{30}$ and $Ba_8Ga_{16}Ge_{30}$, as remarked before. Taking a closer look at the low temperature region, the T_1^{-1} can still be fitted to $T^{1.4}$. However a linear behavior can also give a reasonable fit, as shown in the inset of Fig. 39, indicating some uncertainty for the exponent α. Because we cannot separate the quadrupole and magnetic parts, it is possible that this model provides the physical explanation for the observed T_1, however since the Korringa relation is also obeyed, as shown below, an explanation based on carrier interactions seems more likely.

But, note that, no magnetic and quadrupole contributions have been separated from the overall T_1 fit. So it is possible that the up turn of the $1/T_1$ at high temperatures is due to regular phonon interactions instead of the electronic structures.

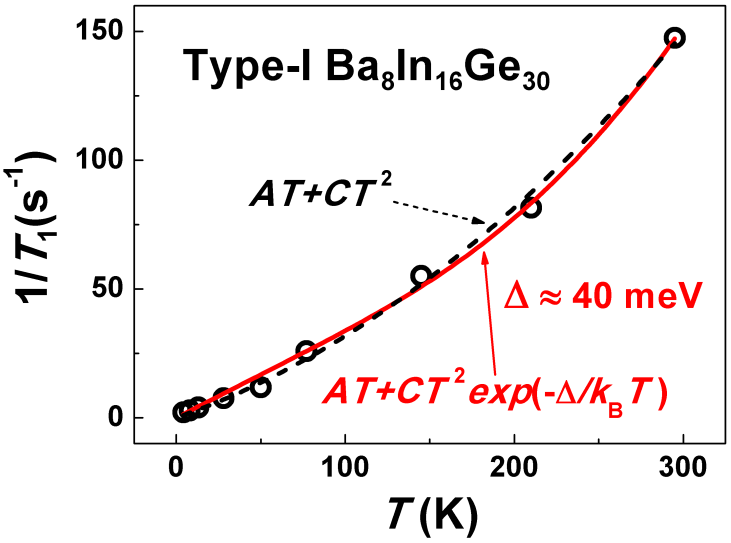

Fig. 40. $1/T_1$ of ^{115}In (open circles) and a fit (solid curve) from the semiconducting two-band model. A fit containing only a Korringa term and a two-phonon quadrupole term can also provide a resonable fit (dashed curve).

A fit including only a Korringa term and a two-phonon quadrupole contribution, $1/T_1 = AT + CT^2$, can be used here, as shown in Fig. 40. The fit is similar to that of the semiconducting assumption.

The semiconducting model discussed previously for both type-VIII $Ba_8Ga_{16}Sn_{30}$ and $Ba_8Ga_{16}Ge_{30}$ can also be applied to this sample. Following a similar procedure as in equation (5.19), the fitted result is shown in Fig. 40, with a fitted energy gap $\Delta \cong 40$ meV and a large uncertainty of about ± 23 meV. The fit looks good, and the small fitted gap implies that the behavior is close to an ordinary metal, with a shallow psedogap if any. Later, we will also see that the Korringa behavior is followed here as the NMR frequency shift increases with T. This indicates a metallic property, which agrees with the fact that a Korringa term was obtained from the fit. Thus it seems reasonable that a small pseudo-gaps may contribute to the T_1 behavior. This

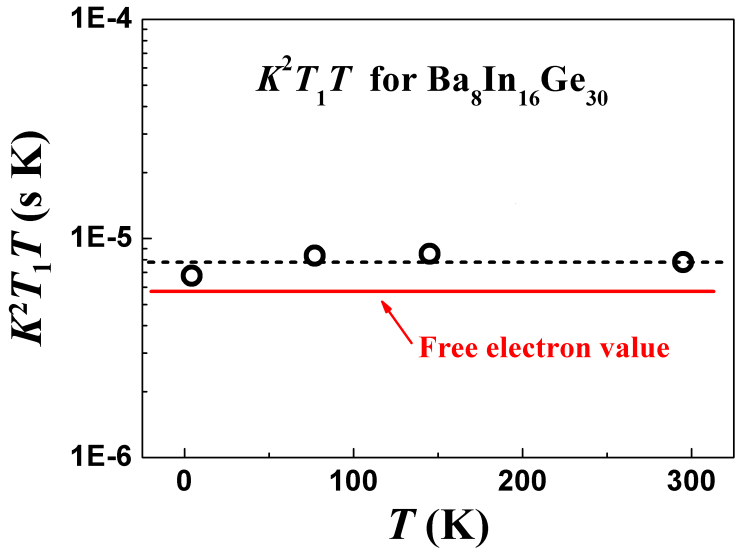

Fig. 41. The values of K^2T_1T for the In NMR central transition peak (open circles) at 4.2 K, 77 K and 295 K are plotted in log scale, with a horizontal guide line (dashed line). The data are nearly constant and close to the Korringa relationship

is similar to the case of type-VIII $Ba_8Ga_{16}Sn_{30}$ as discussed previously.

Furthermore, the frequency shifts, labeled as K, were calculated from the mass center of the Gaussian fit to the central transition with an average error less than 0.01%. The corresponding K values for 4.2 K, 77 K, 145 K and 295 K are 0.183%, 0.168%, 0.181% and 0.197%, showing a relatively small change vs. T compared to its large line width. The corresponding K^2T_1T values were calculated and plotted in Fig. 41 on a log scale. The result is close to the Korringa relation with a value close to the theoretical value from the free-electron assumption, which is 5.6×10^{-6} s K. So, the type-I $Ba_8In_{16}Ge_{30}$ sample can be considered as metallic for which the conduction electrons offer the largest contribution to the relaxation behavior. So it is reasonable to use a model with both metallic and pseudo-gap contributions to analysis the T_1 behavior, as we did above with the semiconducting model. Note that, in principle,

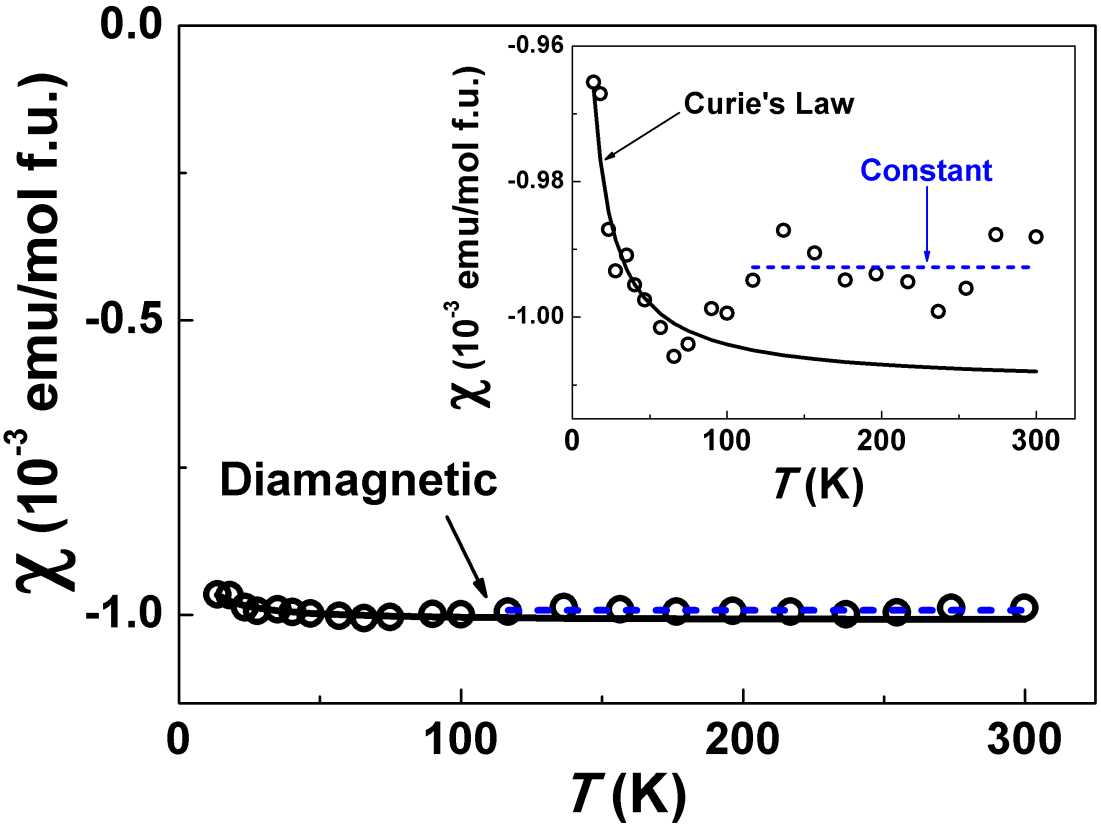

Fig. 42. Susceptibility of type-I $Ba_8In_{16}Ge_{30}$ (open circles). It can be treated as a negative constant over the entire temperature range. Inset: A closer look at the susceptibility. At low temperatures, it can be fitted by the Curie's law (solid line), while in high temperatures it tends to be a constant (dashed line).

the K values used here not only contain the Knight shift, but also a chemical shift and quadrupole shift, which may lead to some variation of the K^2T_1T values.

A measurement of magnetic susceptibility was performed on a Quantum Design SQUID system. The external field was set at 1000 Oe, and the measurement covered a temperature range between 13 K and 300 K. The results are plotted in Fig. 42. As shown in the inset of Fig. 42, the data can be fitted by a Curie law tail, $\chi = \frac{C}{T} + const$, at low temperatures, but with an excedingly small C. Therefore, the susceptibility can be treated as a constant with a negative value, and the material is diamagnetic.

c. Summary

According to the discussions above, type-I $Ba_8In_{16}Ge_{30}$ is a metallic material that is diamagnetic. Its spin-lattice ralaxation behavior is similar to that of the type-VIII $Ba_8Ga_{16}Sn_{30}$, which has an upturn in $1/T_1T$ at low temperatures but no anharmonic peak. The metallic behavior indicates a large contribution of the conduction electrons, and therefore T_1 will not be dominated by the amorphous disorder tunneling or phonon interactions. Consequently the semiconducting assumption is believed to be the best explanation. Also, the temperature dependence of T_2 indicates a motion dominated dephasing process at high temperatures.

3. $Ba_8Cu_xGe_{46-x}$

Previous studies indicate that x=5.3 is the most preferred composition for this material, which agrees with the Zintl concept [89]. A series of $Ba_8Cu_xGe_{46-x}$ clathrate samples, x=4, 5.3 and 6, have been studied using NMR in this work. Dr. Sergio Rodriguez and Jing-Han Chen, our group members, also did first principles calculations to fit the NMR results and further explore the electronic behavior.

a. Sample preparation

Pure elements were mixed together based on the nominal composition followed by an initial arc melting in argon environment. An annealing process was performed in an evacuated quartz tube at 950 °C for 70 hours, followed by another at 700 °C for 90 hours. Note that the x values in the following discussion represent the starting composition. The $x = 5.3$ sample was made by myself, whereas the other two were prepared by Dr. Sergio Rodriguez.

b. NMR results and discussion

NMR measurements were performed on ^{63}Cu. The NMR central transition lineshapes were measured at 295 K for all three samples and the results are plotted in Fig. 43. The linewidth (FWHM) of the sharp peak decreases as x increases, but the variation is small, only a few percent, as shown in Fig. 43 (d). No significant change of the prominent sharp peak has been observed, but a second smaller contribution, possibly from a different site, grows as x increases. This is the small high frequency peak in the plot. From our *ab-initio* calculations, it is found that Cu atoms perfer to occupy the 6c site. For compositions with small x, only 6c sites are expected to be occupied by Cu. By increasing Cu, when x gets closer to 6, excess Cu will start to occupy other sites, which gives a possible explanation for the extra high frequency peak for the high Cu composition sample.

The spin-lattice relaxation time (T_1) was measured at room temperature for all three compositions at the position of the sharp peak, as shown in the inset of Fig. 44. With increasing x, a rapid increase of T_1 was observed. So, although there is no significant change of the central transition spectrum between different compositions, the relaxation process of the spin system does change. When x is small, the relaxation

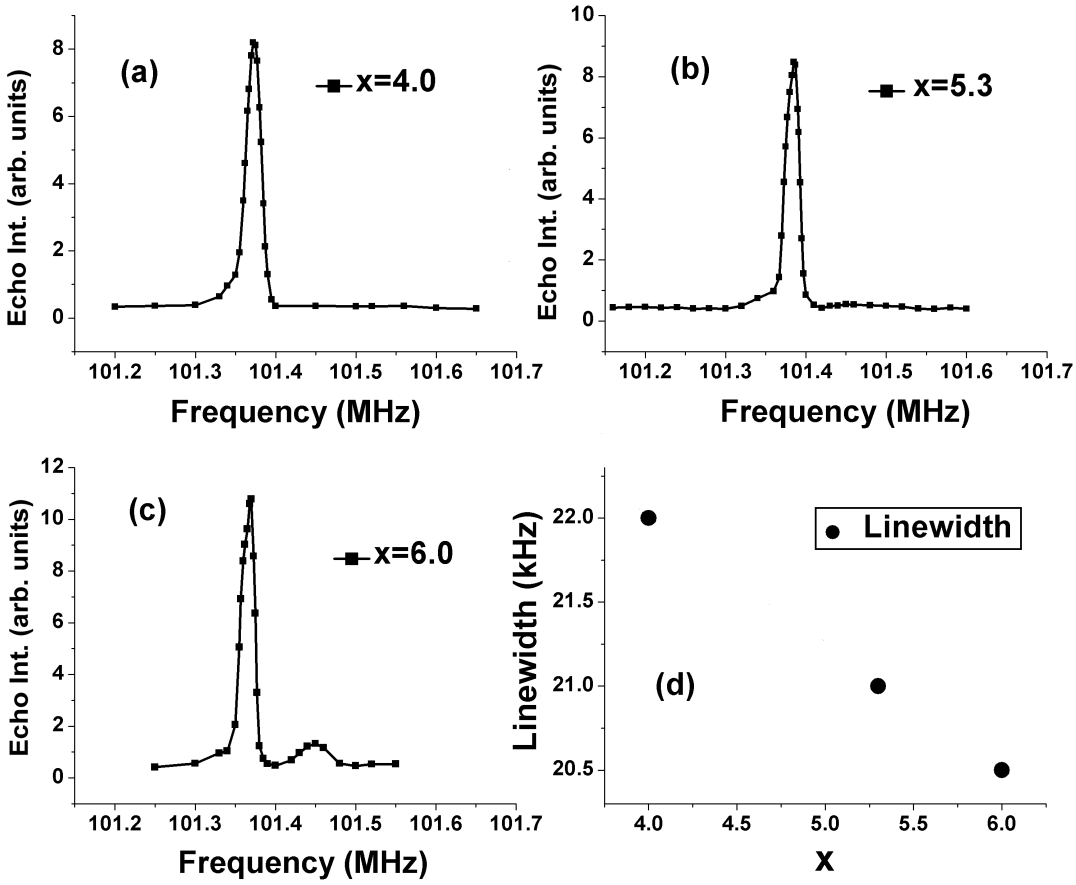

Fig. 43. ^{63}Cu NMR central lineshape comparison between $Ba_8Cu_xGe_{46-x}$ with x =4.0 (a), 5.3 (b) and 6.0 (c) at room temperature. Also, the linewidth of the main peak (solid circles) for three cases is compared in (d). The linewidth decreases as x increases.

is much faster. This behavior is presumably caused by the carrier type difference in these samples. As $x = 5.3$ is the Zintl phase, $x = 4.0$ is likely to be an n-type semiconductor, while $x = 6.0$ would be p-type. It has been observed in other semiconductors that p-type can have a longer relaxation time than n-type because of the difference in their band structure and it seems possible that this occurs for $Ba_8Cu_xGe_{46-x}$. Note that all three samples have large T_1 values, implying a small carrier density, which does correspond to the expected Zintl composition.

Additional measurements were concentrated on the composition $x = 5.3$. Fig.44 shows the T_1 results from 4.2 K, 77 K and 295 K. Fig. 45 shows the frequency shift of the mass center, labeled as K, as a function of temperature, and the inset shows the corresponding K^2T_1T values. The shift is nearly constant, exhibiting a small increase linear with temperature, but the Korringa relation is not followed, as K^2T_1T values are not constant vs. T, and the K^2T_1T values are too big compared to the free electron value for ^{63}Cu, which is 3.7×10^{-6} s·K. This result is presumably also due to the non-metallic characteristic of the $Ba_8Cu_xGe_{46-x}$ materials near $x = 5.3$. In contrast to the other materials examined in this thesis, K is dominated by a non-metallic chemical shift, and thus K^2T_1T is not representative of Korringa behavior.

Our group member, Jing-Han Chen, also did first principle calculations based on different compositions, comparing the resulting theoretical NMR lineshapes with the experimental data. Fig. 46 shows the case for $x = 5.3$. The specific configuration with Cu occupying only 6c sites matches the experimental results very well. This gives another way to confirm the local structure of the sample. Also, the results offer additional information about the quadrupolar broadening in the material. The calculated value of ν_Q is small for this material, indicating a small quadrupole contribution to the central line shift. We are currently planning to use these results as a measure to further analyze the chemical shift and Knight shift.

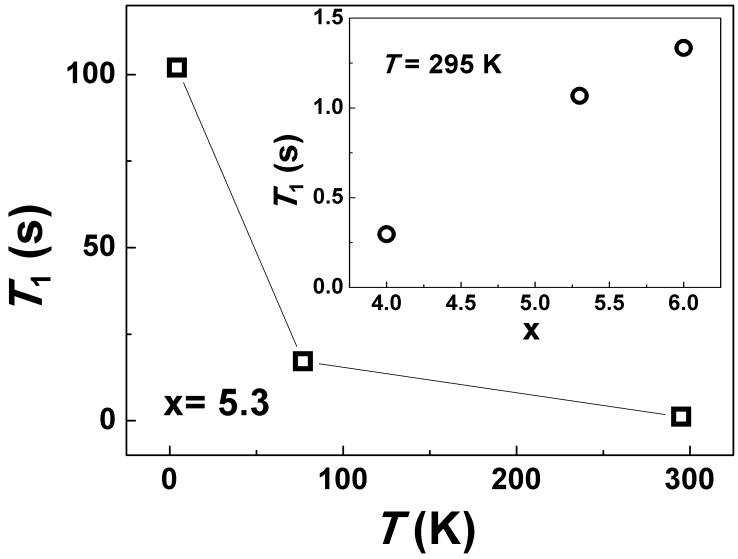

Fig. 44. The ^{63}Cu NMR T_1 for the central transition (open squares) at 4.2 K, 77 K and 295 K. Inset: Comparison of T_1 for $x = 4.0$, 5.3 and 6.0 at 295 K. T_1 grows nearly linearly as x increases for $Ba_8Cu_xGe_{46-x}$.

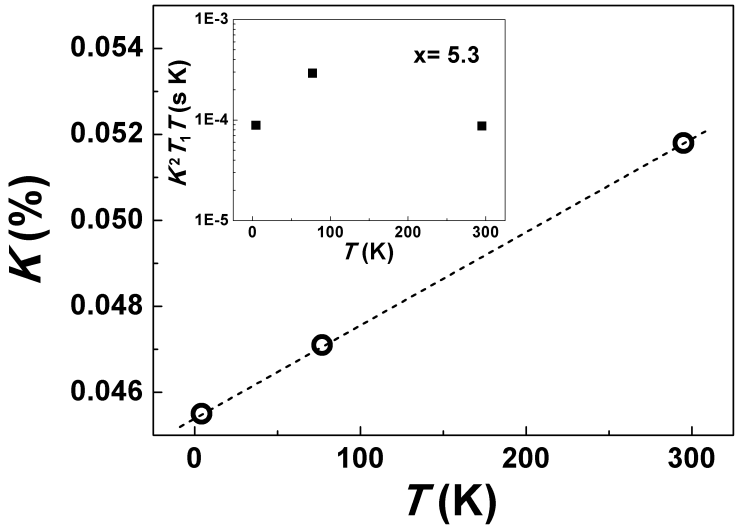

Fig. 45. Knight shift value for the central transition at 4.2 K, 77 K and 295 K for $Ba_8Cu_xGe_{46-x}$ with $x = 5.3$. K grows as T increases. Inset: Calculated K^2T_1T, which does not follow the standard Korriga relationship.

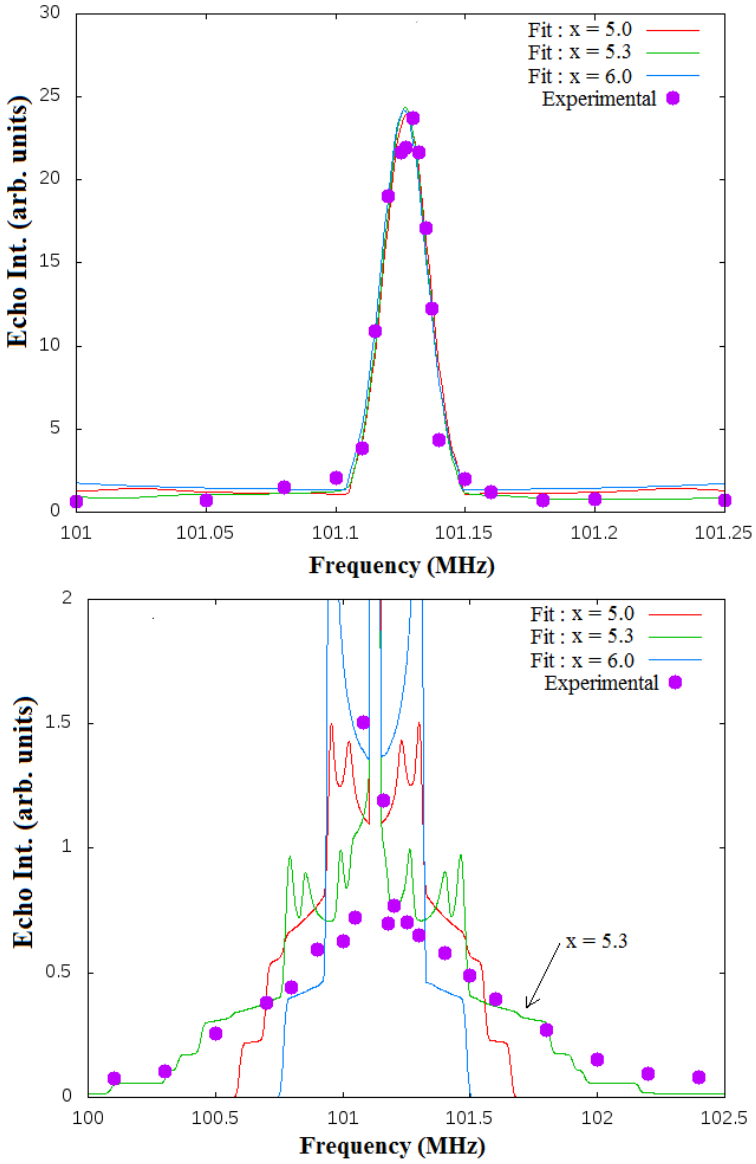

Fig. 46. ^{63}Cu NMR lineshape for $Ba_8Cu_xGe_{46-x}$ with $x = 5.3$ at 77 K (solid circles) compared with calculated results with different compositions. For calculated configurations, mixed occupation of the alloy is modeled as a superstructure. A 3×1 superlattice with Cu occupying only 6c sites gives the best match to the experimental data. (a) is the central line region, and (b) is the detailed fit expanded to show the baseline broadening.

D. Layered $BaGa_3Sn$

$BaGa_4$ and $BaGa_3Sn$ are not clathrates but layered materials sharing the same structure as $BaAl_4$, shown in Fig. 47. They are close to being Zintl phases, in fact these and other materials are expected to exhibit pseudogap structures due to Zintl-like behavior [95]. Thus we decided to study their properties for comparison in order to better understand the stability and structure of the related BaGaSn clathrates.

1. Sample preparation

These two samples studied were prepared by Dr. Sergio Rodriguez. A proper amount of the pure elements was mixed together and heated to 850 °C for one day, followed by a one week annealing at 550 °C. Rietveld refinement of the XRD results confirmed the structure and pure phase of the sample. $BaGa_3Sn$ is a new material which has been little studied. It was originally formed as an extra phase when preparing clathrate samples. The XRD results and refinements for both samples are shown in Fig. 48. $BaGa_4$ has a perfect tetragonal structure and the refinements agree with this quite well. For $BaGa_3Sn$, a standard tetragonal structure gave a reasonable fit in the refinement of the XRD, but with reflections apparently slightly displaced. Including a small orthorhombic distortion led to the improved fit as shown. The lattice parameters are compared in Table. III. A tiny amount of Ga metal was also detected in the $BaGa_4$ sample as a second phase.

2. NMR results and discussion

^{71}Ga NMR lineshapes of $BaGa_3Sn$ and $BaGa_4$ at different temperatures are shown in Fig. 49. The lineshapes for both samples contain two peak groups, one sharp peak at a lower frequency (peak-I) and one broader peak at a higher frequency

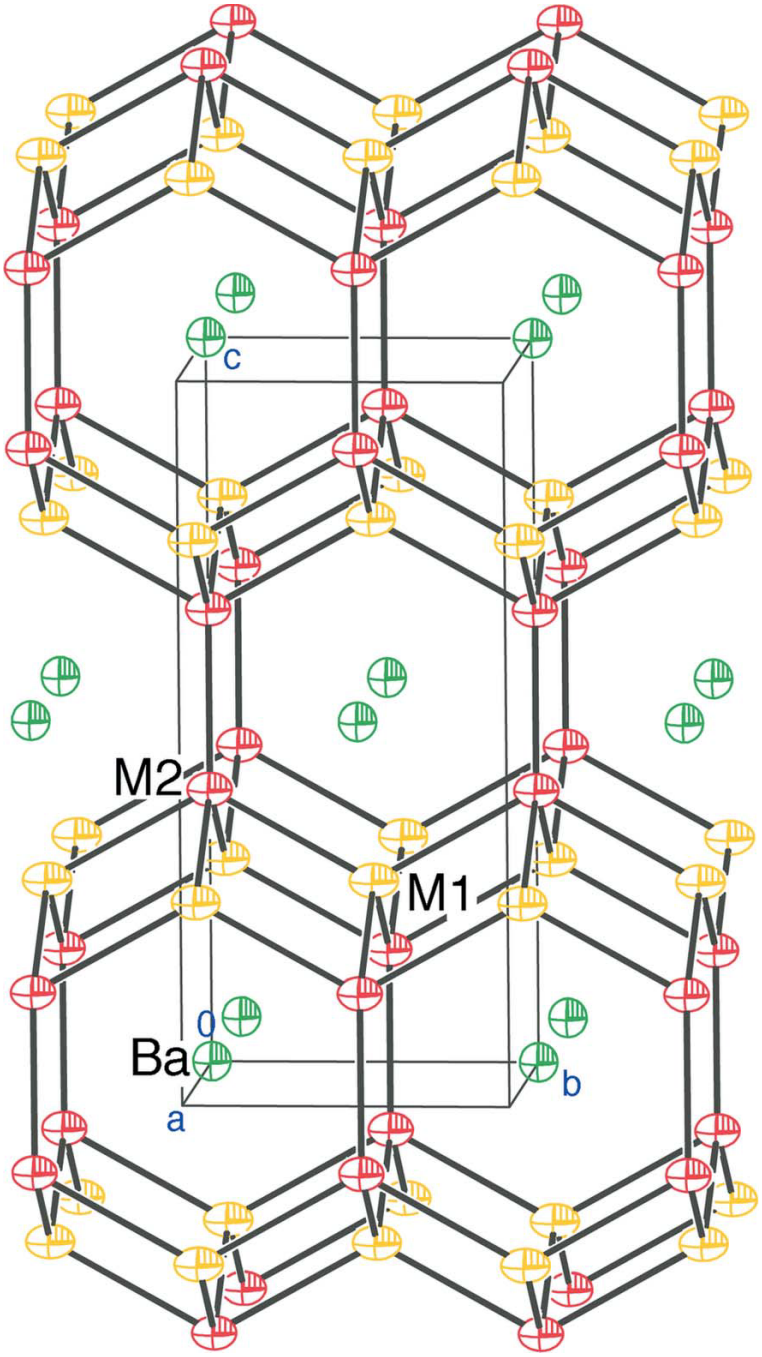

Fig. 47. Layered structure of $BaGa_4$. M1 and M2 represent two Ga sites. Reprinted figure with permission from [97] ©(2007) by International Union of Crystallography.

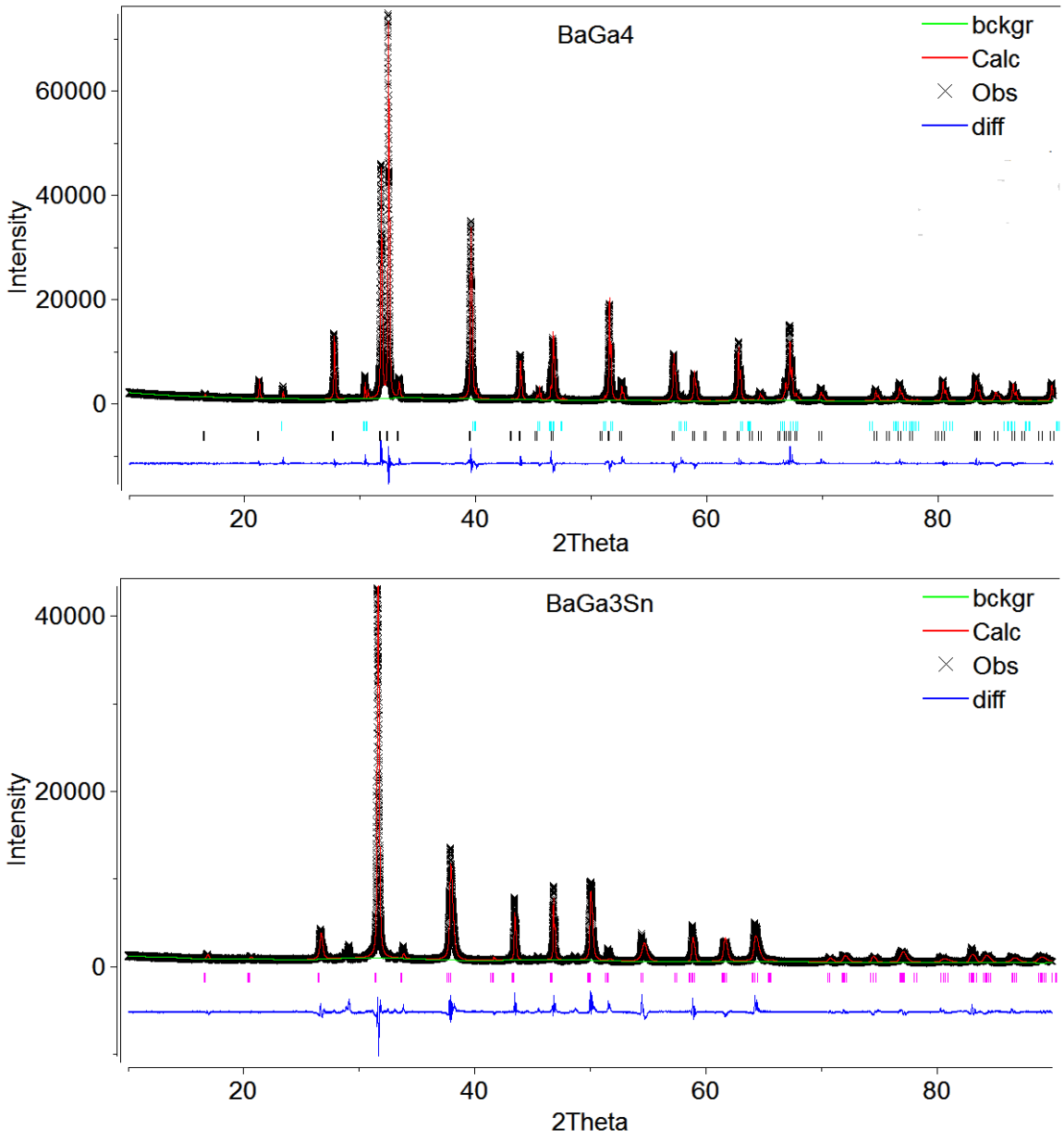

Fig. 48. X-ray result and refinements for the layered $BaGa_4$ (upper) and $BaGa_3Sn$ (lower).

Table III. Comparison of fitted lattice parameters from XRD refinements of $BaGa_4$ and $BaGa_3Sn$.

	Space group	a (Å)	b (Å)	c (Å)
$BaGa_4$	I4/m m	4.5657	4.5657	10.7781
$BaGa_3Sn$	Immm	4.7754	4.7567	10.6717

(peak-II). These are clearly due to two main Ga sites in the structure. The $BaGa_4$ results are similar to previous studies [96, 97]. For $BaGa_3Sn$, based on the areas under each peak, we find that the two sites are nearly equally occupied by the Ga atoms. Also, the MAS spectrum, as shown in Fig. 50, has no clear narrowing compared to the static NMR results.

In Fig. 49, all the amplitudes have been renomalized according to the temperature. It is interesting that peak-II does not follow the standard temperature ratio as peak-I does, and no significant change in the broadening is observed. So it is reasonable to check for a difference in atomic dynamics as measured by the spin-spin relaxation (T_2). And note that all the T_2 measurements and discussion below are focused on peak-II.

T_2 measurements were performed on peak-II for ^{71}Ga. According to equation (3.20), T_2 is a fitted value from Hahn-Echo measurements with different T_{DEL} values, shown in Fig. 51. The results are all renormalized for comparison, and the fast T_2 relaxation at higher temperatures indicates possible hopping-type atomic dynamics in these two materials.

It is clear that the fitted T_{2e} and T_{2g} values, shown in Table IV and Table V, all increase rapidly as the temperature drops for both samples. This indicates that the NMR echo signal dies out much faster at room temperature than at lower tempera-

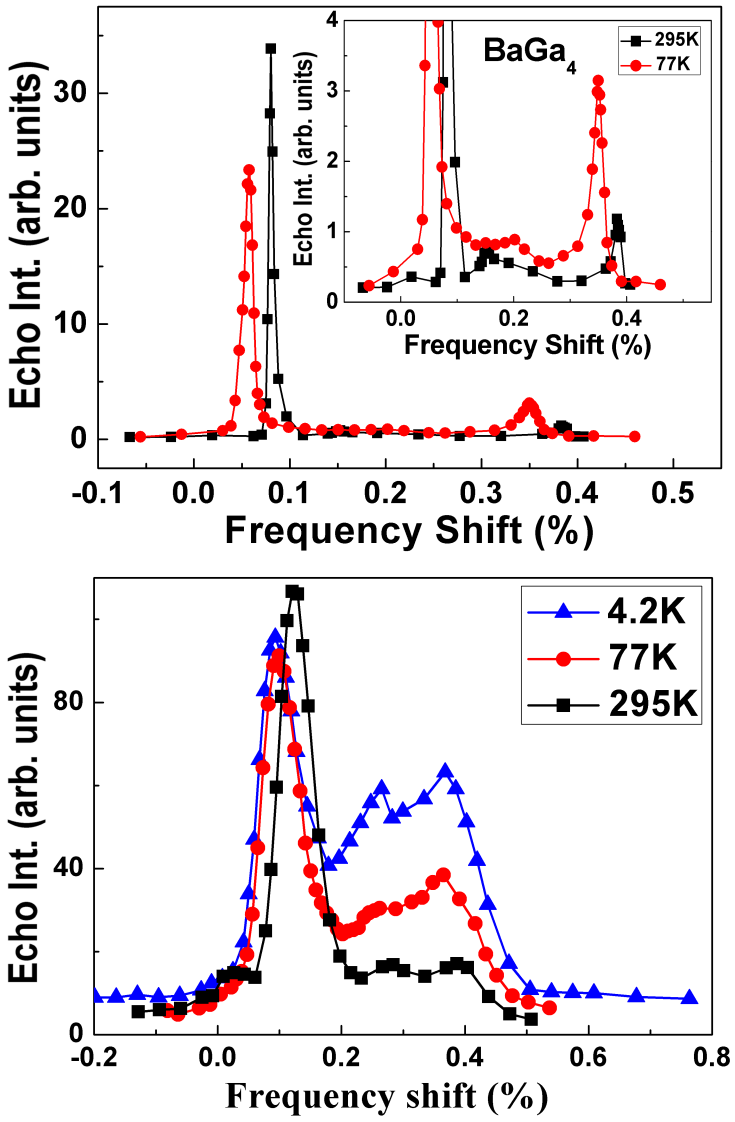

Fig. 49. ^{71}Ga NMR lineshape measurements for layered $BaGa_4$ (upper plot) and $BaGa_3Sn$ (lower plot) vs. temperature. The inset of the $BaGa_4$ figure shows a expanded view of the higher frequency peak.

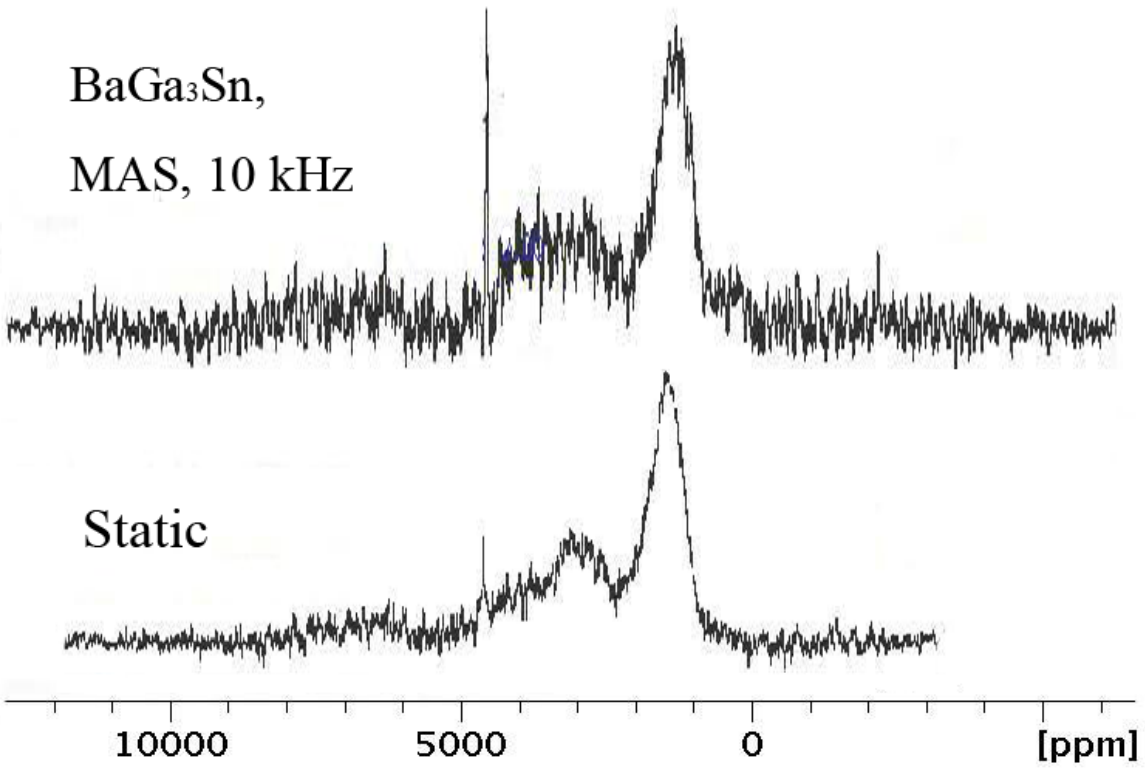

Fig. 50. ^{71}Ga NMR spectrum from magic angle spinning measurements with rotating speed of 10 kHz (upper plot). No significant linewidth narrowing is observed compared with the static measurement (lower plot).

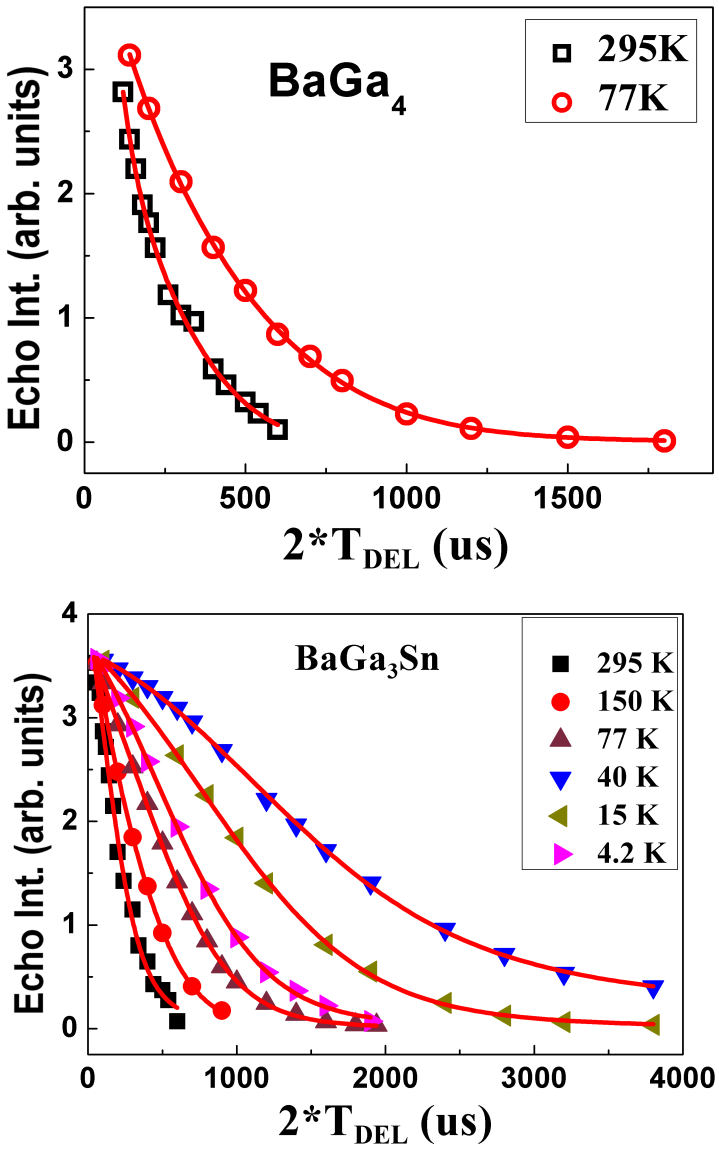

Fig. 51. Spin-spin relaxation measurements of layered $BaGa_4$ (upper plot) $BaGa_3Sn$ (lower plot) along temperature at peak-II with standard T_2 fits (solid curves).

Table IV. Fitted T_2 and parameters from equation (3.20) for peak-II of $BaGa_4$.

Temperature (K)	α	$T_{2e}(\mu s)$	$T_{2g}(\mu s)$
295	3.90	64.8	373.2
77	4.8	320.2	659.1

tures, which explains the temperature-dependent peak amplitude. After adjusting for the measured T_2 and extrapolating to $T_{DEL} = 0$, the lineshapes follow the temperature ratio as expected, so that the amplitude of peak-II corresponds to a T-dependent spin sensity. The extrapolated areas for peak-I and II are roughly equal.

Recalling the slow motion discussion in the $Ba_8In_{16}Ge_{30}$ section and also the previous $Sr_8Ga_{16}Ge_{30}$ studies [52], it appears that a similar type of low frequency atomic motion may be the reason for the small T_2 value and its decrease as the temperature rises. Generally, an exponential decay is observed where motion is important, whereas a Gaussian decay is characteristic of the static NMR line, dominated by the nuclear dipole-dipole couplings [52, 57]. Thus the ratio α is a measure of the relative importance of motion. For $BaGa_3Sn$, α is large at high temperatures, and the decay curve is exponential, which indicates that the echo decay is dominated by motion. However at low temperatures, α is smaller, indicating that the motional contribution partially dies out. For $BaGa_4$, the α values are big at both 295 K and 77 K, indicating that the motion contribution dominates. Also, notice that the exponential relaxation times (T_{2e}) for $BaGa_4$ are much smaller than those of $BaGa_3Sn$, whereas the Gaussian relaxation times (T_{2g}) are comparable, which indicates that the motional effect is stronger in the $BaGa_4$ structure.

For a better understanding of the atomic motion in $BaGa_3Sn$, we can further

Table V. Fitted T_2 and parameters from equation (3.20) for peak-II of $BaGa_3Sn$.

Temperature (K)	α	$T_{2e}(\mu s)$	$T_{2g}(\mu s)$
295	2.01	229.1	247.6
150	2.08	280.2	502.2
77	0.96	460.1	701.7
40	0.74	675.0	844.5
15	0.65	1072.1	1312.0
4.2	0.81	2700.4	1700.1

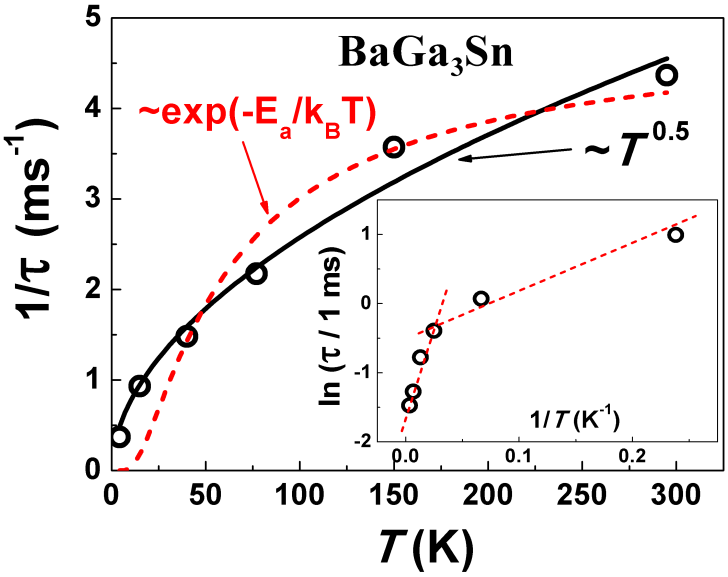

Fig. 52. $1/\tau$ vs. T for $BaGa_3Sn$ with a $T^{0.5}$ fit (solid curve) and an thermal activated fit (dashed curve). Inset: $\ln(\tau/1\text{ms})$ vs. $1/T$ plot. The two dashed lines represent two possible activation behavior in two different temperature regions.

explore the relationship between the motion frequency ($1/\tau$) and temperature. As discussed previously, the atomic motion only shows a significant influence on the relaxation process when its correlation time, τ, is comparable to T_2. As only the exponential contribution is related to the atomic motion, we assume $\tau \cong T_{2e}$ and plot $1/\tau$ vs. T in Fig. 52. For standard thermal activated motions, the motion correlation time (τ) is expected to follow $\tau = \tau_0 \exp(E_a/k_B T)$, where E_a is the activation energy. It is clear from the dashed curve in the figure that the data cannot be fitted by this simple formula very well for the entire temperature range. Instead, a $T^{0.5}$ behavior offers a better fit. This indicates a more complicated motion behavior than a simple temperature activation model. Furthermore, we can plot $\ln(\tau/1\text{ ms})$ vs. $1/T$ to get a closer look at its controlling exponent, as shown in the inset of Fig. 52. It appears that two different exponential relations are followed in different temperature regions, which may indicate a change of activation energy (E_a) vs. temperature.

Currently we do not know the physical mechanism behind the fast T_2 in these materials. However, because they are close to being Zintl phases, it may be that spontaneous vacancies are induced, as also seen in the Ge-based clathrates. Vacancy centers could allow the freedom for atomic motion implied by the NMR results.

The $K^2 T_1 T$ values were calculated for both of the peaks in $BaGa_3Sn$. Here we used the frequency shifts of the mass center as the Knight shift for peak-I. Peak-II is more complicated, and it is similar to the broadened two-peak lineshape caused by an axial second order quadrupole effect [59]. Note that axial symmetry is exact for $BaGa_4$, while no significant symmetry change apparently occurs for $BaGa_3Sn$. In this case, the positions of the two edge singularities (ν_I, ν_{II}) and the center frequency (ν_0) used for Knight shift calculation, have the following relationship [59]:

$$\nu_{\mathrm{I}} = \nu_0 + \frac{\nu_Q^2}{16\nu_0}\left[I\left(I+1\right) - 3/4\right] = \nu_0 + b/\nu_0, \tag{5.20}$$

$$\nu_{\mathrm{II}} = \nu_0 - \frac{\nu_Q^2}{9\nu_0}\left[I\left(I+1\right) - 3/4\right] = \nu_0 - \frac{16b}{9\nu_0}, \tag{5.21}$$

where $b = \frac{\nu_Q^2}{16}\left[I\left(I+1\right) - 3/4\right]$, and $I = 3/2$ for the present case. Taking the $BaGa_3Sn$ lineshape data at 4.2 K for example, $\nu_{\mathrm{I}} \cong 116.840$ MHz, $\nu_{\mathrm{II}} \cong 116.720$ MHz and the reference frequency is $\nu_{ref} = 116.4115$ MHz. So following the equations above, we obtain $\nu_0 = 116.7968$ MHz, $\nu_Q = 5.19$ MHz and $K = \left(\nu_0 - \nu_{ref}\right)/\nu_{ref} \cong 0.0033$. Considering that the T_1 value for peak-II at 4.2 K is 80 ms, we get $K^2T_1T \cong 3.7\times10^{-6}$ s·K.

Following the same procedure, K^2T_1T can be calculated for both peaks. The results for $BaGa_3Sn$ are plotted in Fig. 53 on a log scale. K^2T_1T varies around 2.5×10^{-6} s·K for peak-I, and around 3.5×10^{-6} s·K for peak-II. The same calculation was also performed on $BaGa_4$ using data for 77 K and 295 K, which gave $K^2T_1T \cong 2.0\times10^{-6}$ s·K for peak-I and 2.5×10^{-6} s·K for peak-II, similar to the $BaGa_3Sn$ results. From equation (3.8), the value of K^2T_1T for ^{71}Ga in a free-electron system is 2.73×10^{6} s·K. It is clear that K^2T_1T values for both peaks and both samples are nearly constant and close to the expected value. The result is consistent with metallic behavior. Note that it was reported that pseudogaps are expected in $BaGa_4$ and many $BaGa_4$ type materials from density of states calcuations [95]. However we do not have evidence to confirm this from our NMR results.

For $BaGa_4$, there is a clear shift and narrowing for the two NMR peaks as T increases. Taking peak-II for example, the ν_Q value for 77 K and 295 K can be calculated by equation (5.21) an (5.22), which gives $\nu_Q(77\mathrm{K}) = 8.85$ MHz, and $\nu_Q(295\mathrm{K}) = 7.77$ MHz. There is a 14% difference in ν_Q between the two temperatures. *Ab-initio* calculations are being performed by other members in our group, which have given good agreement with the NMR spectrum with a slightly smaller quadrupole shift. These configuration calculations are going to be continued for these samples,

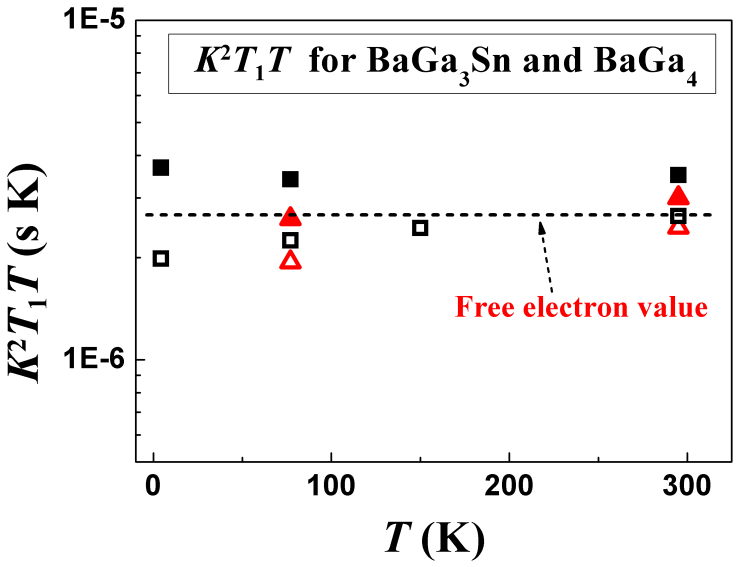

Fig. 53. The values of K^2T_1T of ^{71}Ga for $BaGa_3Sn$ peak-I (open squares) and peak-II (solid squares) are plotted in log scale. The value for $BaGa_4$ peak-I (open triangles) and peak-II (solid triangles) are also plotted. All of them are nearly constant and close to the free electron value of ^{71}Ga (dashed line).

which are expected to offer further understanding of these materials.

3. Summary

From the analysis above, it is clear that $BaGa_4$ and $BaGa_3Sn$ share the same structure and show similar NMR spectra. Also, their spin-spin relaxation behaviors are similar, showing fast dephasing at high temperatures. This can be explained by the influence of slow atomic motion. Also, the fitted spin-spin relaxation behavior for $BaGa_3Sn$ has also shown a change of atomic activation energy around 50 K, which could be due to a phase change or distortion.

CHAPTER VI

CONCLUSIONS

In summary, type-I $Ba_8Ga_{16}Sn_{30}$ NMR lineshapes and spin-lattice relaxation rates indicate the presence of a strong quadrupole relaxation mechanism. Analysis showed this behavior to be due to a strongly anharmonic rattler-type motion of the caged Ba(2) atoms. Fitting using a 1-D double well potential with strong anharmonicity showed good agreement with the experimental data, and offers a good explanation for the rattling behavior and the relaxation mechanism.

The anharmonic influence on the resistivity as well as the heat capacity were also demonstrated for this material. An x^4-type anharmonic potential provides good agreement for the NMR results, heat capacity, and transport measurements with the same set of parameters. The damping parameter is large, indicating that these vibrations interact strongly with vibrational or electronic excitations in the structure. However the success of the 1-D model in this case implies that the expected 2-D motion of these rattlers is not activated, perhaps through cage distortion. Also, the low temperature Einstein contribution and a variable Debye temperature indicate the existence of a broader energy distribution of the oscillators, which is similar to the assumption in the SPM model.

Although other clathrate samples in this work did not show strong anharmonic rattling behavior as observed in type-I $Ba_8Ga_{16}Sn_{30}$, they still exhibit interesting properties. Type-VIII $Ba_8Ga_{16}Sn_{30}$, $Ba_8Ga_{16}Ge_{30}$ and type-I $Ba_8In_{16}Ge_{30}$ have shown similar spin-lattice relaxation behavior vs. temperature, which can be fitted to a T^{α} behavior with $\alpha \cong 1.5$. This is similar to the situation for the amorphous materials, where the tunneling model could be a good explanation. A semiconducting model gives a more reasonable physical picture of the electron structure near the Fermi sur-

face for type-VIII $Ba_8Ga_{16}Sn_{30}$ and type-I $Ba_8In_{16}Ge_{30}$, which explains their metallic-like behaviors as indicated by the Korringa relation. Also, the existence of impurity bands in n-type $Ba_8Ga_{16}Ge_{30}$ was indicated by its unusual magnetic spin-lattice relaxation behavior.

The investigation of a series of $Ba_8Cu_xGe_{46-x}$ samples showed a clear relationship between the composition and the NMR results for both the spectrum and relaxation behaviors. Study of the Zintl composition, $x = 5.3$, showed an extremely long T_1 and non-metallic behavior. Also, *ab-initio* calculations combined with the NMR lineshapes offered useful information connecting the spectral broadening to the atomic distribution, similar to what was found for type-I $Ba_8Ga_{16}Sn_{30}$.

Spin-spin relaxation measurements for $Ba_8In_{16}Ge_{30}$ and the layered $BaGa_3Sn$ showed that the NMR lineshapes are affected by the atomic motion and the resulting dephasing process. Both of these materials exhibit NMR controlled by an exponential T_2 contribution at high temperatures which makes the dephasing much faster and reduces the NMR signal significantly. The T_2 values are bigger at lower temperatures, indicating slower motions. Thermal activated atomic motions play an important role in both materials.

Together with the T_1 measurements, a Korringa-like behavior can be observed for both sites of $BaGa_4$ and $BaGa_3Sn$, and the values are close to the theoretical prediction, confirming the metallic behavior for this material.

In conclusion, the NMR techniques used in this work are very powerful tools for material analysis for a broad range of different types of materials. With the addition of other measurements, including XRD, resistivity and heat capacity, it was possible to investigate structural configurations, relaxation mechanisms and atomic motions. The results include a variety of interesting properties. The anharmonicity of the guest atomic motion might be one of the most important. In this work I have

demonstrated its influence on several other properties, including thermal behavior and transport properties.

REFERENCES

[1] H. J. Goldsmid, *Thermoelectric Refrigeration*, Plenum Press, New York, 1964.

[2] D. M. Rowe, *CRC Handbook of Thermoelectrics*, CRC, Boca Raton, 1995.

[3] I. Terasaki, Y. Sasago, and K. Uchinokura, "Large thermoelectric power in $NaCo_2O_4$ single crystals," *Phys. Rev. B*, vol. 56, pp. R12685–R12687, Nov. 1997.

[4] R. Venkatasubramanian, E. Siivola, T. Colpitts, and B. O'Quinn, "Thin-film thermoelectric devices with high room-temperature figures of merit," *Nature*, vol. 413, pp. 597–602, Oct. 2001.

[5] D. G. Cahill, W. K. Ford, K. E. Goodson, G. D. Mahan, A. Majumdar, H. J. Maris, R. Merlin, and S. R. Phillpot, "Nanoscale thermal transport," *J. Appl. Phys.*, vol. 93, no. 2, pp. 793–818, 2003.

[6] S. D. Obertelli, J. R. Cooper, and J. L. Tallon, "Systematics in the thermoelectric power of high-T_C oxides," *Phys. Rev. B*, vol. 46, pp. 14928–14931, Dec. 1992.

[7] A. I. Hochbaum, R. Chen, R. D. Delgado, W. Liang, E. C. Garnett, M. Najarian, A. Majumdar, and P. Yang, " Enhanced thermoelectric performance of rough silicon nanowires," *Nature*, vol. 451, pp. 163–167, Jan. 2008.

[8] K. F. Hsu, S. Loo, F. Guo, W. Chen, J. S. Dyck, C. Uher, T. Hogan, E. K. Polychroniadis, and M. G. Kanatzidis, "Cubic $AgPb_mSbTe_{2+m}$: Bulk thermoelectric materials with high figure of merit," *Science*, vol. 303, no. 5659, pp. 818–821, Feb. 2004.

[9] T. C. Harman, P. J. Taylor, M. P. Walsh, and B. E. LaForge, "Quantum dot superlattice thermoelectric materials and devices," *Science*, vol. 297, no. 5590, pp. 2229–2232, 2002.

[10] G. J. Snyder and E. S. Toberer, "Complex thermoelectric materials," *Nat. Mater.*, vol. 7, no. 2, pp. 105–114, 2008.

[11] G. S. Nolas, J. L. Cohn, G. A. Slack, and S. B. Schujman, "Semiconducting Ge clathrates: Promising candidates for thermoelectric applications," *Appl. Phys. Lett.*, vol. 73, no. 2, pp. 178–180, 1998.

[12] T. N. Narasimhan, "Thermal conductivity through the 19th century," *Physics Today*, vol. 63, no. 8, pp. 36–41, Aug. 2010.

[13] C. Kittel, *Introduction to Solid State Physics, 6th Ed.*, John Wiley & Sons, Inc., New York, 1986.

[14] J. S. Kasper, P. Hagenmuller, M. Pouchard, and C. Cros, "Clathrate structure of silicon Na_8Si_{46} and Na_xSi_{136} ($x < 11$)," *Science*, vol. 150, no. 3704, pp. 1713–1714, 1965.

[15] C. Cros, M. Pouchard, and P. Hagenmuller, "Sur une nouvelle famille de clathrates minèraux isotypes des hydrates de gaz et de liquides. Interprètation des rèsultats obtenus," *J. Solid State Chem.*, vol. 2, no. 4, pp. 570 – 581, 1970.

[16] R. Alben, D. Weaire, J. E. Smith, and M. H. Brodsky, "Vibrational properties of amorphous Si and Ge," *Phys. Rev. B*, vol. 11, pp. 2271–2296, Mar. 1975.

[17] J. H. Ross, Jr. and Y. Li, "Superconductivity and magnetism in silicon and germanium clathrates," in *Nanoscale Magnetic Materials and Applications*, J. P.

Liu, E. Fullerton, O. Gutfleisch, and D.J. Sellmyer, Eds., chapter 4. Springer, New York, 2009.

[18] G. S. Nolas, T. J. R. Weakley, J. L. Cohn, and R. Sharma, "Structural properties and thermal conductivity of crystalline Ge clathrates," *Phys. Rev. B*, vol. 61, pp. 3845–3850, Feb. 2000.

[19] S. Paschen, W. Carrillo-Cabrera, A. Bentien, V. H. Tran, M. Baenitz, Yu. Grin, and F. Steglich, "Structural, transport, magnetic, and thermal properties of $Eu_8Ga_{16}Ge_{30}$," *Phys. Rev. B*, vol. 64, pp. 214404, Nov. 2001.

[20] B. C. Sales, B. C. Chakoumakos, R. Jin, J. R. Thompson, and D. Mandrus, "Structural, magnetic, thermal, and transport properties of $X_8Ga_{16}Ge_{30}$ (X=Eu, Sr, Ba) single crystals," *Phys. Rev. B*, vol. 63, no. 24, pp. 245113, Jun. 2001.

[21] A. Bentien, M. Christensen, J. D. Bryan, A. Sanchez, S. Paschen, F. Steglich, G. D. Stucky, and B. B. Iversen, "Thermal conductivity of thermoelectric clathrates," *Phys. Rev. B*, vol. 69, pp. 045107, Jan. 2004.

[22] M. A. Avila, K. Suekuni, K. Umeo, H. Fukuoka, S. Yamanaka, and T. Takabatake, "Glasslike versus crystalline thermal conductivity in carrier-tuned $Ba_8Ga_{16}X_{30}$ clathrate (X=Ge, Sn)," *Phys. Rev. B*, vol. 74, no. 12, pp. 125109, Sep. 2006.

[23] M. A. Avila, K. Suekuni, K. Umeo, H. Fukuoka, S. Yamanaka, and T. Takabatake, "$Ba_8Ga_{16}Sn_{30}$ with type-I clathrate structure: Drastic suppression of heat conduction," *Appl. Phys. Lett.*, vol. 92, no. 4, pp. 041901, 2008.

[24] I. Fujita, K. Kishimoto, M. Sato, H.i Anno, and T. Koyanagi, "Thermoelectric properties of sintered clathrate compounds $Sr_8Ga_xGe_{46-x}$ with various carrier

concentrations," *J. Appl. Phys.*, vol. 99, no. 9, pp. 093707, 2006.

[25] N. L. Okamoto, K. Kishida, K. Tanaka, and H. Inui, "Effect of In additions on the thermoelectric properties of the type-I clathrate compound $Ba_8Ga_{16}Ge_{30}$," *J. Appl. Phys.*, vol. 101, no. 11, pp. 113525, 2007.

[26] K. Suekuni, S. Yamamoto, M. A. Avila, and T. Takabatake, "Universal relation between guest free space and lattice thermal conductivity reduction by anharmonic rattling in type-I clathrates," *J. Phys. Soc. Jpn.*, vol. 77SA, no. Supplement A, pp. 61–66, 2008.

[27] S. Johnsen, A. Bentien, G. K. H. Madsen, B. B. Iversen, and M. Nygren, "Crystal structure, band structure, and physical properties of $Ba_8Cu_{6-x}Ge_{40+x}$ ($0 \leq x \leq 0.7$)," *Chem. Mater.*, vol. 18, no. 19, pp. 4633–4642, 2006.

[28] S. Deng, Y. Saiga, K. Suekuni, and T. Takabatake, "Enhancement of thermoelectric efficiency in type-VIII clathrate $Ba_8Ga_{16}Sn_{30}$ by Al substitution for Ga," *J. Appl. Phys.*, vol. 108, no. 7, pp. 073705, 2010.

[29] B. C. Chakoumakos, B. C. Sales, D. G. Mandrus, and G. S. Nolas, "Structural disorder and thermal conductivity of the semiconducting clathrate $Sr_8Ga_{16}Ge_{30}$," *J. Alloys Compd.*, vol. 296, no. 12, pp. 80 – 86, 2000.

[30] R. P. Hermann, V. Keppens, P. Bonville, G. S. Nolas, F. Grandjean, G. J. Long, H. M. Christen, B. C. Chakoumakos, B. C. Sales, and D. Mandrus, "Direct experimental evidence for atomic tunneling of europium in crystalline $Eu_8Ga_{16}Ge_{30}$," *Phys. Rev. Lett.*, vol. 97, pp. 017401, Jul. 2006.

[31] Y. Takasu, T. Hasegawa, N. Ogita, M. Udagawa, M. A. Avila, K. Suekuni, and T. Takabatake, "Off-center rattling and cage vibration of the carrier-tuned type-

I clathrate $Ba_8Ga_{16}Ge_{30}$ studied by Raman scattering," *Phys. Rev. B*, vol. 82, pp. 134302, Oct. 2010.

[32] K. Suekuni, M. A. Avila, K. Umeo, and T. Takabatake, "Cage-size control of guest vibration and thermal conductivity in $Sr_8Ga_{16}Si_{30-x}Ge_x$," *Phys. Rev. B*, vol. 75, pp. 195210, May 2007.

[33] T. Dahm and K. Ueda, "NMR relaxation and resistivity from rattling phonons in pyrochlore superconductors," *Phys. Rev. Lett.*, vol. 99, no. 18, pp. 187003, Oct. 2007.

[34] K. Umeo, M. A. Avila, T. Sakata, K. Suekuni, and T. Takabatake, "Probing glasslike excitations in single-crystalline $Sr_8Ga_{16}Ge_{30}$ by specific heat and thermal conductivity," *J. Phys. Soc. Jpn.*, vol. 74, no. 8, pp. 2145–2148, 2005.

[35] K. Suekuni, M. A. Avila, K. Umeo, H. Fukuoka, S. Yamanaka, T. Nakagawa, and T. Takabatake, "Simultaneous structure and carrier tuning of dimorphic clathrate $Ba_8Ga_{16}Sn_{30}$," *Phys. Rev. B*, vol. 77, no. 23, pp. 235119, Jun. 2008.

[36] M. Yoshida, K. Arai, R. Kaido, M. Takigawa, S. Yonezawa, Y. Muraoka, and Z. Hiroi, "NMR observation of rattling phonons in the pyrochlore superconductor KOs_2O_6," *Phys. Rev. Lett.*, vol. 98, no. 19, pp. 197002, May 2007.

[37] J. Dong, O. F. Sankey, G. K. Ramachandran, and P. F. McMillan, "Chemical trends of the rattling phonon modes in alloyed germanium clathrates," *J. Appl. Phys.*, vol. 87, no. 11, pp. 7726–7734, 2000.

[38] T. Mori, K. Iwamoto, S. Kushibiki, H. Honda, H. Matsumoto, N. Toyota, M. A. Avila, K. Suekuni, and T. Takabatake, "Optical conductivity spectral anomalies

in the off-center rattling system β-$Ba_8Ga_{16}Sn_{30}$," *Phys. Rev. Lett.*, vol. 106, no. 1, pp. 015501, Jan. 2011.

[39] G. D. Mahan and J. O. Sofo, "Resistivity and superconductivity from anharmonic phonons," *Phys. Rev. B*, vol. 47, no. 13, pp. 8050–8055, Apr. 1993.

[40] X. Zheng, S. Y. Rodriguez, and J. H. Ross, Jr., "NMR relaxation and rattling phonons in the type-I $Ba_8Ga_{16}Sn_{30}$ clathrate," *Phys. Rev. B*, vol. 84, no. 2, pp. 024303, Jul. 2011.

[41] I. Zerec, V. Keppens, M. A. McGuire, D. Mandrus, B. C. Sales, and P. Thalmeier, "Four-well tunneling states and elastic response of clathrates," *Phys. Rev. Lett.*, vol. 92, no. 18, pp. 185502, May 2004.

[42] M. Christensen, S. Johnsen, and B. B. Iversen, "Thermoelectric clathrates of type I," *Dalton Trans.*, vol. 39, pp. 978–992, 2010.

[43] M. Christensen, A. B. Abrahamsen, N. B. Christensen, F. Juranyi, N. H. Andersen, K. Lefmann, J. Andreasson, C. R. H. Bahl, and B. B. Iversen, "Avoided crossing of rattler modes in thermoelectric materials," *Nat. Mater.*, vol. 7, no. 10, pp. 811–815, 2008.

[44] S. M. Kauzlarich, S. R. Brown, and G. Jeffrey Snyder, "Zintl phases for thermoelectric devices," *Dalton Trans.*, pp. 2099–2107, 2007.

[45] R. Nesper, "Structure and chemical bonding in zintl-phases containing lithium," *Prog. Solid St. Chem.*, vol. 20, pp. 1–45, 1990.

[46] S. Y. Rodriguez, L. Saribaev, and J. H. Ross, Jr., "Zintl behavior and vacancy formation in type-I Ba-Al-Ge clathrates," *Phys. Rev. B*, vol. 82, pp. 064111, Aug. 2010.

[47] A. Laaksonen and P. Stilbs, "Molecular dynamics and NMR study of methane-water systems," *Mol. Phys.*, vol. 74, no. 4, pp. 747–764, 1991.

[48] G. K. Ramachandran, P. F. McMillan, J. Diefenbacher, J. Gryko, J. Dong, and O. F. Sankey, "^{29}Si NMR study on the stoichiometry of the silicon clathrate Na_8Si_{46}," *Phys. Rev. B*, vol. 60, pp. 12294–12298, Nov. 1999.

[49] J. Gryko, P. F. McMillan, R. F. Marzke, A. P. Dodokin, A. A. Demkov, and O. F. Sankey, "Temperature-dependent ^{23}Na Knight shifts and sharply peaked structure in the electronic densities of states of Na-Si clathrates," *Phys. Rev. B*, vol. 57, no. 7, pp. 4172–4179, Feb. 1998.

[50] J. Gryko, P. F. McMillan, and O. F. Sankey, "NMR studies of Na atoms in silicon clathrate compounds," *Phys. Rev. B*, vol. 54, pp. 3037–3039, Aug. 1996.

[51] W. Gou, Y. Li, J. Chi, J. H. Ross, Jr., M. Beekman, and G. S. Nolas, "NMR study of slow atomic motion in $Sr_8Ga_{16}Ge_{30}$ clathrate," *Phys. Rev. B*, vol. 71, no. 17, pp. 174307, May 2005.

[52] W. Gou, *A Nuclear Magnetic Resonance Probe of Group IV Clathrates*, PhD Thesis, Texas A&M University, 2008.

[53] W. Gou, S. Y. Rodriguez, Y. Li, and J. H. Ross, Jr., "NMR experiments and electronic structure calculations in type-I BaAlGe clathrates," *Phys. Rev. B*, vol. 80, pp. 144108, Oct. 2009.

[54] S. Y. Rodriguez, X. Zheng, L. Saribaev, and J. H. Ross, Jr., "NMR and computational studies of $Ba_8Ga_{16}Sn_{30}$ clathrates," *Proc. Mater. Res. Soc.*, vol. 1267, pp. DD04–07, 2010.

[55] S. Y. Rodriguez, *Magnetic and Electronic Properties in Rattling Systems, an Experimental and Theoretical Study*, PhD Thesis, Texas A&M University, 2011.

[56] C. P. Slichter, *Principles of Magnetic Resonance*, Springer-Verlag, New York, 1990.

[57] A. Abragam, *Principles of Nuclear Magnetism*, Oxford University Press, London, 1982.

[58] W. D. Knight, "Nuclear magnetic resonance shift in metals," *Phys. Rev.*, vol. 76, pp. 1259–1260, Oct. 1949.

[59] G. C. Carter, L. H. Bennett, and D. J. Kahan, *Metallic Shifts in NMR*, Pergamon, New York, 1977.

[60] Paul T. Callaghan, *Principles of Nuclear Magnetic Resonance Microscopy*, Clarendon Press, Oxford, 1993.

[61] E. R. Andrew, A. Bradbury, and R. G. Eades, "Nuclear magnetic resonance spectra from a crystal rotated at high speed," *Nature*, vol. 182, pp. 1659, Dec. 1958.

[62] X. Zheng, S. Y. Rodriguez, L. Saribaev, and J. H. Ross, Jr., "Transport and thermodynamic properties under anharmonic motion in type-I $Ba_8Ga_{16}Sn_{30}$ clathrate," *Phys. Rev. B*, vol. 85, pp. 214304, Jun. 2012.

[63] B. H. Toby, "EXPGUI, a graphical user interface for GSAS," *J. Appl. Cryst.*, vol. 34, pp. 201, 2001.

[64] R. K. Harris and E. D. Becker, "NMR nomenclature: Nuclear spin properties and conventions for chemical shifts-IUPAC recommendations," *J. Magn. Reson.*, vol. 156, pp. 323, 2002.

[65] B. S. Shastry and E. Abrahams, "What does the Korringa ratio measure," *Phys. Rev. Lett.*, vol. 72, no. 12, pp. 1933–1936, Mar. 1994.

[66] J. M. Ziman, *Principles of the Theory of Solids*, Cambridge University Press, Cambridge, 1972.

[67] J. R. Cooper, "Electrical resistivity of an Einstein solid," *Phys. Rev. B*, vol. 9, no. 6, pp. 2778–2780, Mar. 1974.

[68] A. Bulusu and D.G. Walker, "Review of electronic transport models for thermoelectric materials," *Superlattices Microstruct.*, vol. 44, no. 1, pp. 1 – 36, 2008.

[69] K. Biswas and C. W. Myles, "Electronic and vibrational properties of framework substituted type II silicon clathrate," *Phys. Rev. B*, vol. 75, no. 24, pp. 245205, Jun. 2007.

[70] E. Reny, A. San-Miguel, Y. Guyot, B. Masenelli, P. Mélinon, L. Saviot, S. Yamanaka, B. Champagnon, C. Cros, M. Pouchard, M. Borowski, and A. J. Dianoux, "Vibrational modes in silicon clathrate compounds: A key to understanding superconductivity," *Phys. Rev. B*, vol. 66, pp. 014532, Jul. 2002.

[71] R. P. Hermann, W. Schweika, O. Leupold, R. Rüffer, G. S. Nolas, F. Grandjean, and G. J. Long, "Neutron and nuclear inelastic scattering study of the Einstein oscillators in Ba-, Sr-, and Eu- filled germanium clathrates," *Phys. Rev. B*, vol. 72, pp. 174301, Nov. 2005.

[72] S. Johnsen, M. Christensen, B. Thomsen, G. K. H. Madsen, and B. B. Iversen, "Barium dynamics in noble-metal clathrates," *Phys. Rev. B*, vol. 82, pp. 184303, Nov. 2010.

[73] M. Christensen, N. Lock, J. Overgaard, and B. B. Iversen, "Crystal structures of thermoelectric n- and p-type $Ba_8Ga_{16}Ge_{30}$ studied by single crystal, multi-temperature, neutron diffraction, conventional X-ray diffraction and resonant synchrotron X-ray diffraction," *J. Am. Chem. Soc.*, vol. 128, no. 49, pp. 15657–15665, 2006.

[74] M. Christensen, S. Johnsen, F. Juranyi, and B. B. Iversen, "Clathrate guest atoms under pressure," *J. Appl. Phys.*, vol. 105, no. 7, pp. 073508, 2009.

[75] J. H. Roudebush, C. de la Cruz, B. C. Chakoumakos, and S. M. Kauzlarich, "Neutron diffraction study of the type I clathrate $Ba_8Al_xSi_{46-x}$: Site occupancies, cage volumes, and the interaction between the guest and the host framework," *Inorg. Chem.*, vol. 51, no. 3, pp. 1805–1812, 2012.

[76] C. L. Condron, J. Martin, G. S. Nolas, P. M. B. Piccoli, A. J. Schultz, and S. M. Kauzlarich, "Structure and Thermoelectric Characterization of $Ba_8Al_{14}Si_{31}$," *Inorg.Chem.*, vol. 45, no. 23, pp. 9381–9386, 2006.

[77] C. Lee, H. Yoshizawa, M. A. Avila, I. Hase, K. Kihou, and T. Takabatake, "Phonon dynamics of type-I clathrate $Sr_8Ga_{16}Ge_{30}$ studied by inelastic neutron scattering," *J. Phys. Soc. Jpn.*, vol. 77SA, no. Suppl. A, pp. 260–262, 2008.

[78] M. A. Ramos and U. Buchenau, *Tunneling systems in amorphous and crystalline solids*, Springer, Berlin, 1998.

[79] A. Lindqvist, O. Yamamuro, I. Tsukushi, and T. Matsuo, "Excess heat capacities due to the low-energy excitations of molecular glasses: An approach using the soft potential model," *J.Chem. Phys.*, vol. 107, no. 13, pp. 5103–5107, 1997.

[80] T. L. Reinecke and K. L. Ngai, "Low-temperature nuclear-spin-lattice relaxation in glasses," *Phys. Rev. B*, vol. 12, pp. 3476–3478, Oct. 1975.

[81] G. E. Jellison, Gary L. Petersen, and P. C. Taylor, "Tunneling modes and local structural order in amorphous arsenic," *Phys. Rev. Lett.*, vol. 42, pp. 1413–1416, May 1979.

[82] J. Szeftel and H. Alloul, "Nuclear spin-lattice relaxation associated with low-energy excitations in glasses," *Phys. Rev. Lett.*, vol. 34, pp. 657–660, Mar. 1975.

[83] P. W. Anderson, B. I. Halperin, and C. M. Varma, "Anomalous low-temperature thermal properties of glasses and spin glasses," *Philos. Mag.*, vol. 25, no. 1, pp. 1–9, 1972.

[84] P. W. Anderson, "Model for the electronic structure of amorphous semiconductors," *Phys. Rev. Lett.*, vol. 34, pp. 953–955, Apr. 1975.

[85] M. Rubinstein and P. C. Taylor, "Nuclear quadrupole resonance in amorphous and crystalline As_2S_3," *Phys. Rev. B*, vol. 9, pp. 4258–4276, May 1974.

[86] C. S. Lue, S. Y. Wang, and C. P. Fang, "NMR probe of pseudogap characteristics in $CaAl_{2-x}Si_{2+x}$," *Phys. Rev. B*, vol. 75, pp. 235111, Jun. 2007.

[87] N. Bloembergen, "Nuclear magnetic relaxation in semiconductors," *Physica*, vol. 20, no. 712, pp. 1130 – 1133, 1954.

[88] R. A. Ribeiro, T. Ekino, M. A. Avila, and T. Takabatake, "Tunneling spectroscopy of single-crystal clathrate $Ba_8Ga_{16}Sn_{30}$," *Physica B*, vol. 383, no. 1, pp. 126 – 127, 2006.

[89] Y. Li, J. Chi, W. Gou, S. Khandekar, and J. H. Ross, Jr., "Structure and stability of BaCuGe type-I clathrates," *J. Phys.: Condens. Matter*, vol. 15, no. 32, pp. 5535, 2003.

[90] D. P. Tunstall and V. G. I. Deshmukh, "Conduction electrons in an impurity band: NMR in Ge:As," *J. Phys. C: Solid State Physics*, vol. 12, no. 12, pp. 2295, Jun. 1979.

[91] E. M. Meintjes, J. Danielson, and W. W. Warren, "Temperature-dependent NMR study of the impurity state in heavily doped Si:P," *Phys. Rev. B*, vol. 71, pp. 035114, Jan. 2005.

[92] J. H. Ross, Jr., "Calculations on $Ba_8Ga_{16}Ge_{30}$ clathrate," Private communication, 2012.

[93] R. L. Mieher, "Quadrupolar nuclear relaxation in the III-V compounds," *Phys. Rev.*, vol. 125, pp. 1537–1551, Mar. 1962.

[94] J. Chen, "*Ab-initio* calculations on $Ba_8In_{16}Ge_{30}$ clathrate," Private communication, 2012.

[95] U. Häussermann, S. Amerioun, L. Eriksson, C.-S. Lee, and G. J. Miller, "The s-p bonded representatives of the prominent $BaAl_4$ structure type: A case study on structural stability of polar intermetallic network structures," *J. Am. Chem. Soc.*, vol. 124, no. 16, pp. 4371–4383, 2002.

[96] F. Haarmann, K. Koch, P. Jeglič, O. Pecher, H. Rosner, and Y. Grin, "NMR spectroscopy of intermetallic compounds: An experimental and theoretical approach to local atomic arrangements in binary gallides," *Chem. Eur. J.*, vol. 17, pp. 7560–7568, Jun. 2011.

[97] P. H. Tobash, Y. Yamasaki, and S. Bobev, "Gallium-tin mixing in $BaGa_{4-x}Sn_x$ [$x = 0.89(2)$] with the $BaAl_4$ structure type," *Acta Cryst. E*, vol. 63, pp. i35–i37, Jan. 2007.

VITA

Xiang Zheng was born in Hefei, Anhui, China in 1985. He received his B.S. degree in physics from University of Science and Technology of China in 2007. His work was focused on the structure and magnetic properties of epitaxial thin films. He obtained his M.S. degree in physics at Texas A&M University, in 2009. The field of specialization was on solid state NMR experiments. He received his Ph.D. degree in materials science and engineering from Texas A&M University in 2012, with emphasis on theoretical and experimental studies of thermoelectric clathrate materials. His email address is zheng_095@hotmail.com.

Contact information: c/o Dr. Joseph H. Ross, Jr., Department of Physics and Astronomy, Texas A&M University, College Station, TX 77843-4242, USA.

The typist for this thesis was Xiang Zheng.